Università Ca'Foscari Venezia

Master's Degree on Chemistry and Sustainable Technologies

Synthesis and characterization of novel materials for aqueous zinc-ion batteries

Student	Sara Sfiligoi
Matriculation number	854417
Academic Year	2020/2021
Appraisers	Prof. Salvatore Daniele
	Prof. Fabio La Mantia

Contents

1. INTRODUCTION

The industrial revolutions in the past centuries have led to extraordinary changes in social life, transportation, and production activities, with energy utilization reflecting the progress of industrial technology and human civilization. The primary energy sources that have been used to power all tech-dependent human activities were the fossil fuels, such as crude oils and natural gas, with no little consequences. In fact, pollution arising from fossil fuel combustion has had a devastating impact on the natural environment and on the human health[1]. In addition, the natural reserves of fossil fuels are limited[2]. Therefore, these energy sources are not sustainable by multiple points of view. Hence, the focus of the research has shifted to environmentally benign sustainable energy.

The development of renewable energies and the need for means of transport with reduced CO_2 emissions have generated new interest in storage, which has become a key component of sustainable development. Energy storage is a dominant factor in renewable energy plants. It can mitigate power variations, enhances the system flexibility and enables the storage and dispatching of the electricity generated by variable renewable energy sources such as wind and solar. The storage technologies used in electric power systems can be chemical or electrochemical, mechanical, electromagnetic or thermal storage[3]. As for electrochemical storage systems, there are many different types of batteries and most of them are subject to further research and development. Recently, several battery technologies, such as redox flow, sodium sulfur, lead carbon, or lithium ion, have been proposed as possible systems for large-scale stationary energy storage. However, they suffer from low charging rates, high operating temperatures and the use of hazardous materials in their components and/or high costs[4]. These drawbacks limit their integration into the electrical power grid[5]. Metal-ion aqueous rechargeable batteries have become a low-cost, safe, and environmentally friendly alternative to traditional technologies. Several cells based on lithium intercalation electrodes have been developed in recent years. However, the lower energy density and low availability

of lithium have led to the need for energy storage systems based on alternative elements[6].

1.1. History of the battery

A battery is a source of electric power consisting of one or more electrochemical cells.[7] An electrochemical cell is a device that can generate electrical energy. When the electric current is generated from a spontaneous chemical reaction, the electrochemical cell is called *Galvanic* or *Voltaic cell*, named after Luigi Galvani and Alessandro Volta, respectively. Conversely, when the device uses electrical energy to cause a chemical reaction, the cell is called *electrolytic cell*. The Galvanic (or Voltaic) cells can be categorized in *primary* and *secondary*. In the primary cells, the electric current in generated from a not reversible chemical reaction, rendering these devices not-rechargeable. Due to their high pollutant content compared to their small energy content, the primary battery is considered a wasteful and environmentally unfriendly technology. In secondary cells the chemical reaction can be reversed using an external current supplier, regenerating the chemical reactants. The first electrochemical battery was described and built by Alessandro Volta in 1799.[8] This system consisted of a stack of copper and zinc plates separated by brine-soaked paper disks, capable of producing a steady current (Figure 1.1).

Figure 1.1: Volta's electrochemical cell

In 1936, the so-called *Daniell Cell* was invented by the British chemist John Daniell. This cell consisted of a copper pot filled with a copper sulfate solution, in which it was immersed an unglazed earthenware container filled with sulfuric acid and a zinc electrode (Figure 1.2).

Figure 1.2: Daniell's cells, 1936

The main problem of the cells mentioned above was the use of a liquid electrolyte, which could leak if not handled correctly. To prevent the leakage, glass containers where used, making them fragile and potentially dangerous. For these reasons, wet cells were unsuitable for portable applications. In 1886, a new type of battery, called dry cell, was developed by Carl Gassner.[9] A dry cell uses a paste, having enough moisture to allow the current to flow, instead of a liquid electrolyte. For this reason,

unlike wet cells, dry cells are suitable for portable usage and this enabled the progress of technology, which led to the development of portable devices. [9] Among others, most used are Nickel-cadmium and lithium-ion cells. Lead–acid batteries did not achieve the safety and portability of the dry cell until the development of the gel battery.[10]

1.2. Lithium-ion Batteries

As the use of fossil fuels continues to rise, an increase in the concentration of toxic gases like NOx and SOx in the atmosphere can be seen.[11] Such gases, alongside with carbon dioxide, are the so-called greenhouse gases (GHG) and are responsible for the global warming.[12] Renewable energy sources such as wind and solar power are the most promising candidates for reducing the consumption of fossil fuels with the advantages of being free and unlimited. However, these resources are not always available. Therefore, to be able to use efficiently these sources, the energy needs to be storage. Hence the importance of battery systems.

1.3. Intercalation Li-ion batteries

Among the storage systems, lithium-ion batteries are by far the most revolutionary devices that have led to the technological progress we are experiencing nowadays, allowing the development of portable electronic products. The use of LiCoO2 as a positive-electrode material was first reported by Goodenough and co-workers in 1979.[13,14] In 1982, Yazami and Touzain reported the world's first successful experiment demonstrating the electrochemical intercalation and release of lithium in graphite.[15,16] Although the Li-ion batteries have set the starting point for the development of portable electronic systems, the toxicity and harmful of the compounds that make up the battery have become important issues.[17] These problems were overcome in 1994 by Dahn et al.[18] who introduced rechargeable aqueous Li-ion batteries (RALBs), in which flammable organic electrolytes were replaced with water-based electrolytes.[18] However, due to recent increase in the

price of lithium and its limited resources, large-scale applications have not yet been realized.[19] In the RALB, the operating mechanism involved Li ions intercalation/deintercalation mechanism[20] and based on this process a variety of other batteries have been developed, as is illustrated in the next sections.

In chemistry, intercalation is the reversible insertion of ions into layered materials with layered structure.[21] In these batteries, lithium ions move from the negative electrode to the positive electrode through the electrolyte solution during discharge (fFigure 1.3 b). During charging, the opposite process occurs (Figure 1.3 a), making the process *reversible*.

Li-ion batteries have a high energy density and low self-discharge. However, they can be a safety hazard since they contain flammable electrolytes. Even worse, if damaged or incorrectly charged they can lead to explosions.[22]

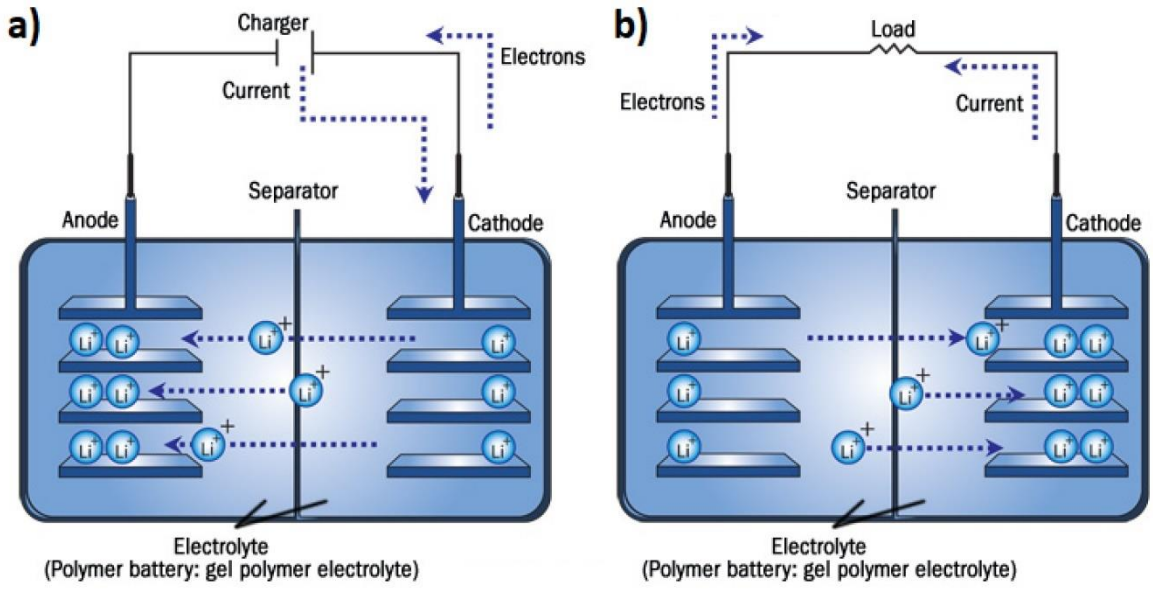

Figure 1.3: mechanism of charge (a) and discharge (b) of a Li-ion battery[23]

Compared to other rechargeable batteries, Li-ion batteries (LIBs) have become the leading energy storage systems since the introduction in 1991 by Sony.[24] However, when it comes to large scale applications such as in stationary grid energy storage or electric vehicles, the high cost and safety concerns related to LIBs become very

important issues.[17] For largescale applications, lead-acid batteries are still dominant due to their low cost and durability, even though lead compounds are of concern for the environment and harmful to human health, even at low concentrations.[25]

1.4. Aqueous Zinc-ion Batteries

For the reasons mentioned in the previous section, rechargeable zinc-ion batteries have been developed. This new type of battery is considered a promising candidate for grid energy storage thanks to the low price, nontoxicity and abundance of zinc. Furthermore, zinc metal has a high theoretical gravimetric and volumetric capacity of 820 mAh/g and 5854 mAh/cm^3, respectively.[11]

The zinc aqueous battery system was introduced for the first time in 1986 by Yamamoto et al., replacing the alkaline electrolyte with zinc sulfate electrolyte.[26]

The ZIBs, as Li-ion batteries, are intercalation batteries. They are based on a negative zinc electrode, whereas the active material on the positive electrode is able to accommodate Zn^{2+} in its crystalline structure during the discharge (Figure 1.4).

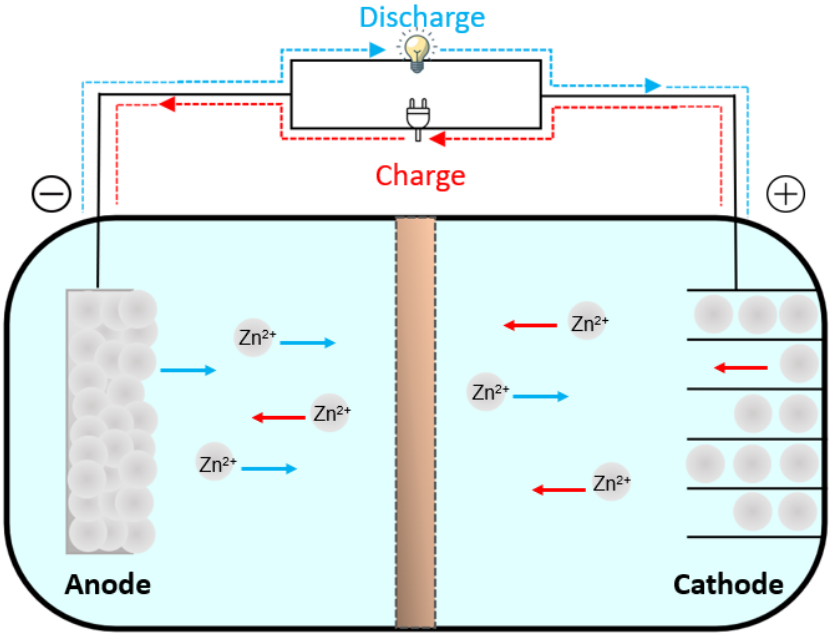

Figure 1.4: general scheme of a zinc ion battery

During the discharging process, the anode releases zinc ions in the solution. The ions move towards the cathode, where they are intercalated in the material structure. Therefore, the intercalation is a necessary process to maintain the electroneutrality of the system during the reaction. The opposite process occurs during the charging process and zinc ions are reduced at the zinc electrode, while zinc ions are released from the cathode.

The choice of the electrolyte has a strong influence on the performance and life cycle of the battery. This is mainly due to the formation of byproduct like ZnO and $Zn(OH)_2$.[27] For these reasons, the electrolytes must have several properties, such as electrochemical and chemical stability at high and low voltages and good ion conductivity. The electrolytes can be aqueous or non-aqueous. Among the aqueous electrolytes available, $ZnSO_4$ has shown better performance due to the reversibility of Zn plating.[28] Moreover, it has been shown that low zinc-ion concentration in the electrolyte is beneficial for positive electrode materials, whereas high concentration leads to phase transition.[27]

1.5. PBAs

The first purely synthetic pigment was Prussian blue. This compound was synthesized for the first time in Berlin as *Caeruleum Berolinense*.[29] Its discovery was by mistake. Johann Conrad Dippel, a German alchemist, was extracting cochineal with alum ($KAl(SO_4)_2$), iron sulfate and potash. By contamination of the potash with hexacyanoferrate, a blue precipitate was produced when the iron solution was added. The first synthesis procedure was reported in Philosophical Transactions of the Royal Society by John Woodward (1657–1728). Prussian blue was subsequently used as a pigment in paintings or photographs in the 18th and 19th centuries.[30]

Prussian Blue Analouges, in the last decade, have attracted great attention as electrode material for metal-ion battery. What make them attractive are the easy and inexpensive synthesis procedure, the high specific capacity for the reversible insertion of a variety of metallic ions and the high safety and nontoxicity.[13]

Hexacyanometallates, often referred to as PBAs, are materials constituted by an open framework face-centered cubic lattice, having an *fm3m* space group. The nominal formula of this class of materials can be written as:

$$A_xM[M'(CN)_6]_{1-y}\ \gamma_y \cdot wH_2O$$

where, A is an alkaline cation, M and M' are transition metal ions coordinated octahedrally to the nitrogen atoms and the carbon atoms of the cyanide group, respectively, and γ the hexacyanometallate complex vacancy (the primer defect of such crystallographic structure).[32] Each unit cell consists of eight subunits (i.e. interstitial sites/subcells) that are able to accommodate neutral species and/or cations. PBA crystal structures (Figure 1.6) are characterized by large interstitial sites, often called 'A sites', and large channels in the 100 directions, which are responsible for the high solid diffusion coefficient (10^{-9} to 10^{-8} cm^2 s^1) and ionic conductivity of this class of materials.[13, 32] As a consequence, different PBAs having different transition metals in their lattice can reversibly (de-)insert a variety of monovalent (e.g. Na^+, Li^+, K^+, etc.), divalent (e.g. Zn^{2+}, Mg^{2+}, Ca^{2+}, etc.), and trivalent cations (e.g. Al^{3+}).[13, 32, 33]

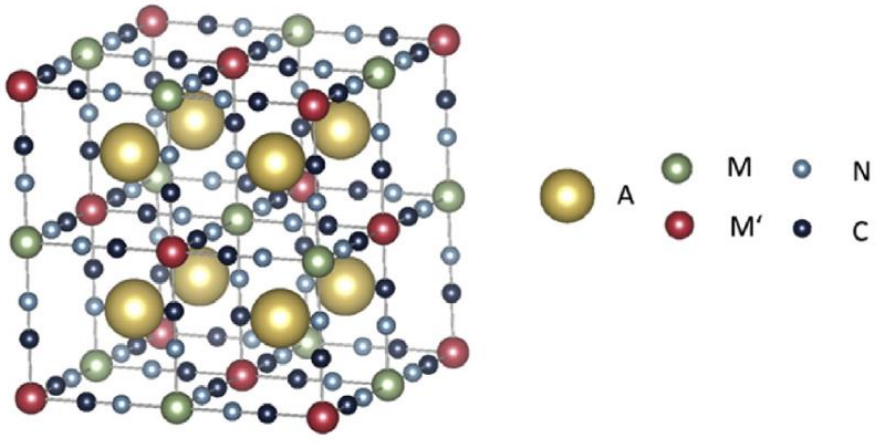

Figure 1.5: crystal structure of Prussian blue analouges.

1.6. Copper Hexacyanoferrate

Different materials belonging to the PBA family are promising candidates as cathode electrodes in a variety of metal-ion battery applications: from organic-based Na-, K-, and Zn-ion to aqueous Li-, Na-, K-, Zn-, Mg-, Al-, Ca-ion batteries.[32, 33] Among Prussian blue analogues, copper hexacyanoferrate (CuHCF) has been shown to be a promising candidate as positive electrode material for aqueous zinc ion batteries (ZIBs). Due to its high average working potential (c.a. 1.7 V vs Zn/Zn^{2+}) and its excellent power rate capability, together with low toxicity and costs, make it is suitable for power grid applications.[34] Moreover, CuHCF can be synthesized through an easy synthesis route, which makes its industrial large scale production feasible.[13] As other prussian blue analogues (PBAs), CuHCF has an open framework face-centered cubic lattice crystal structure with large interstitial sites as well (Figure 1.6).

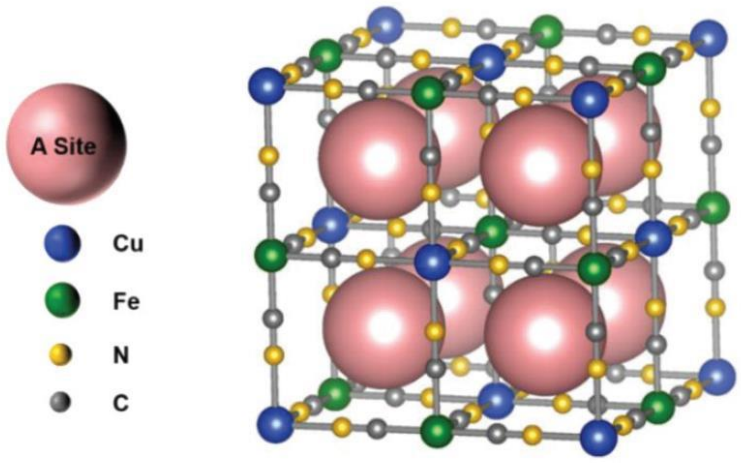

Figure 1.6: CuHCF crystal structure [35]

The cell consists of eight subcells, where the A sites have a diameter of 4.6 Å. Combined with a channel diameter of 3.2 Å, the structure offers diffusion coefficients for ionic species varying from 10^{-9} to 10^{-8} $cm^2\ s^{-1}$, which allows fast and reversible (de-)insertion of multivalent ions (e.g. Zn^{2+}) in the lattice.[35] Here, Cu^{2+} is bonded to the nitrogen and Fe^{3+} to the carbon ends of the cyanide group, due to the larger ionic radius of Cu^{2+} (87 pm) compared to Fe^{3+} (78.5 pm).[35, 36]

2. AIM OF THE WORK

Over the last years, aqueous Zn-ion batteries (ZIBs) have brought great interest due to their applicability as cheap and environmentally friendly energy storage devices for power grid applications[13]. Among the potential active materials, which can be used in this type of battery[58], open framework Prussian Blue (PB) and its analogues (PBAs) have attracted the attention of the researchers thanks to their excellent properties. Because of the large interstitial sites, PBAs facilitate the reversible intercalation of hydrated ions from an aqueous electrolyte[59]. Belonging to the Prussian blue analogues (PBAs) family, copper hexacyanoferrate (CuHCF) has been shown to be a promising candidate as positive electrode material for aqueous ZIBs. In addition, CuHCF can be synthesised through a simple synthesis. Despite CuHCF can be produced through an easy co-precipitation route, the synthesis of the desired phase is not straightforward to control[14]. Such complications in controlling the synthesis' reaction mechanism have been evaluated in previous studies[66].

The measurements carried out with zinc as the reference electrode differ in terms of life cycle from the measurements made with Ag / AgCl as RE. These results led to the consideration that the potassium chloride solution of the reference electrode somehow plays a role in the life span of the electrode due to potential losses of the solution in the electrolyte. For this reason, it was decided to further evaluate the role of the electrolyte. Therefore, the purpose of this thesis is to investigate the effect of the presence of potassium chloride as an electrolyte in the co-presence of zinc sulfate. Furthermore, the effect of an excess of potassium ions in the synthesis of the material was also evaluate.

3. THEORETICAL PRINCIPLES

To better understand the results obtained in this thesis, it is appropriate to briefly describe some theoretical aspects concerning both the models of mass transport that characterize the electrode processes [37] and the nature and types of responses obtained from the use of some particular electroanalytical techniques using working electrodes of micro and nano size.[37, 38]

3.1. Diffusion

The experimental conditions that lead to the realization of a diffusive mass transport of an electroactive species involve the use of stationary electrodes, in a still solution and containing a relatively high amount of supporting electrolyte [39]. In conditions of mass transport governed by diffusion alone, the concentration (and therefore current) profiles as a function of time depend on the particular geometry of the electrode.

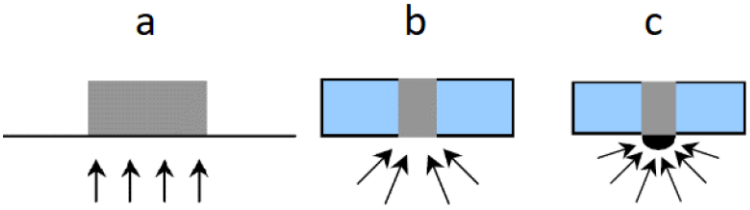

Figure 3.1: Flow lines for electrodes of different geometries a) conventional plane electrode b) disk microelectrode inserted in an infinite insulating plane c) hemispherical microelectrode in an infinite insulating plane.

As is known, for electrodes of conventional dimensions the condition of semi-infinite linear diffusion to a plane electrode is assumed to be valid, where the edge effects are neglected.[37] In this case the flux depends only on the direction perpendicular to the electrode surface (Figure 3.1). As the size of the electrode decreases, the edge effects can no longer be neglected and the equations that describe the flow become more complex.[40]

3.2. Diffusion for different electrode geometries

Diffusion to a semi-infinite plane electrode

Consider the generic reversible electrode reaction:

$$Ox + ne^- \leftrightarrow Red \qquad (1)$$

The expression of the variation of the Ox species concentration as a function of time is obtained from Fick's second law in one dimension[42]:

$$\frac{\partial C_{Ox}(x,t)}{\partial t} = D_{Ox} \frac{\partial^2 C_{Ox}(x,t)}{\partial x^2} \qquad (2)$$

where D_{ox} is the diffusion coefficient of the electroactive species initially present in solution, x is the distance from the electrode surface in the direction perpendicular to it, C_{ox} is the concentration of the electroactive species in oxidized form. The faradic current will be given by the combination of the flow with Faraday's law [37]:

$$\frac{i(t)}{nFA} = D_{Ox} \left[\frac{\partial C_{Ox}(x,t)}{\partial x}\right]_{x=0} \qquad (3)$$

where F is Faraday's constant, equal to 96500 C × mol^{-1}, *i(t)* is the instantaneous current, n the number of electrons exchanged, A the area of the electrode; the term x = 0 indicates the flow at the electrode surface. To obtain the current it is necessary to find an analytical solution for the concentration gradient at the electrode surface. In a chronoamperometric experience for a flat electrode, the equation resulting from the solution of equation (2) and subsequently from the application of equation (3) is given by the well-known Cottrell equation [37].

$$i(t) = \frac{nFAD_{Ox}^{\frac{1}{2}} C_{Ox}^{b}}{\pi^{\frac{1}{2}} t^{\frac{1}{2}}} \qquad (4)$$

where t is the time, C_{Ox}^{b} is the concentration of the electroactive species in the bulk of the solution and the other symbols have their usual meaning. A typical time-current profile to a flat electrode is shown in Figure 3.2 (black line).

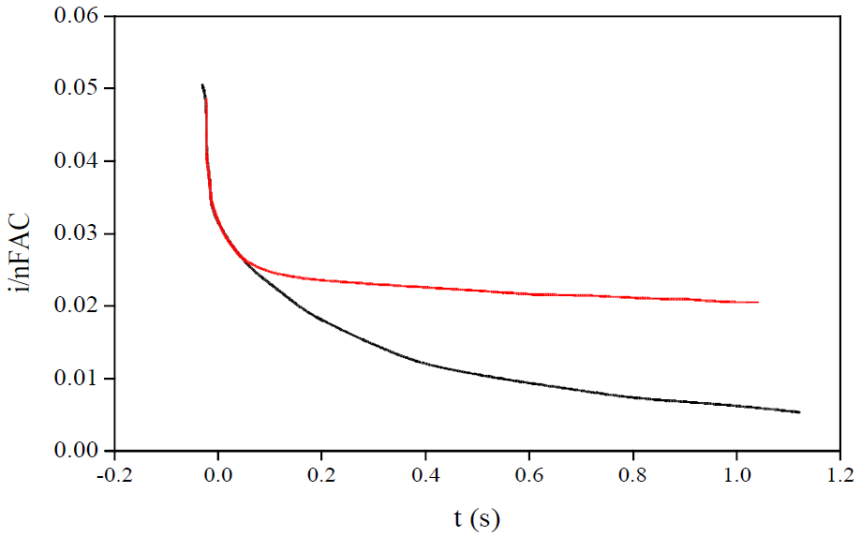

Figure 3.2: Current-time response for a chronoamperometric experience of electrodes a different geometries, plane (black line) and hemispherical (red line).

3.3. Diffusion to a hemispherical microelectrode

The electrode geometry considered is the one schematized in Figure 3.1 The rigorous expression of the concentration profile as a function of time is determined on the basis of Fick's second law in spherical coordinates [37]:

$$\frac{\partial C_{Ox}(r,t)}{\partial t} = D_{Ox}\left[\frac{\partial^2 C_{Ox}(r,t)}{\partial r^2} + \frac{2}{r}\frac{\partial^2 C_{Ox}(r,t)}{\partial r}\right] \quad (5)$$

where r is the radial direction, and the other symbols have their usual meaning. Also, in this case the resolution of the differential equation is relatively simple as the concentration profile depends only on the radial coordinate r. The solution of the

differential equation (5), after combining the flow at the electrode surface with the Faraday equation, provides the following relationship [37]:

$$i(t) = \frac{nFAD_{Ox}^{\frac{1}{2}}C_{Ox}^{b}}{\pi^{\frac{1}{2}}t^{\frac{1}{2}}} + \frac{nFAD_{Ox}C_{Ox}^{b}}{r} \quad (6)$$

where r is the electrode radius. Two terms appear in this equation: the first function of time and the second independent of the latter. From equation (6) we can derive two limit cases, corresponding to times tending to zero and infinity. It can be shown that the limit of equation (6) for t → 0 is identical to the Cottrell equation (4). For t = ∞ (or in the case of an electrode with a very small radius r), the transient term tends to zero, and expression (6) takes the following form [40]:

$$i = 2\pi nFD_{Ox}C_{Ox}^{b}r \quad (7)$$

that is, the current, at a given concentration of the electroactive species and for a given electrode, is constant over time.

Figure 2.2 (red curve) shows the entire current-time profile at a hemispherical microelectrode. This profile differs from that observed with conventional electrodes for the achievement of a steady state over a long time.

3.4. Diffusion to a disk microelectrode

The rigorous expression of the concentration profile as a function of time for a disk microelectrode (Figure 3.1) is obtained from the resolution of Fick's law in cylindrical coordinates [41]:

$$\frac{\partial C_{Ox}}{\partial t} = D_{Ox}\left[\frac{\partial^2 C_{Ox}}{\partial r^2} + \frac{1}{r}\frac{\partial C_{Ox}}{\partial r} + \frac{\partial^2 C_{Ox}}{\partial z^2}\right] \quad (8)$$

where D_{Ox} is the diffusion coefficient of the electroactive species present in solution, r is the radial dimension with origin in the center of the disc, while z is the direction perpendicular to the electrode surface (Figure 3.3).

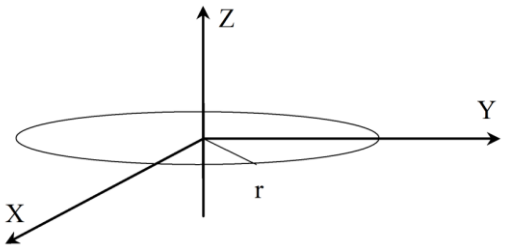

Figure 3.3: The disk represents the electroactive surface with the reference system adopted.

The solution of the differential equation (8) is very complex; however, approximate numerical solutions are known which are obtained by resorting to digital simulation methods [40].

These solutions represent in a sufficiently accurate way the current / time responses for this electrode geometry. Among the various numerical solutions proposed, we can recall the one proposed by Shoup and Szabo, an empirical equation, defined as follows [42]:

$$i = 4nFD_{ox}aC_{ox}^{b}f(\tau) \quad (9)$$

where $f(\tau)$ is expressed by the following equation:

$$f(\tau) = 0.7854 + 0.8862 \cdot \tau^{-\frac{1}{2}} + 0.2146 \cdot e^{-0.7823 \cdot \tau^{-1/2}} \quad (10)$$

$$\tau = \frac{4D_{ox}t}{a^2} \quad (11)$$

and a represents the radius of the micro disc.

Expression (9) is valid throughout the time interval with an accuracy of 0.6% [43].

It can be shown that for t → 0, the relations (9) (10) are reduced to the Cottrell equation, while for t → ∞ the following equation is obtained:

$$i = 4nFD_{ox}aC_{ox}^{b} \quad (12)$$

where a is the disk radius. Note that equation (12) is similar to (7) apart from the factor 2π, replaced by the factor 4. This difference allows to distinguish the current-time profiles of the two different types of microelectrode [40].

3.5. Voltammetric methods

The equations reported in the previous paragraph are valid for chronoamperometric measurements. Theoretical relationships for both conventional and microelectrodes can also be derived for voltammetric techniques. Among these, the most important are linear scanning voltammetry (LSV) and cyclic voltammetry (CV). For simplicity, in this part we will describe the potential current profiles that are obtained only in a qualitative way [37].

For a conventional electrode, characterized by planar diffusion, profiles such as the one shown in Figure 3.4 are obtained in the case of cyclic voltammetry.

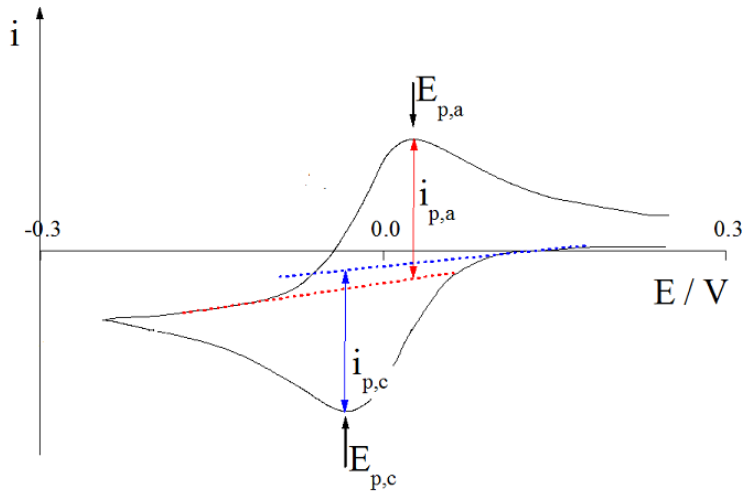

Figure 3.4: Cyclic voltammogram recorded with conventional electrodes.

The most important parameters of these diagrams are: cathode peak (Ep, c) and anodic (Ep, a) potentials, cathode peak (ip, c) and anodic (ip, a) currents, indicated in Figure 3.4. The analysis of these parameters as the scanning speed varies, allows to establish the nature of the electrode process, and in particular the reversibility of the heterogeneous charge transfer, and any associated chemical reactions. From an analytical point of view, the most important parameter is the peak current, which for a diffusive and reversible process is expressed by the following equation [37]:

$$i_p = Kn^{3/2} AD^{1/2} Cv^{1/2} \quad (13)$$

where K is a constant, (at 25 ° C K = 2.69x105), v is the scanning speed, A is the electrode surface and other symbols have their usual meaning. Equations related to the profiles were also obtained for the microelectrodes current / potential. However, while for the spherical and hemispherical shaped microelectrodes there are rigorous analytical solutions [37], for disk microelectrodes it has been possible obtain results only with numerical methods. For the latter electrode geometry, an approximate equation, but sufficiently accurate (the error is <0.23%), which

describes the maximum current, as a function of the scanning speed, is as follows [44]:

$$\frac{i}{4nFcDr} = 0.34\exp(-0.66p) + 0.66 - 0.13\exp\left(-\frac{11}{p}\right) + 0.351p \quad (14)$$

where i is the observed maximum or peak current, p is a dimensionless parameter defined as follows:

$$p = \left(\frac{nFr^2v}{RTD_0}\right)^{1/2} \quad (15)$$

where the different symbols have their usual meaning. For very fast scan speeds, voltammograms recorded with a microelectrode take the same shape as those recorded at a plane electrode conventional dimensions (see Figure 3.5a). For slow scanning speeds, the current-potential results like that shown in Figure 3.5b, characterized by the fact that in both direct and reverse scanning, sigmoidal forms are obtained which overlap, characterized by the presence of a state current plateau stationary. [40]

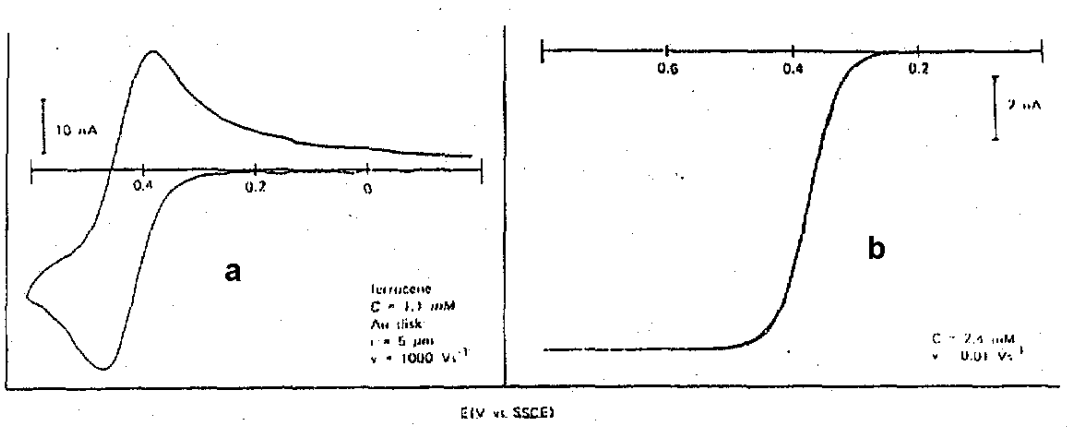

Figure 3.5: Cyclic voltammograms relating to the oxidation of ferrocene in a 0.6M solution TEAP / acetonitrile, recorded on a gold disc microelectrode (r = 5 µm); a) speed of scanning = 1000 V / s, b) scanning speed = 0.01 V / s.

If the value of the parameter p <0.076, the diffusion limit current obtained by LSV or CV is identical to that obtainable from equation (12). For values of p parameter greater, the diffusion current is higher due to a additional contribution due to planar diffusion [44].

Table 3.1 shows, for some values of p, the relative percentage contributions of semi-infinite planar diffusion which is added to the steady state current value [44].

Table 3.1: parameters and relative % of planar diffusion contribution.

p	% planar diffusion
0.6	10%
0.33	5%
0.21	3%
0.076	1%

3.6. Thin layer voltammetry

Thin layer voltammetry is carried out in conditions in which a thin layer of electrolytic solution is contained between the electrode and the wall of the electrochemical cell generally at a distance of less than 100 microns. Figure 3.6 shows a typical thin layer electrochemical cell scheme.

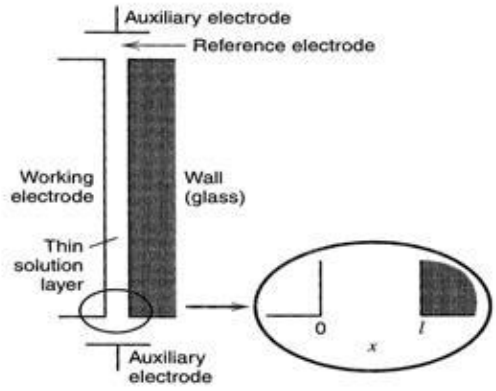

Figure 3.6: Typical cell configuration for thin layer voltammetry. [37]

Under these conditions, in many voltammetric measurements, the thickness of the solution film (1) is less than the thickness of the diffusion layer. That is:

$$l < (2D_{Ox})^{1/2} \quad (16)$$

The consequence of this cell configuration is that all the Ox species turns into Red or vice versa; by changing the direction of the potential Red it can be converted back to Ox. A thin-layer cell behavior implies, in other words, that the phenomena related to the mass transport of both Ox and Red are practically absent, and that the concentration of Ox and Red at each potential are uniform in the solution layer considered. A cell-to-thin-layer behavior means that the principles related to the electrode process are different from those seen previously.

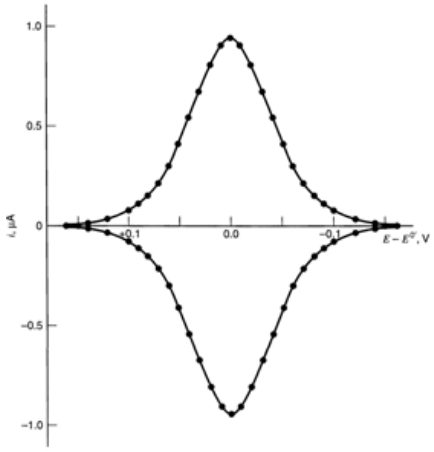

Figure 3.7: relates to a reversible process.

Considering in particular the voltammogram shown in Figure 3.7, some parameters that characterize it can be defined:

The peak potential (E_{pc}) has a value corresponding to the formal potential, therefore E_{pc} = E^{0}'. The peak current (i_{pc}), given by equation 17:

$$\mathrm{i_{pc}} = \frac{\alpha \mathrm{F^2 V v C^*_{Ox}}}{4\mathrm{RT}} \qquad (17)$$

Where V is the volume of electrolyte involved and the other symbols have their usual meaning. From this equation it is observed that the peak current is proportional to the concentration of the analyte and the scanning speed. Therefore, a quick diagnostic criterion for establishing whether a voltammetric wave has a thin layer

behavior is to verify that i_{pc} is linearly dependent on *v*. On the other hand, the area underlying the peak (anodic or cathodic) corresponds to the charge Q involved in the electrolysis of the analyte present in the thin layer. Therefore, on the basis of Faraday's law, it corresponds to the number of moles of the electrolyzed analyte, obtainable from the following equation:

$$Q = nFN_0 \quad (18)$$

Where N_0 is the number of moles of the species that oxidize or reduce.
For an irreversible process, the current and the potentials of the peaks depend not only on the parameters seen above, but also on the transfer coefficient α and the charge transfer constant k_0. In particular, i_{pc} is given by the relation:

$$i_{pc} = \frac{\alpha F^2 V v C_{Ox}^*}{2.718RT} \quad (19)$$

While, the peak potential (E_{pc}) is given by:

$$E_{pc} = E^{0\prime} + \frac{RT}{\alpha F} \ln\left(\frac{ARTk^0}{\alpha F V v}\right) \quad (20)$$

Where the symbols have their usual meaning. From equation (19) it is observed that also in this case the i_{pc} linearly depends on both the concentration and the scanning speed, a behavior similar to that observed for a reversible process. As regards E_{pc}, it is displaced with respect to the $E^{0'}$ value by a quantity that depends on both the transfer coefficient and the charge transfer kinetics constant. The peak area, even in these conditions, corresponds to the number of moles of electrolyzed substance. Based on the thin layer model, relations are also derived that identify adsorption phenomena of a species involved in an electrode process.

3.7. Principles of the SECM

Scanning electrochemical microscopy or SECM briefly[42] is a technique that allows to carry out chemical and chemical-physical investigations on various types of surfaces, and at the interphase of solid / liquid, liquid / liquid, liquid / gas.

This technique is based on the controlled movement of a voltammetric microelectrode[45] near the surface under study (see Figure 3.8A). The measured signal is the faradic current associated with the oxidation / reduction of an electroactive species present in the solution which, with the sample surface, forms the interface under examination.

The fundamental aspect of SECM is that the signal is perturbed in a reproducible mode based on the distance between the sample surface and the microelectrode. This perturbation is related to the fact that the sample surface can constitute both an impediment to the transport of matter towards the electrode (see Figure 3.8B), and a local source of electroactive species (see Figure 3.8C) [42].

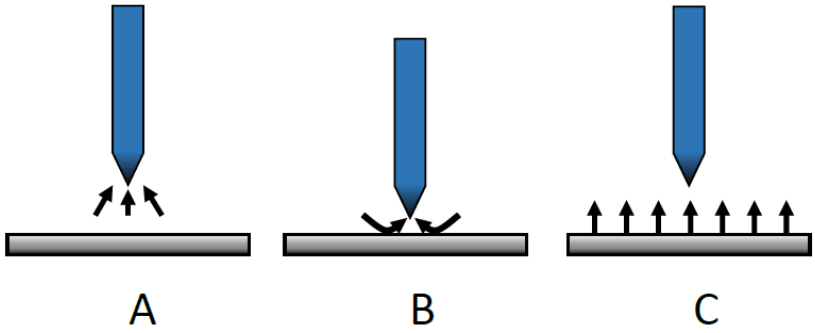

Figure 3.8.: Effect of the approach of the microelectrode to the surface on the diffusion of the electroactive species.

The scheme of a typical SECM instrument consists of a microelectrode [45], that is an electrode with a radius ≤ 25 μm, a reference electrode and a potentiostat (or bipotentiostat) for controlling the potential applied to the working electrode and / or independently of the substrate under examination, if it is a conductor. The electrodes are immersed in the solution contained in a cell whose bottom consists of the investigated surface. The potentiostat is normally interfaced with a computer for the

acquisition of current and potential signals and processes them for a two or three dimensional representation.

What distinguishes SECM equipment from a conventional electrochemical circuit is the presence of micropositioners that allow you to place the probe electrode in space with extreme precision.

3.8. SECM methodologies

In the SECM context, there are several operating modes that can be classified on the basis of the type of displacement of the probe electrode in space [42]. The main ones are:

Feedback mode:
the microelectrode is moved away and approached perpendicularly to the surface (Z axis)

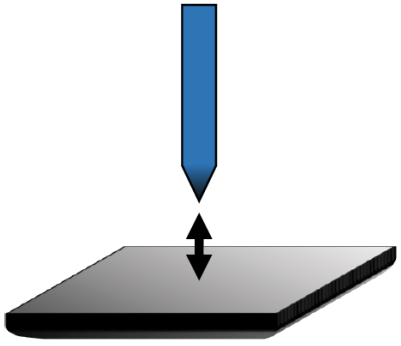

Scanning mode: the microelectrode, placed on the z axis near the surface, comes translated parallel to the surface on the X and Y axes.

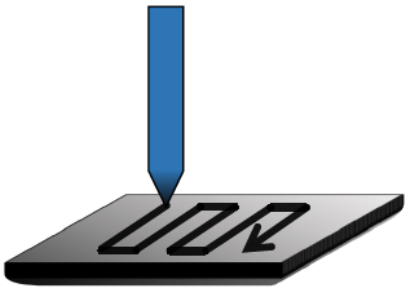

Proximity mode: the microelectrode is brought as close as possible to the surface where
the variations of the chemical-physical phenomena that take place at the interphase are recorded.

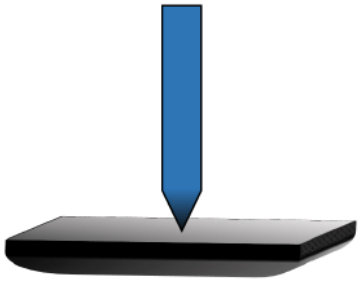

Working in feedback mode, data is obtained that allow the construction of approach curves [42], in scanning mode it is possible, through the re-processing of the acquired data, to build an image of the surface with micro and nanometric resolution; in proximity mode, in addition to recording the phenomena at the interphase, the microelectrode can intervene directly on the surface itself, causing, for example, the solubilization of the material, the electrolytic deposition of metals, or the electrodeposition of polymeric material [42].

3.9. Tilting

Theoretically we can imagine that the microelectrode is moving perfectly perpendicular to the surface. However, the microelectrode can have a certain

inclination as its surface is unlikely to be perfectly perpendicular to the substrate. These phenomena must be taken into account with very large RG as the insulating part of the microelectrode may touch the substrate first. In this case, there would always be space between the electrode and the surface that would allow the species to pass and the current value of zero (negative feedback) or infinite (positive feedback) would rarely be reached. The case of tilting can also occur with small RGs but the distance between the microelectrode and the substrate is smaller. Hence the phenomenon is minimized.

Figure 3.9: comparison for a large RG (right figure) and a small RG (left figure) in case of tilting.

3.10. Applications of the SECM

The SECM is able to combine the spatial resolution offered by the positioning system and the analytical sensitivity typical of microelectrodes [45]. Thanks to these properties, SECM has been used to perform studies in various scientific fields. Just to cite a few examples, with SECM it was possible to selectively study the flow of numerous chemical species through porous membranes, following the permeability variations in different conditions[46], identifying the surface distribution of the catalytic sites, following the concentration variations of the electroactive species near the

surface itself [47]; mass transfer phenomena can also be studied at the liquid-liquid interphase of two immiscible liquids, or at the air-liquid interphase, thanks to the possibility of placing the working electrode exactly at the interphase without altering its chemical-physical properties [47].

Interesting applications have also been reported in biological systems both to identify the transport mechanisms and the permeability of membranes of biological tissues themselves [48], and to study redox processes on biological surfaces such as, for example, photosynthesis processes and activity of enzymes immobilized on solid surfaces[49]. SECM has been used to study a large number of both heterogeneous and homogeneous electrode processes at the solid-liquid and air-liquid interphase[48]. Finally, this technique has recently found application in the study of the photochemical and photocatalytic properties of many semiconductors and nanocomposites containing semiconductors.

3.11. Microelectrodes for SECM

In most SECM applications, the microelectrodes used have disk geometries. Therefore, many of the considerations that will be described below will refer to this electrode geometry.

3.11.1. The RG parameter

The resolution of the SECM depends on the RG parameter defined by the following relationship:

$$RG = R/a \quad (21)$$

where R is the radius of the electrode tip (insulator + electrode), while a is the radius of the microdisk as indicated in Figure 3.10. The RG parameter is a geometric parameter and is given by the shape of the tip of the microelectrode. RG is in fact defined as the ratio between the diameter r of the tip, which includes both the active part and the insulating part (glass) around it, and the radius of the electrode a (Equation 21). The microelectrodes used to make SECM measurements are generally made a conical tip shape to try to make the RG parameter small.

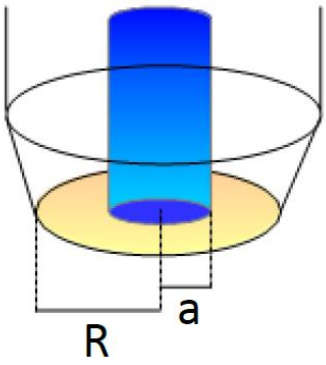

Figure 3.10: Scheme of a microelectrode where the values of R and a are identified to determine the RG parameter.

Diffusion to a disk-shaped microelectrode can also be influenced by the RG parameter as shown in Figure 3.11 [50].

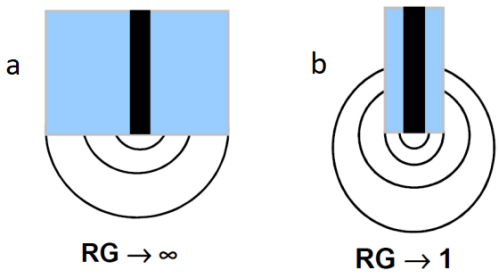

Figure 3.11: schematic representation of the possible types of flux that are established at the surface of the microelectrode as a function of the RG parameter. a) RG large, the diffusion profile is almost hemispherical b) RG → 1 the diffusion profile is almost spherical.

With RG tending to infinity, the edge effects are limited to the adjacent area below the electrode plane; in these conditions, as previously seen, an almost hemispherical diffusion profile is obtained (Figure 3.11 a).
For small RG, that is, when the thickness of the insulation is of a size comparable to the electrode beam, a flow of matter is established also from the upper area with respect to the plane of the electrode itself. Under these conditions, the diffusion profile tends to assume an approximately spherical shape (Figure 3.11 b) and the mass transfer coefficient is higher than that relating to the condition of Figure 3.11 a. The steady state currents associated with this last type of geometry are, all other conditions being equal, higher than those predicted on the basis of equation (12) [50, 51]. Also for these electrode geometries there are equations that allow to express the value of the steady state currents [51].

3.12. Feedback effects

The steady state current to a microelectrode is affected by the presence of the surface of the substrate studied when the distance separating the latter from the microelectrode is less than the diffusion layer [52].
If the microelectrode is located at a distance from the surface less than ten times the electrode radius, two different results are obtained depending on the type of surface and the working conditions to which the surface itself is subjected. If the latter is an insulator, the steady state current of the microelectrode decreases as it approaches the surface from the bulk of the solution. This phenomenon, associated with an impediment to diffusion, is called negative feedback [42] (see Figure 3.12).

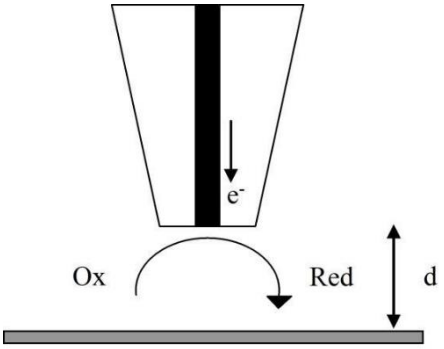

Figure 3.12: Schematic representation of negative feedback.

If the surface studied is made of a conductive material of relatively larger dimensions than the surface of the microelectrode, or a potential is applied to it such as to give rise to electrode processes with the probe molecule, (see Figure 3.13), the steady state current it will grow as the distance that separates the microelectrode from the surface decreases. In this case the phenomenon is called positive feedback. [42]

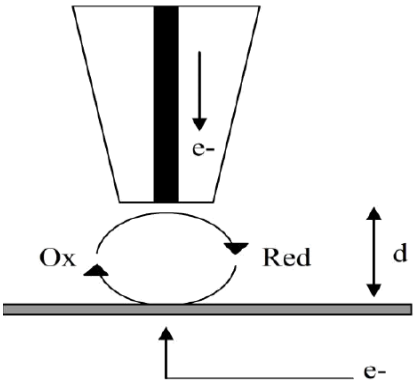

Figure 3.13: Schematic representation of positive feedback.

3.13. Approach curves

To know the position of the microelectrode relative to the sample surface, current-distance curves called approach curves are generally constructed [53]. These are obtained by reporting the values of the steady state current, i_M, obtained for different positions assumed by the microelectrode on the axis perpendicular to the surface,

as a function of the distance. In order to have independent approach curves from the electrode radius and the concentration of the redox mediator and parametric to RG, the values of current i_M and electrode-substrate distance d, are normalized respectively for the current $i_{L,\infty}$ recorded in the bulk of the solution, i.e. when the microelectrode is located at a sufficiently high distance not to perceive the presence of the surface (i.e. the current given by equation (12)), and for the electrode radius. In other words, the approach curves are nothing more than i_M / i_L vs L diagrams with:

$$L = \frac{d}{a} \quad (22)$$

The theoretical approach curves can be derived from the differential equations already presented in the previous paragraphs for each electrode geometry, imposing the appropriate initial and boundary conditions that characterize the feedback phenomena. The solutions of the differential equations that describe the flow for feedback phenomena are extremely complex and are generally not solved analytically. At the moment, the quantitative description, in terms of current, of the two feedback phenomena is obtained by means of digital simulation procedures [54]. Based on these procedures, approximate analytical equations (23) and (24) were derived, for a fast, reversible and diffusion-controlled electrode process. In conditions of negative feedback we have:

$$\frac{i_{SS}}{i_{L,\infty}} = \frac{1}{k_1 + \frac{k_2}{L} + k_3 e^{\frac{k_4}{L}}} \quad (23)$$

where k_1, k_2, k_3, k_4, are constants that depend on the parameter RG.

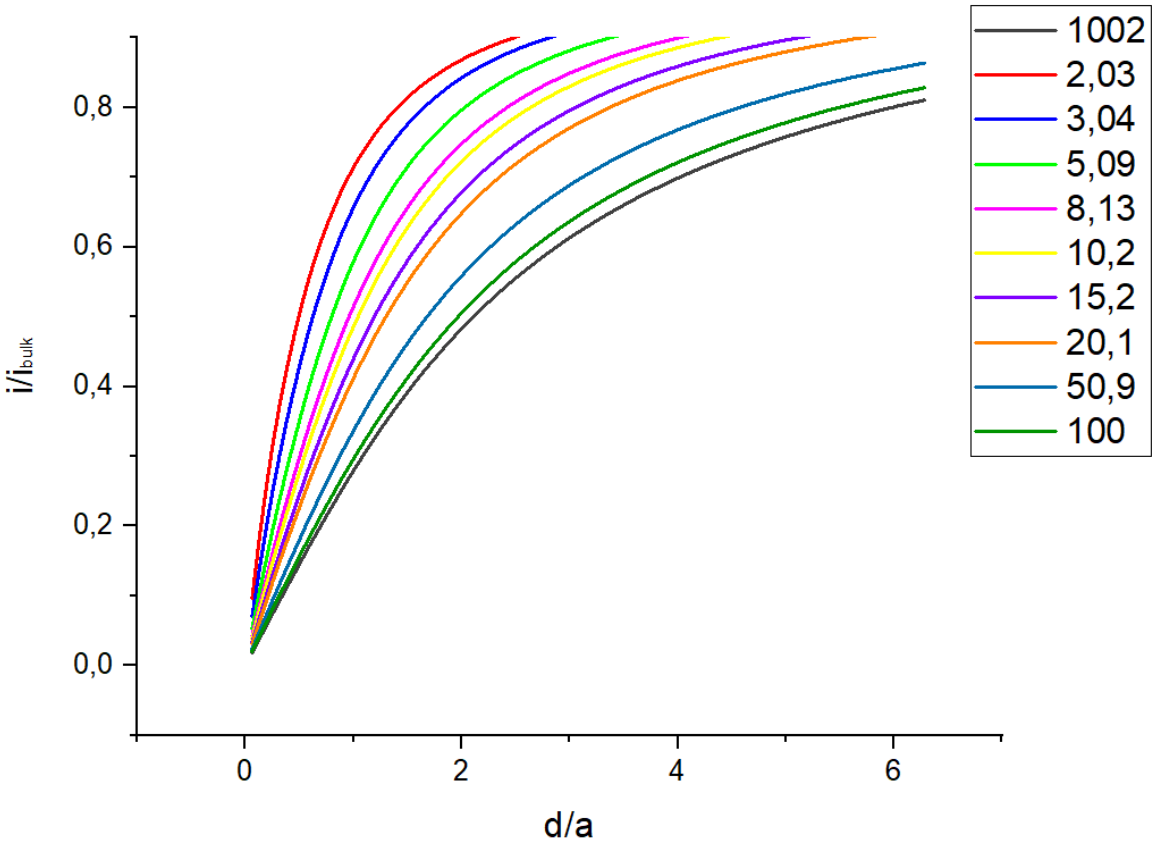

Figure 3.14: Theoretical approach curves under negative feedback conditions obtained for different values of the RG parameter.

From Figure 3.14 it is observed that for large electrode-surface distances studied (L large), the RG parameter has relatively little influence; this is evident from the relatively low slope of the curves at a given value of L. For small values of L, the parameter RG significantly affects the slope of the curve. In particular, as RG decreases the current variation is higher and this indicates a greater sensitivity in the z direction of the voltammetric probe for the same distance from the surface.
In case of positive feedback, the relationship obtained is as follows:

$$\frac{i_{SS}}{i_{L,\infty}} = k_1 + \frac{k_2}{L} + k_3 e^{\frac{k_4}{L}} \quad (24)$$

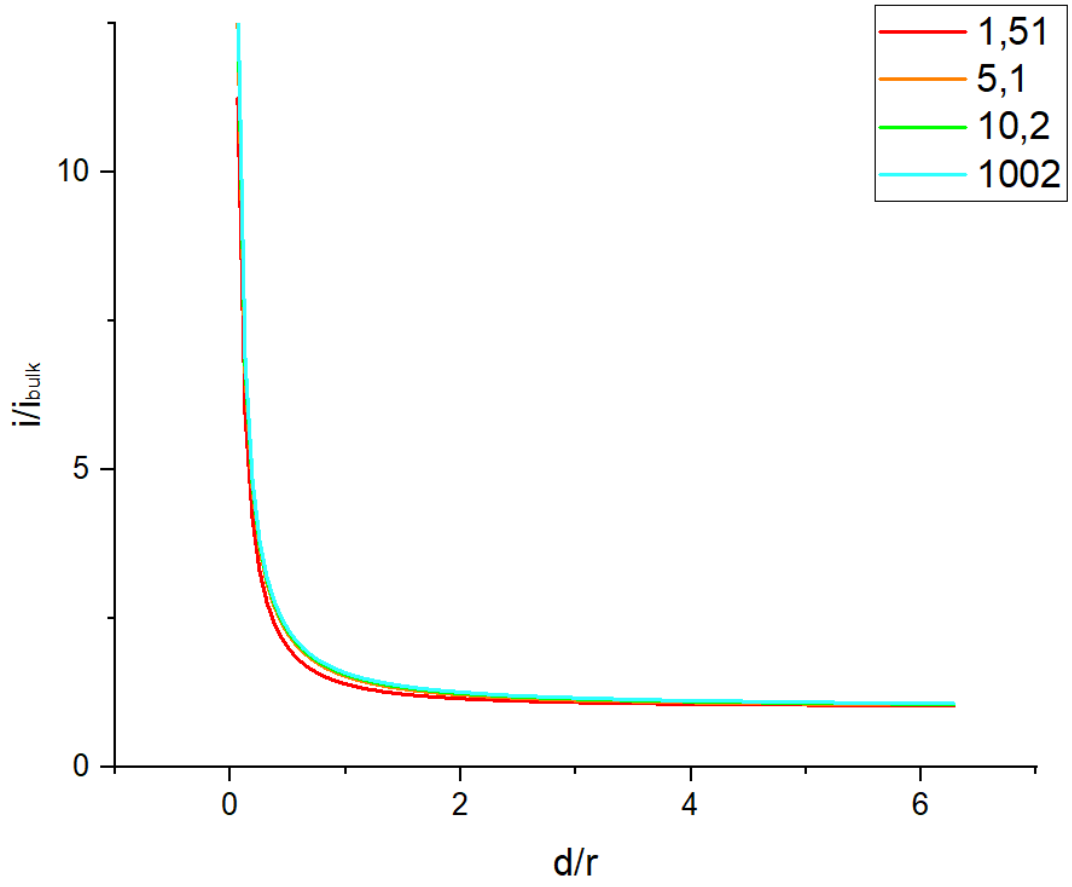

Figure 3.15: Theoretical approach curves in conditions of positive feedback obtained for different values of the parameter RG.

The resulting approach curves have the form shown in Figure 3.15. As this last figure highlights, for positive feedback phenomena, the RG parameter is relatively unimportant in determining the shape of the approach curve. In fact, both for large and small L values, the working electrode is, respectively, little or very sensitive regardless of the RG value.

The approach curves are extremely useful from a practical point of view since, once constructed, an electrode-surface distance is associated with each current value. In fact, knowing the electrode radius, it is possible to trace the electrode-surface distance through the relations (23) - (24).

Furthermore, the shape of the curves acquired experimentally provides indications on the nature of the electrode process both at the surface of the microelectrode and at that of the substrate. It also allows, through the comparison with the theoretical curves, to obtain quantitative information in the kinetics involved, both heterogeneous and homogeneous.

3.14. Galvanostatic technique with potential limitation

In this technique a constant current is applied while recording the variation of the potential in a predetermined interval, such as to include the electrode processes of interest [37]. Figure 3.16 shows typical waveforms applied to the working electrode and related responses obtained.

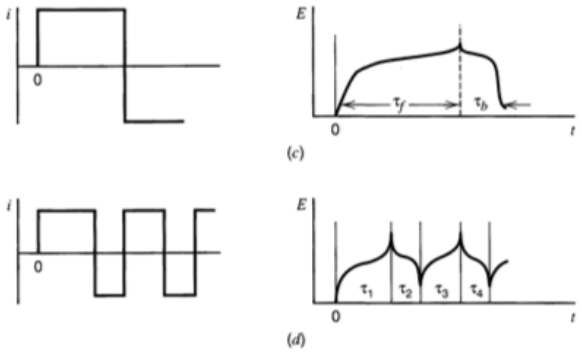

Figure 3.16: Controlled current techniques: chrono potentiometry with current inversion c), cyclic chronopotentiometry d).

This technique is used in the study of battery performance and allows to obtain the charge involved in the charge and discharge processes, the capacity (*Q*) and the coulombic efficiency after having performed a certain number of charge and discharge cycles. Based on the amount of material responsible for the accumulation process, a theoretical capacity (*Qt*) is also defined. These characteristics have quantitative definitions as shown below.

The amount of charge (*q*) of charge (or discharge) is simply obtainable from the relation:

$$q = I \cdot t \quad (25)$$

where I is the applied constant current intensity, *t* is the time elapsed to reach the predetermined potential limit.

The theoretical capacity of an electrochemical cell is the amount of electric charge theoretically stored in the cell [53]; is expressed by equation (26),

$$Qt = \frac{nF}{3.6\ x\ MW} \quad (26)$$

where n is the number of electrons exchanged per unit of formula, F is Faraday's constant and M.W. is the molecular mass of the material.

In the specific case, the theoretical capacity of CuHCF in a ZIB, assuming a molar mass of 310.316 $gmol^{-1}$, is equal to 86.38 $mAhg^{-1}$ [53].

When a battery is subjected to charge and discharge cycles, it undergoes the phenomenon of aging, with loss of capacity. This phenomenon can be represented in numerical terms on the basis of the amount of charge retained after a certain number of charge and discharge cycles. Therefore, the capacity retention (RC) of the battery can be calculated from the following relation [53]:

$$RC = \frac{capacity\ at\ the\ last\ cycle\ of\ descharge}{maximum\ discharge\ capacity} \quad (27)$$

3.15. Thermodynamic analysis

As mentioned above, for CuHCF positive electrodes, charging implies the deinsertion of zinc-ions from the lattice, whereas discharge implies the insertion of zinc-ions in the lattice.[35] The electrochemical reactions for aqueous Zn-ion batteries with CuHCF as cathode and metallic zinc as anode can be described by equation 2 and 3, respectively.[55]

$$KCuFe^{3+}(CN)_6 + xZn^{2+} + 2xe^- \underset{ox/ch}{\overset{red/dis}{\rightleftharpoons}} Zn_xKCu[Fe^{3+}(CN)_6]_{1-2x}[Fe^{2+}(CN)_6]_{2x} \quad (28)$$

$$xZn \underset{red/ch}{\overset{ox/dis}{\rightleftharpoons}} xZn^{2+} + 2xe^- \quad (29)$$

with $0 \leq x \leq 0.5$

The cell voltage resulting from the potential difference of the cathode and anode are given by equation 4.

$$\Delta E = E_{cathode} - E_{anode} \quad (30)$$

The Gibbs free energy ΔG is related to the equilibrium cell potential (ΔE_{eq}) through equation (31).

$$\Delta G = -nF\Delta E_{eq} \quad (31)$$

The standard Gibbs free energy G^0 is related to the standard cell potential ΔE^0_{eq} through equation (32)

$$\Delta G^0 = -nF\Delta E^0_{eq} \quad (32)$$

The equilibrium cell potential is related to the activity of the species involved in the redox processe through the Nernst equation (7):

$$\Delta E_{eq} = \Delta E^0 + \frac{RT}{z_e F} \ln\left(\frac{a_{ox}}{a_{red}}\right) \quad (33)$$

Where *R* is the gas constant, *T* the temperature in *K*, *F* the Faraday constant and z_e the number of electrons, a_{ox} and a_{red} are the activity of the oxidised and reduced species under equilibium conditions.

For the Zn-ion batteries, the Nernst equation becomes [35, 56]:

$$\Delta E_{eq} = \Delta E^0 + \frac{RT}{z_e F} \ln\left(\frac{a_{KCuFe^{3+}(CN)_6}}{a_{Zn_{0.5}KCuFe^{2+}(CN)_6}}\right) \quad (34)$$

3.16. Kinetic analysis

The kinetics of an electrochemical reaction can be evaluated by the Butler-Volmer equation (12):

$$i = i_o \left[\exp\left(\frac{(1-\alpha)F}{RT}\eta_{ct}\right) - \exp\left(-\frac{\alpha F}{RT}\eta_{ct}\right)\right] \quad (35)$$

where i_o is the exchange current density, α is the transfer coefficient and η is the overvoltage[27, 35]. The latter parameter is related to the cell voltage e and equilibrium cell voltage through equation (9). [56]

$$\eta = \Delta E - \Delta E_{eq} \quad (36)$$

The overpotential is caused by different (electro-)chemical processes such as ion or electron transfer at the interface, or mass transport between electrolyte and the surface of the electrode. The overpotential can be described as the sum of different overpotentials, as the equation 10 shows:

$$\eta = \eta_o + \eta_{ct} + \eta_{mt} + \dots \quad (37)$$

where η_o is the ohmic overpotential, η_{ct} is the charge transfer overpotential and η_{mt} is the mass transfer overpotential. Other overpotentials are the nucleation overpotential.[35, 27]

The ohmic overpotential (η_o) is the resistance that electrodes, separator and electrolyte oppose during the electrochemical process and it can be obtained from equation (11):

$$\eta_o = iR_{int} \quad (38)$$

where i is the applied current and R_{int} is the internal ohmic resistance.[35]

The mass transfer overpotential is correlated to the concentration gradients of the reagents between the surface and the bulk. The are three types of mass transfer: diffusion, migration and convection. An important factor for the mass transfer overpotential is the *molar conductivity (Λm)* of the solution and it's represented by the number of the ions in the solution. It can be expressed with equation (12), where v_+ and v_- are the number of moles of cations and anions while λ_+ and λ_- are the molar ionic conductivities of the cation and the anion.[35, 57]

$$\Lambda_m = v_+\lambda_+ + v_-\lambda_- \quad (39)$$

Another important technique that can be used to analyze the kinetics of a cell is the galvanostatic cycling. In this technique the charge and discharge current are often expressed as a C-rate, calculated from the battery capacity. The C-rate is a measure

of the rate at which a battery is charged or discharged relatively to its maximum capacity. For example, a C-rate of 1 C means that the battery is completely charged or discharged in one hour by applying the necessary current. C-rates multiples of 1 C are also used.

4. EXPERIMENTAL SECTION

4.1. Synthesis

The synthesis consists in preparing two solutions, 120 ml of 100 mM $Cu(NO_3)_2$ and 120 ml of 50 mM $K_3Fe(CN)_6$. These solutions are added dropwise with a flow rate of 1 ml per minute into a 3-neck round-bottomed flask containing 60 ml of deionized water under constant stirring at 400 rpm. The flow rate is precisely controlled by using a peristaltic pump. After finishing, the precipitant is further stirred for 30 more minutes and afterwards ultra-sonicated for 30 minutes. The solution is now set to rest over-night to let CuHCF precipitate. Afterwards, the precipitate is separated from water and divided in equally filled 50 ml falcon tubes for the washing. The washing step is carried out by a centrifuge and is conducted six times for 20 minutes at 6000 rpm to get more stable material by removing impurities from the CuHCF crystal lattice. First, only the precipitate is centrifuged and the tubes are filled between 30 and 35 ml. For the next two times the precipitate is mixed with the wash solution containing 1 M KNO_3 and 10 mM HNO_3 and the tubes are filled up to 35 ml. The last three runs are conducted with deionized water and the tubes are filled up to 50 ml. After the washing, the CuHCF is dried in the oven at 60°C overnight. The resultant material is finally grinded with mortar and pestle to get a homogeneous green-brown powder. The second synthesis follows all the steps of the previous one with the exception of adding 300 mM KNO_3 to the 120 ml 100mM $Cu(NO_3)_2$ solution. The third synthesis is carried out with 600 mM KNO_3 added to the 120 ml 100mM $Cu(NO_3)_2$ solution. For the last synthesis, a ball miller machine is used to obtain the powder of the material. These last experiments were conducted to understand if the presence of a greater quantity of potassium ions could favor a longer life of the electrode.

4.2. Centrifuge time

During the washing procedure the centrifuge time is investigated. In particular, two experiments are conducted with two different centrifugation times: 10 and 20 minutes. These experiments are carried out to understand if a longer centrifugation time would lead to a better washing of the material and therefore to an increase in the electrode performance.

4.3. Three electrode setup

The measurements are conducted by using three electrode flooded cells, where CuHCF is the working electrode, metallic zinc the counter electrode and as reference electrode metallic zinc or Ag/AgCl electrode are used. The working electrode (WE) contains CuHCF as active material. Therefore, a 3 x 1 cm stripe of carbon cloth is painted partially with the active material. In detail, a slurry consisting of 80 wt% CuHCF, 9 wt% amorphous carbon (C65), 9 wt% pol-yvinylidene fluoride (PVDF) binder solution in N-methyl-2-pyrrolidone (NMP, 25 mg/ml) and 2 wt% graphite (SFG6) is stirred by using an ultra-turrax disperser for 30 minutes at 4000 rpm. Due to heat production, 10 minutes of stirring are followed by 10 minutes of resting. After stirring, the slurry is hand-painted on the carbon cloth current collector (approx. 1 cm^2) and afterwards dried in the oven at 60 °C overnight. Finally, a small stripe of wax dissolved in toluene and painted on the upper part of the carbon cloth to prevent capillary effects and again, the electrode is dried at 60 °C overnight. Five electrodes are prepared at the same time. The electrochemical measurements are conducted in a three-electrode flooded cell. Electrochemical reactions and current flow only occur between working and counter electrode. For measuring the potential of the working electrode precisely, the potential is read between working and reference electrode. By using a reference electrode, it was possible to separate the contribution of the zinc electrode from that of CuHCF[8]. In particular, it was possible to study the effect of zinc ion intercalation on the potential profile of Copper Hexacyanoferrate[8]. In an electrochemical cell the cell voltage is equal to the

difference between the positive electrode´s potential and the negative electrode´s potential. For the used three-electrode cell the total voltage is measured between CuHCF (WE) and Zn (RE) or Ag/AgCl (RE). The current is flowing and measured between CuHCF (WE) and metallic zinc (CE). The cells are filled up until the active material on the carbon cloth is entirely immersed in the electrolyte.

4.4. Electrolytes

In these experiments the role of the electrolyte is investigated using two different solutions. The main electrolyte is zinc sulfate and the principal solution is a slightly acidic aqueous solution of 100 mM $ZnSO_4$. The second solution contains potassium chloride as electrolyte in addition to the 100 mM $ZnSO_4$. Two different concentrations of KCl are investigated, 100 mM KCl and 50 mM KCl. The choice of potassium chloride as the second electrolyte was driven by the longer life cycle of the electrodes used with the silver/silver chloride as reference electrode with the solution of 100 mM $ZnSO_4$. The Ag/AgCl electrode is composed of a 3 M KCl solution that might be leaking during the measurements. Hence, the choice of introducing potassium chloride directly into the solution to simulate the leaking of the electrode. The working electrodes immersed in the solution of KCl added to the first electrolyte are utilized with a zinc foil as a reference electrode.

4.5. Pre-immersion of the WE in the electrolyte

In the differential specific charge profiles the intensities of the second redox peak, attributed to the formation of new phases, changed weakly in response to the number of cycles[9]. This means that the electrochemical performances alone could not prove the phase formation[9]. It has been previously suggested that such phase transition may involve a partial substitution of Cu^{2+} with Zn^{2+} in the B sites of the CuHCF crystal, with the consequent formation of a distorted CuZnHCF phase[14,15].

For these reasons, it has been hypothesized that the phase transformation process might also occur in the absence of the electrochemical one for direct reaction between the material and the electrolyte. Without the electrochemical performance (e.g. cycling), the material may go under a slower phase transformation that might allow the system to form a more stable phase and therefore extend the life of the electrode. For this purpose, the electrodes are immersed in the electrolyte (100 mM $ZnSO_4$) for two weeks and subsequently cycled. Before the immersion, the electrodes are cycled for three times. The measures are stopped at the end of the reduction. There, the zinc ions intercalated into the crystal structure remain inside the material allowing the reaction to happen.

5. RESULTS AND DISCUSSION

5.1. General Considerations

During the first part of this thesis work, the substrates used as support for the active material were constituted by classical glassy graphite disc electrodes (GCE). This type of material was used in order to be able to perform measurements by scanning electrochemical microscopy (SECM), as well as voltammetric and galvanostatic measurements. The support material used during the second part of the thesis was made of graphite mesh. This type of substrate is characterized by high porosity and is the one used in real batteries. However, the high roughness does not allow measurements to be made with a high spatial resolution technique such as the SECM.

5.2. Voltammetric behaviour of the CuCHF system

For the characterization of the CuHCF, potentiodynamic measurements have been conducted. The higher potential limit was 1.2 V vs Pt, while the lower limit was 0.2 V. This potential interval is the onset at which the electrode process of the $[Fe^{III}(CN)_6]^{3-}$ /$[Fe^{II}(CN)_6]^{2-}$ system occurs. The first scans was carried out starting from the open circuit potential (OCP) in an aqueous solution of 20 mM of $ZnSO_4$. In these experiments, the variation of the potential (E) over time (t) was measured until constant values were obtained. Figure 5.1 shows responses obtained with electrodes with 20 μl of CuHCF. Before any measurements, the cell was de-aerated with a flow of nitrogen for 5 minutes.

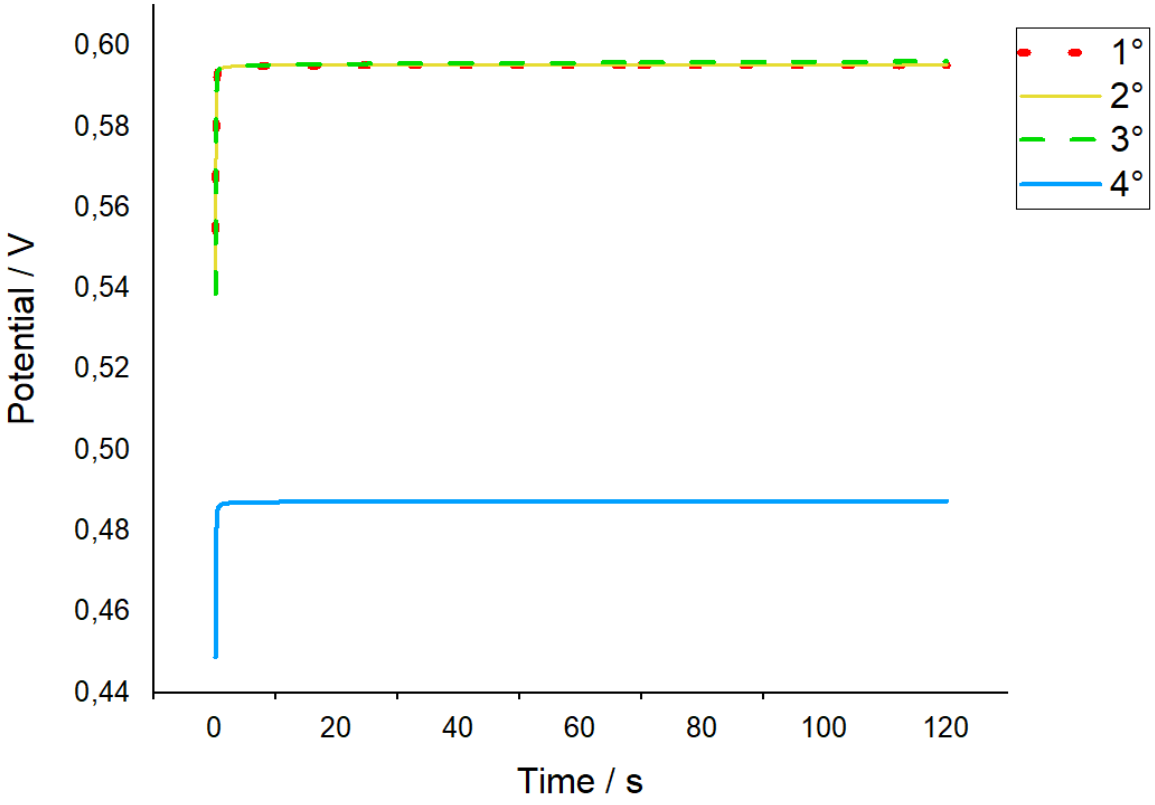

Figure 5.1: open circuit potentials of different electrodes from the same batch.

It can be seen that, in all cases, the potential starts from a lower value than the actual OCP. The first three electrodes show almost the same values of starting potential and open circuit potential while the fourth electrode shows values 0.09 V lower in both potentials as can be seen in Table 5.1.

Table 5.1: initial and open circuit potential values of the electrodes with 20 µl of CuHCF.

	1°	2°	3°	4°
Initial potential (V)	0.554	0.542	0.539	0.449
OCP (V)	0.595	0.595	0.596	0.487

The lower value of the 4th measure might be due to an error during the deareation process before the measurement. In every case, a constant value was obtained

after less than 3 seconds. The open circuit potential values were determined at t = 120 s.

Starting from the OCP value, voltammetric cycles were then performed at scanning speeds ranging between 0.05 mV s^{-1} and 0.5 mV s^{-1} until stationary voltammograms were obtained. The number of cycles required to reach this last condition depended, to some extent, on the thickness of the CuHCF film (e.g. the amount of material deposited), on the uniformity of the deposit produced on the disc electrode and on the size of the disc itself. With the electrodes and the quantities of material used, a stationary condition was reached after a number of 4 cycles. A typical cyclic voltammogram recorded after 4 cycles is shown in Figure 5.2 while the voltammogram in the box shows the first cycle obtained starting from the OCP. The general form of the voltammogram is that expected for processes involving solid phase redox reactions associated with intercalation of ions present in solution.[68] The charging and discharging process of the CuHCF structure correspond to the cathode and anodic branch, respectively, of the voltammogram shown in Figure 5.2.

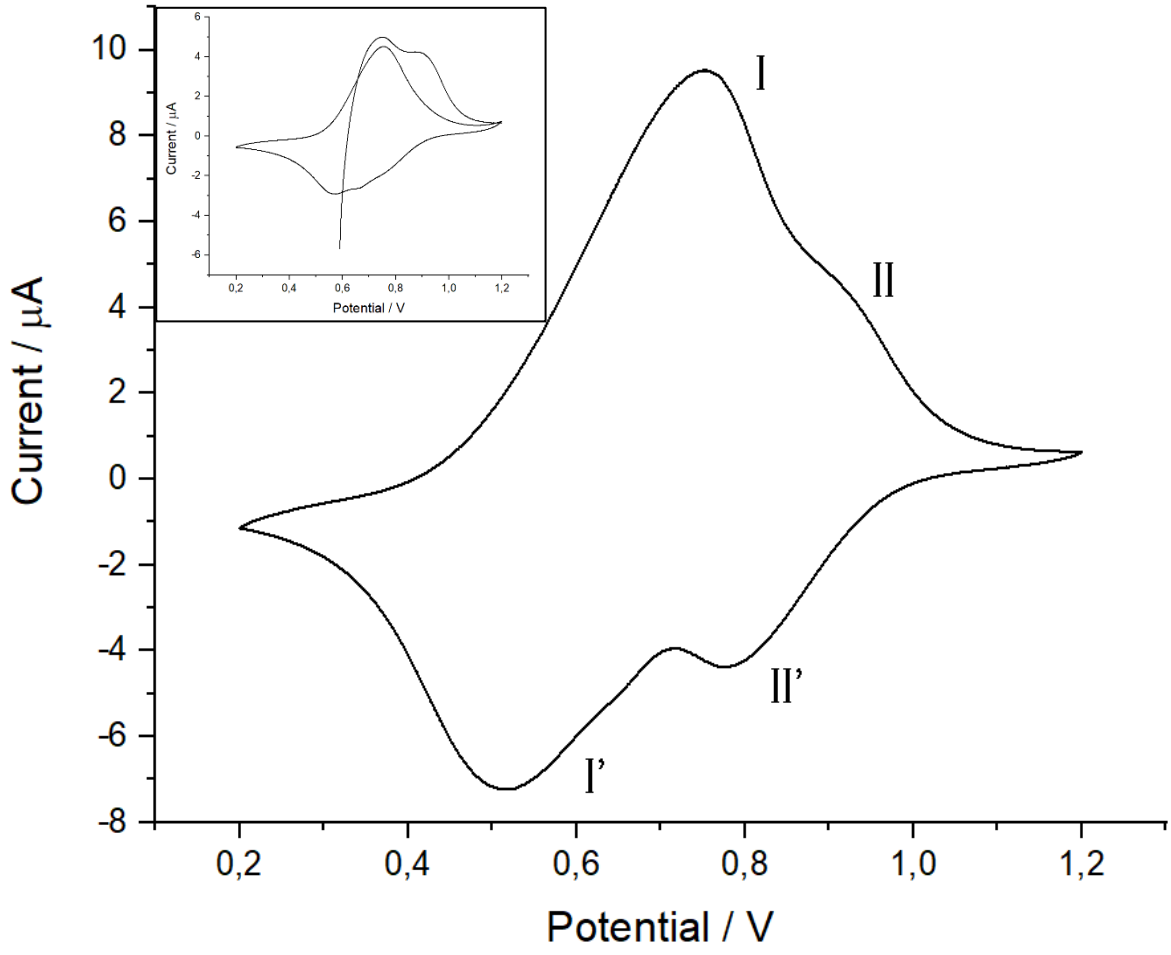

Figure 5.2: 1st cycle (in the box) and 4th cycle of the voltametric measure of CuHCF

The voltammogram shows two pairs of peaks both in the anodic (I', II') and in the cathodic (I, II) scanning. The peaks (I-I') are attributed to the redox system $[Fe(CN_6]^{3-}$ / $[Fe(CN)_6]^{2-}$, while the peaks (II-II') are assigned to the (de-)intercalation of Zn^{2+} in the CuHCF crystal structure. The overall electrode process, considering the nominal formula $KCuFe^{III}(CN)_6$ [2.1], is as follows:

$$KCuFe^{III}(CN)_6 + xZn^{2+} + 2x\ e- \leftrightarrow ZnxKCu[Fe^{III}(CN)_6]_{1-2x}[Fe^{II}(CN)_6]_2 \quad (1.1)$$

The intercalation process in the crystal structure of CuHCF entails that two low spin Fe^{III} atoms are simultaneously converted into two low spin Fe^{II} atoms.[53] Figure 5.3 schematically shows the reversible process of (de)intercalation of Zn^{2+} ions.

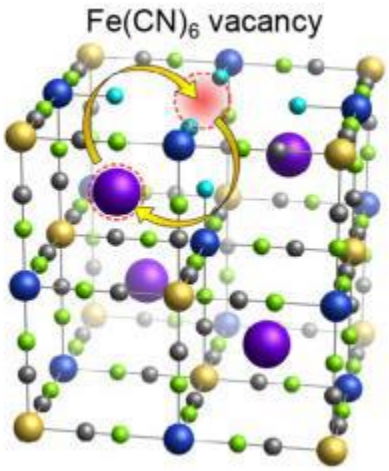

Figure 5.3: Scheme of the Zn^{2+} (de)intercalation process in the crystal structure of CuHFC [60]

The voltammetric response described above is valid for electrolytic solutions containing Zn^{2+} ions. Electrolytes having different cations can give different responses, depending on the charge and size of the solvated ions.[61]

An important aspect to establish the characteristics of a voltammetric response is the scanning speed. For scan rates up to 1 mV s^{-1}, voltammograms similar to those shown in Figure 5.3 were obtained. For higher scan rates, voltammograms became much more down-lying, e.g. irreproducible.[45] This causes a widening between the anodic and cathodic peak potential (ΔE_p) of the system $[Fe(CN)_6]^{3-}$ / $[Fe(CN)_6]^{2-}$, while the process correlated to the (de-)intercalation of the zinc ions was completely absent or covered by the background current.[45] This different voltammetric shape is due to the ohmic drops, e.g. the resistance that the system imposes at the current flow and it's linked to the solution resistance. The cyclic voltammograms recorded in stationary conditions were used to establish the mass actually present on the electrode surface. This evaluation was based on the charge (q) associated with the oxidation or reduction process and using equation 18. The charge was obtained by

integration of the voltammograms. Table 5.2 shows the charge values, relative mass (m) and anodic peak current (μA).

Table 5.2: charge, mass and peak current value of CuHCF deposited on a GCE electrode.

***v* scan (mV s^{-1})**	**q (mC)**	**m (mg)**	**i (μA)**
1.00	43.9	0.14	14.50
0.50	53.3	0.17	9.51
0.30	50.5	0.16	6.64
0.20	57.9	0.19	4.90
0.10	61.8	0.20	2.93
0.05	67.2	0.22	1.74

As expected, the peak current decreases at the lowering of the scan rate. The values of the mass vary from 0.14 mg to 0.22 mg with an average value of 0.18 mg. The higher mass value is shown with the lowest scan rate, while the lower mass value is obtained with the higher scan rate. The fact that the lower scan rate has the higher mass value might be due to the higher amount of time that the system had to undergo the electrode process. In addition, the higher mass value shows, as expected, the higher amount of charge.

5.3. SECM and Voltammetric study of the CuHCF film

The analyzes were carried out in an electrochemical cell in the two-electrode configuration, using a platinum disk microelectrode (12.5 μm radius) both as a working electrode (in voltammetric measurements) and as a SECM probe; a platinum wire served as a pseudo-reference/counter electrode. The measurements were conducted in an aerated aqueous solution containing 100 mM of $ZnSO_4$. The SECM measurements on CuHCF films were conducted using [FcTMA] [PF_6] as a

redox mediator. This compound was chosen because it is sufficiently soluble in aqueous solutions, unlike other similar redox systems of ferrocene. Furthermore, the positive charge of $[FcTMA]^+$ is balanced by the anion $[PF_6]^-$ which, unlike ions such as Cl^-, does not form complexes with any Cu^{2+}/Cu^+ ions which can be released into the solution from the CuHCF structure. The measurements were carried out in a Teflon cell with 1 ml of an aqueous solution containing 20 mM $ZnSO_4$ as support electrolyte. As a SECM probe, a platinum microelectrode was used. The electrode supporting the active material was inserted from the bottom of the Teflon cell. As long as the microelectrodes built for the SECM measures are very fragile, the approach was interrupted whenever the conductivity started to increase, meaning that the electrode was near the surface. To avoid breaking, the next measurements were conducted by dropping the electrode manually by 5 μm at a time and then a voltametric measurement was performed.

The $FcTMA^+$ gives rise to the following reversible monoelectronic process:

$$FcTMA^+ \rightleftarrows FcTMA^{2+} + e^-$$

The approach curves were constructed to determine the RG parameter of the microelectrodes subsequently used for SECM measurements. The substrate considered was the 1.5 mm radius GCE. The approach curves were recorded by imposing a potential of 0.4 V vs. the microelectrode of Pt, at which the redox process is controlled only by diffusion. No external potential was applied to the substrate.

The positive feedback curves were obtained on the active part of the electrode. Positive feedback approach curves are shown in Figure 4.5.

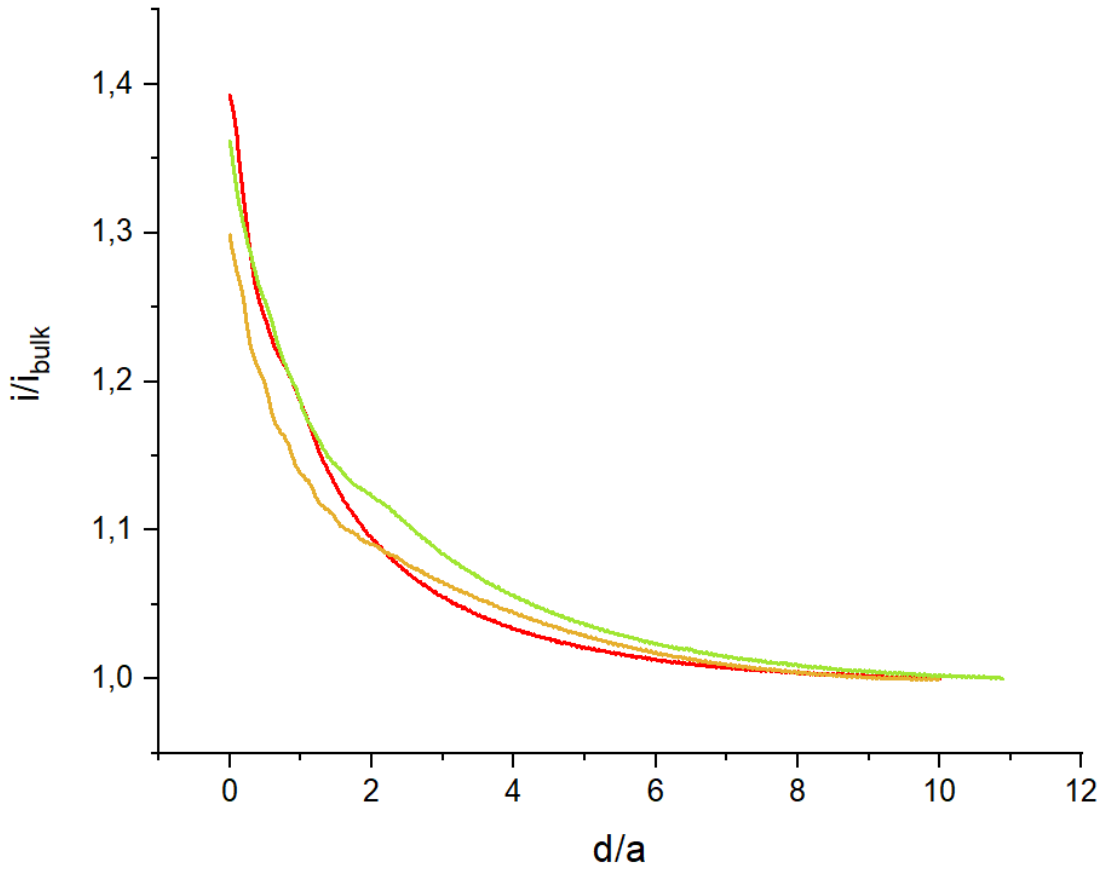

Figure 5.4: positive feedback curves

If the substrate is conductive, a potential can be applied such that the opposite reaction occurs to the substrate to that which occurs on the surface of the micro-electrode. The current increases as the distance between the microelectrode and the substrate decreases. The increase in current is due to the shorter distances that the oxidized species must cross to reach the surface on which it regenerates. In these conditions, regeneration is much faster and consequently the current increases. At the limit, if the microelectrode touches the substrate, the current goes to infinity as a consequence of a short circuit. In this case, a signal that goes out of range is obtained. The regeneration phenomenon can occur even if a potential is

not applied to the conducting substrate. There are conditions, especially when the electrode surface is very high, in which regeneration occurs spontaneously.

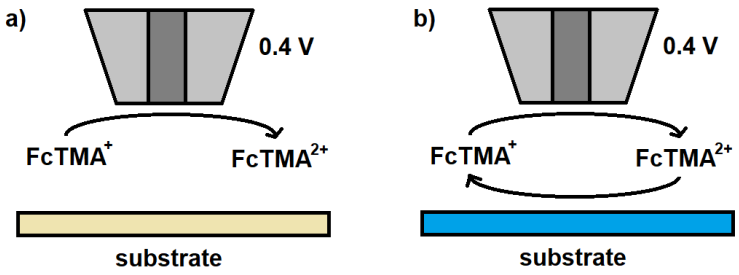

Figure 5.5: Electrodic processes between a microelectrode and an insulating substrate (a) and conductive substrate (b).

The negative feedback curves were obtained on the part of the insulator (Teflon) surrounding the glassy carbon disc (Figure 5.6).

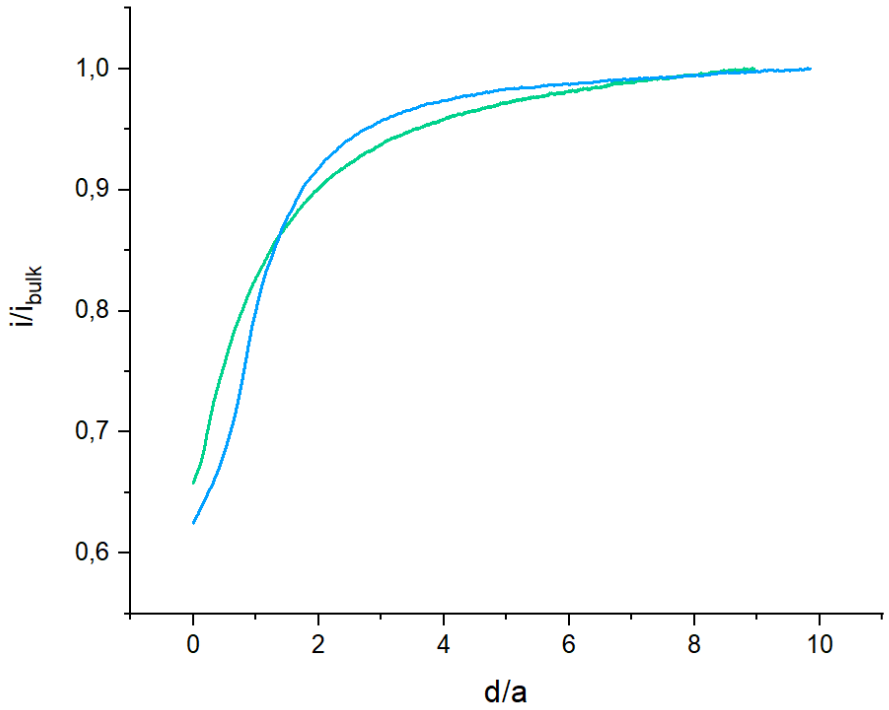

Figure 5.6: approach curve recorded on the insulating (Teflon) surface.

The current decreases compared to that observed in the bulk. As you get closer, the substrate is insulating and acts by preventing the transport of matter towards the electrode. Away from the substrate, diffusion occurs in all directions. When the microelectrode is close to the substrate (Figure 4.6 a), as it is insulating, this prevents the substance from reaching the substrate itself. There is an impediment to dissemination. If there is an impediment to diffusion, the flux at the electrode surface decreases and consequently the current also decreases. The decrease in current depends on the microelectrode-substrate distance. The smaller the distance between the microelectrode and the substrate, the greater the decrease in current. At the limit, if the microelectrode is supported, the current goes to zero because no material arrives.

The positive outcome is linked to the effect of lateral charge transfer, as shown in Figure 5.7.

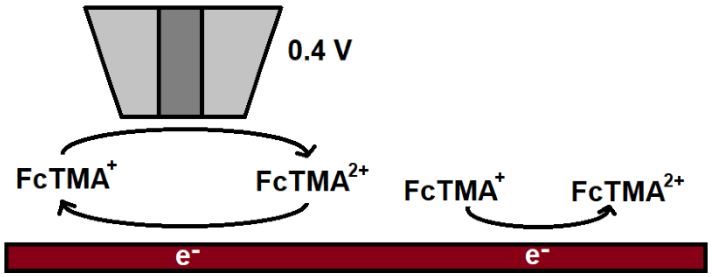

Figure 5.7: schematization of the lateral charge transfer effect.

The surface of the substrate, being conductive, assumes a potential value which in the $FcTMA^+$ solution is less positive than that generated in the gap below the microelectrode. A concentration cell is thus created, responsible for the redox mediator recycling phenomenon even in the absence of a potential applied to the substrate.[11.1]

Before proceeding with the SECM study, the GCE electrode covered with the CuHCF film was examined in an electrochemical cell in the three-electrode configuration. This experience was conducted at verifying that the deposited material provided a voltammetric picture similar to those recorded on CuHCF

deposits prepared on the larger GCEs. No external potential was applied to the substrate. The electrode placed in the SECM cell was then studied in feedback mode, using $FcTMA^+$ as a redox mediator.

To establish the position of the microelectrode near the substrate, approach curves were preliminarily recorded on the part of the Teflon insulation that surrounded the CuHCF-coated substrate. Subsequently, it was positioned over the active area of the material. In both cases, a potential of 0.4 V vs. Pt.

5.4. Linear and 3D scan

In order to establish the degree of homogeneity of the CuHCF film, from the point of view of the active centers, linear scans and 3D were performed to cover areas larger than those that could be evaluated by means of an approach curve. For this purpose, the microelectrode was placed 15 - 25 µm above the substrate, where the positive feedback effect is sufficiently high. Linear scans were performed in multiple X-Y directions parallel to the plane on which the SECM cell rested, covering distances up to 1000 µm. Furthermore, for each curve performed in a given direction, the corresponding one in the opposite direction was recorded, so as to verify that the observed signals were not artifacts due to uncontrolled phenomena (background noise, spikes of currents linked to variations in mains voltage, inadvertent movements of the bench on which the instrumentation was placed by the operator, etc).

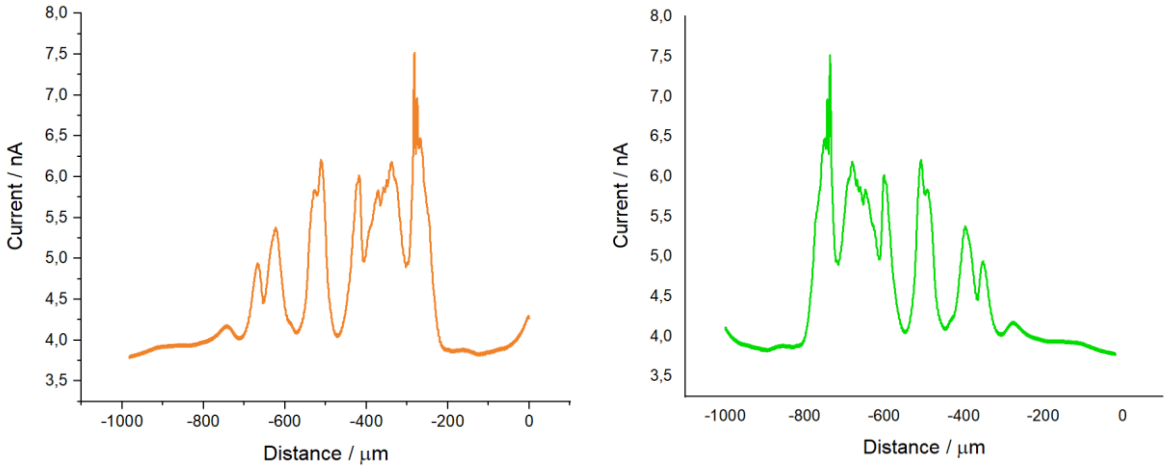

Figure 5.8: linear scans on the same points of the CuHCF deposit.

The reliability of the responses obtained was established by performing two series of measurements in the same direction and in the opposite direction (Figure 5.8). In order to have significant responses, the position of the microelectrode, with respect to the substrate studied, must be chosen carefully in order to avoid incorrect readings of the results due to tilting phenomena (lack of perpendicular alignment of the microelectrode with respect to the substrate). The series of voltammograms are superimposable (Figure 5.8). The scan rates show an irregular surface of different degree in some point of the material. In certain cases, the variation of the thickness of the deposited material caused the interruption of the measure in order to avoid the braking of the micro electrode. In these cases, the current responses, in some points, are widely outside the limit of the plausible full scale selected.

Using the same criteria defined above, 3D surface maps can be recorded, where the most active and least active areas present in the CuHCF film can be distinguished. An example is shown in Figure 5.9.

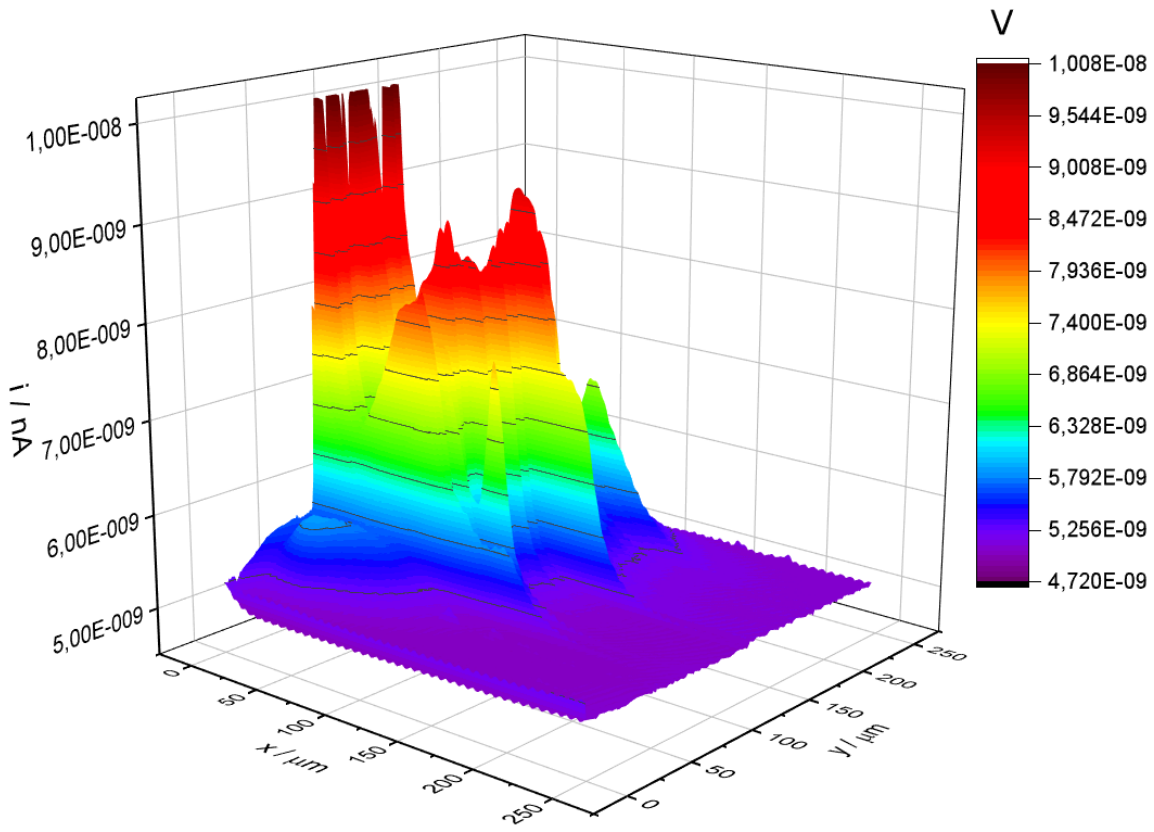

Figure 5.9: Map of the surface of the CuHCF deposit.

The topography of the substrate being investigated was studied because the increase or decrease of the current could be due to an activity of the substrate itself. The map obtained from CuHCF sample, in agreement with the linear scan measures (Figure 5.8), shows an irregular conductivity around the surface investigated (Figure 5.9).

In this first part of this thesis, a basic study of the electrochemical behavior of the active material was carried out by voltammetric and scanning electrochemical microscopy measurements. In the second part of the thesis, a deeper study was performed by carrying out different experiments in order to achieve a better understanding of what might cause the aging of the system.

5.5. Galvanostatic measurements

This section presents the results of the electrochemical measurements for the different synthesis. For testing these electrochemical systems, galvanostatic cycling with potential limitation (GCPL) is used as electrochemical technique. During this method a current is imposed on the system with given potential ranges, while the actual potential is constantly plotted. As instrument for all these electrochemical measurements a VMP3 from BioLogic is used. The applied current is set equal to a current rate of 1 C for CuHCF (85.2 mAh g^{-1}) and the potential limits, referring to CuHCF working electrode, to 1.25 V as lower limit and 2.15 V as upper limit vs. Zn. For the experiments that don't include potassium chloride as electrolyte, measurements with silver/silver chloride electrode as reference are conducted. Thus, the potential limits are set to 0.25 V as lower limit and 1.15 V as upper limit (vs. Ag/AgCl in 3 M KCl).

5.5.1. Standard synthesis : CuHCF 100:100

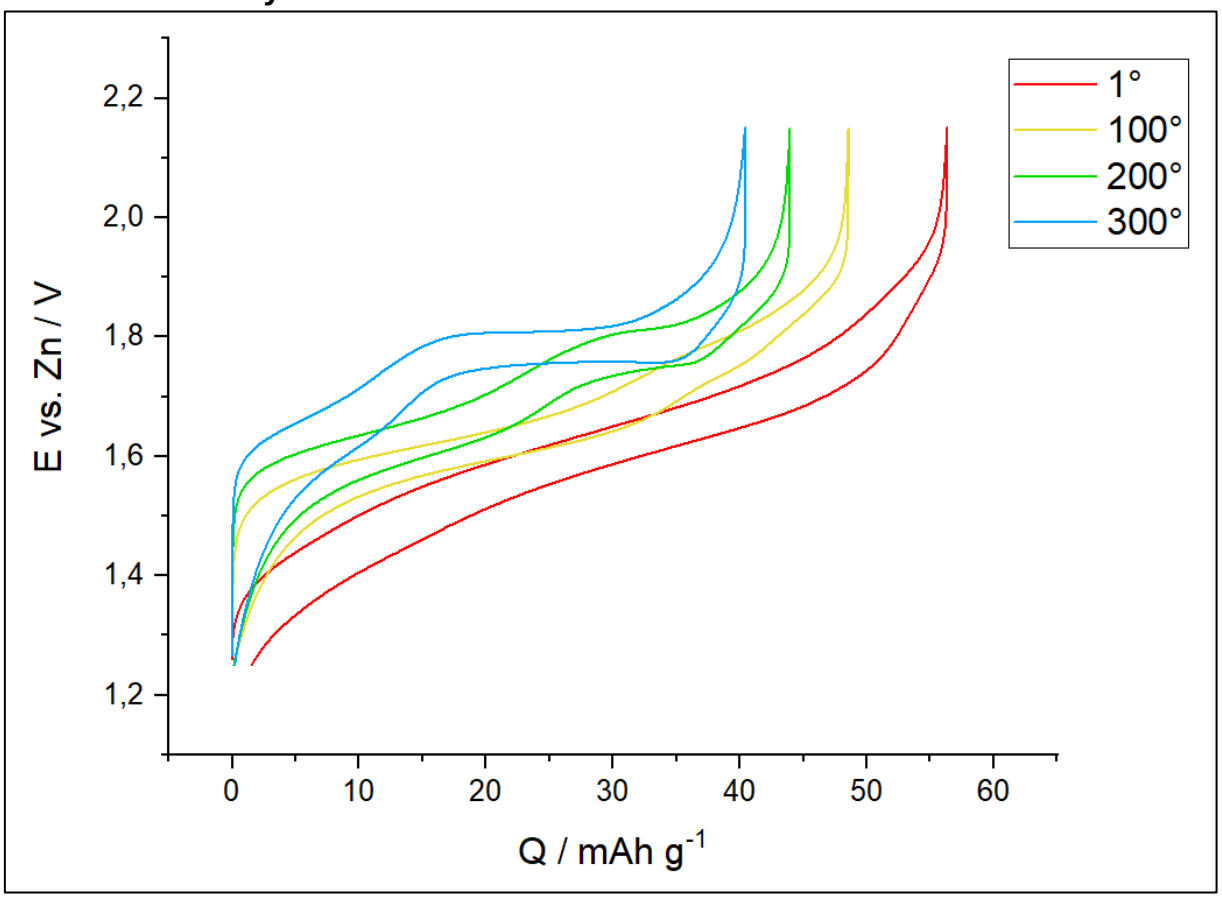

Figure 5.10: Galvanostatic cycle plot (1C rate) of CuHCF 100:100 for 1st, 100th, 200th and 300th cycle.

In figure 1 the 1st, 100th, 200th and 300th galvanostatic cycle plots of CuHCF 100:100 synthesis are shown. The potential is measured vs. Zn. These data are taken from the second measurement of the first batch from the first synthesis of CuHCF 100:100. Starting with an initial specific charge capacity of 55.69 mAh g^{-1}, the specific charge of the working electrode decreases to 41.58 mAh g^{-1} after 272 cycles, which is equal to retention of 80%.

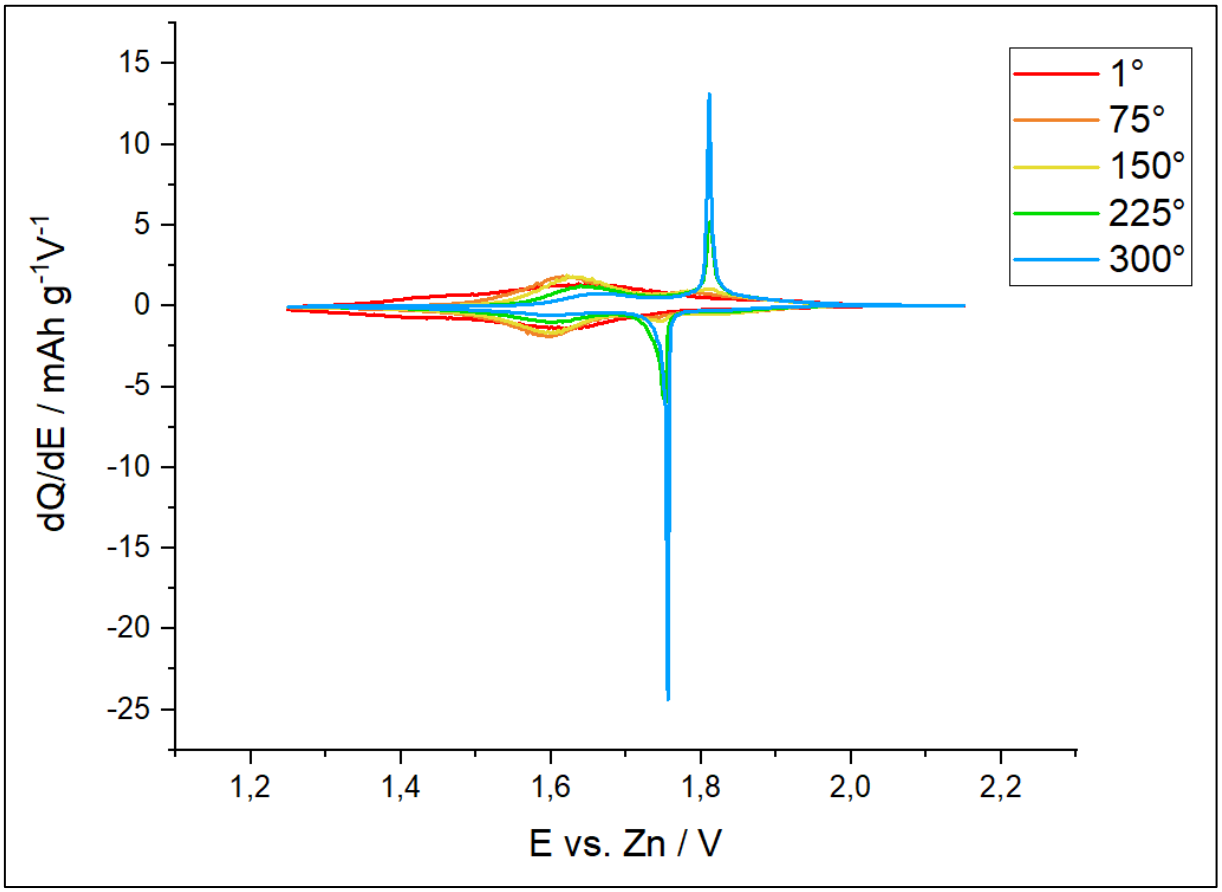

Figure 5.11. Differential charge plot of CuHCF 100:100 for 1st, 100th, 200th and 300th cycle.

Figure 5.11 shows the differential charge of the CuHCF 100:100 at the 1st, 100th, 200th and 300th cycle. The potential is measured vs. Zn. These data are also taken from the second measurement of the first batch from the first synthesis of CuHCF 100:100. For both oxidation and reduction processes two peaks are visible. The second peaks appear at the 28th cycle and start to grow in a spike shape from the 159th cycle while the first peaks start to decrease. The average potential of the second peaks is 1.79 V.

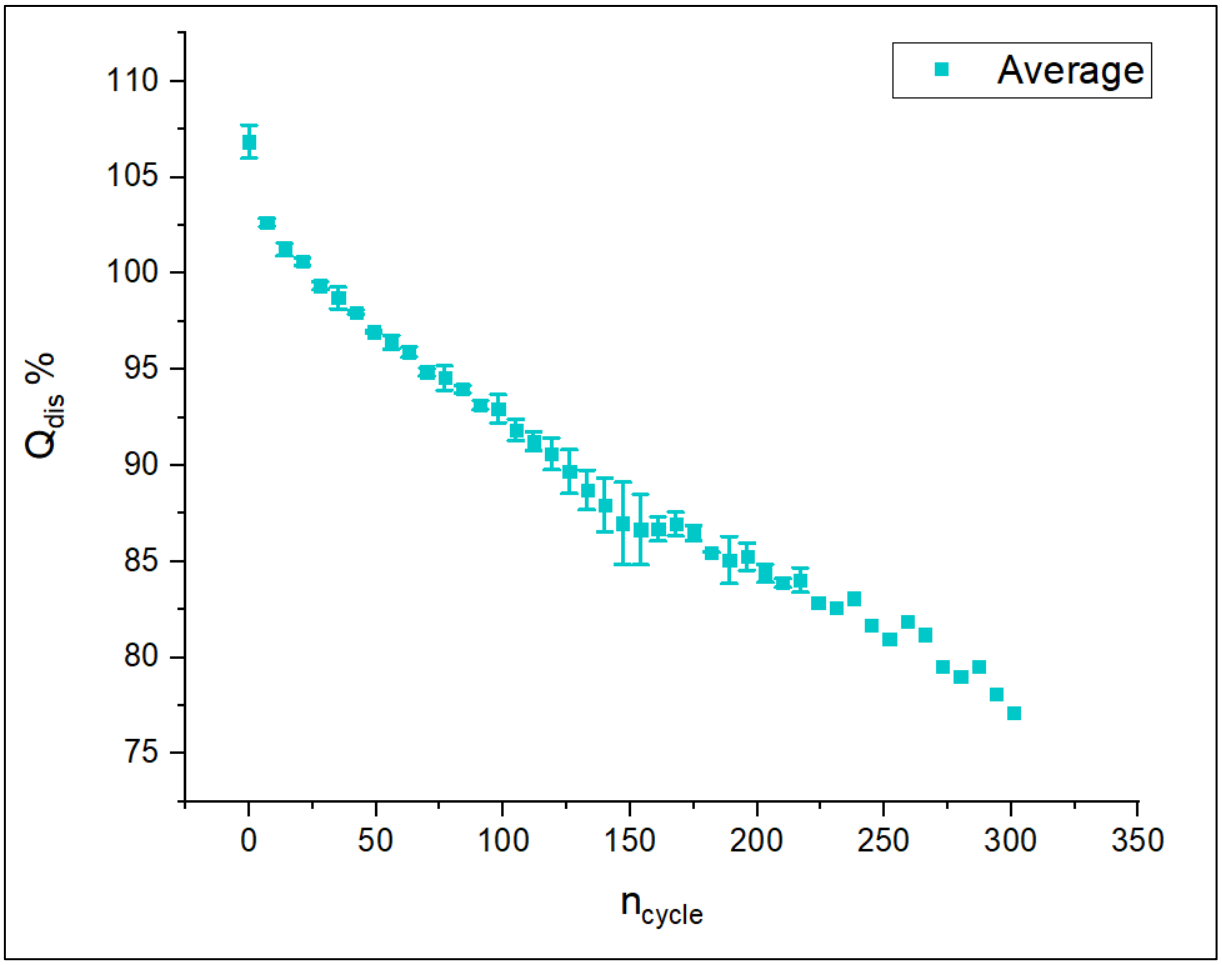

Figure 5.12. Average charge retention of the CuHCF 100:100 electrodes galvanostatically cycled at 1C vs. Zn. The retention has been normalized by the charge at the 25th cycle.

Figure 5.12 shows the mean value of the CuHCF electrode charge retention related to the number of cycles. The values are generated after full reduction of the CuHCF electrode and plotted in percentage referring to the charge reached at the 25th cycle during the measurement. The average and standard deviation have been calculated by comparing four different samples resulting from two different batches of two different synthesis of CuHCF 100:100. The maximum standard deviation is 2.26.

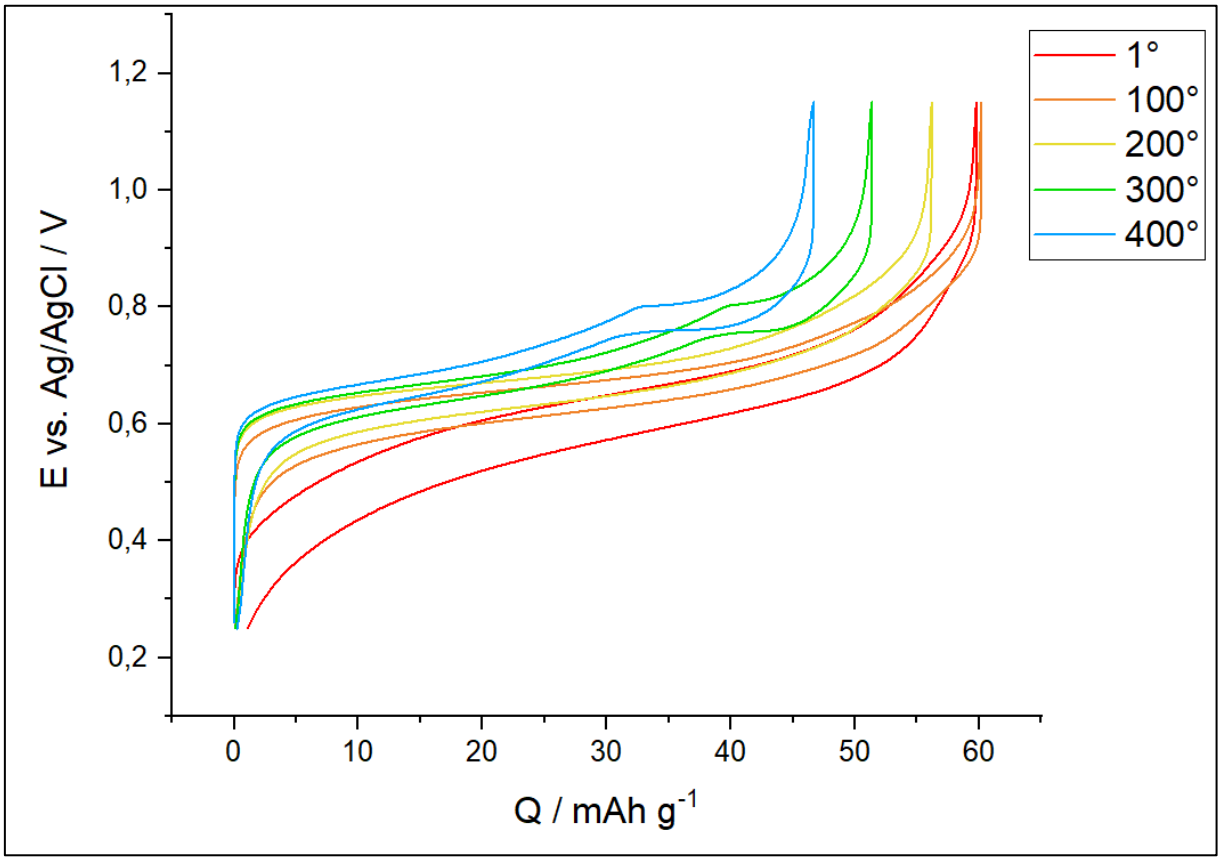

Figure 5.13. Galvanostatic cycle plot (1C rate) of CuHCF 100:100 for 1st, 100th, 200th, 300th and 400th cycle.

In figure 5.13 the 1st, 100th, 200th, 300th and 400th galvanostatic cycle plots of CuHCF 100:100 synthesis are shown. The potential is measured vs. Ag/AgCl in 3 M KCl. These data are taken from the second batch of the first synthesis. Starting with an initial specific charge capacity of 58.65 mAh g^{-1} the capacity retention of the working electrode decreases to 80% after 371 cycles, reaching a specific charge of 48.24 mAh g^{-1}.

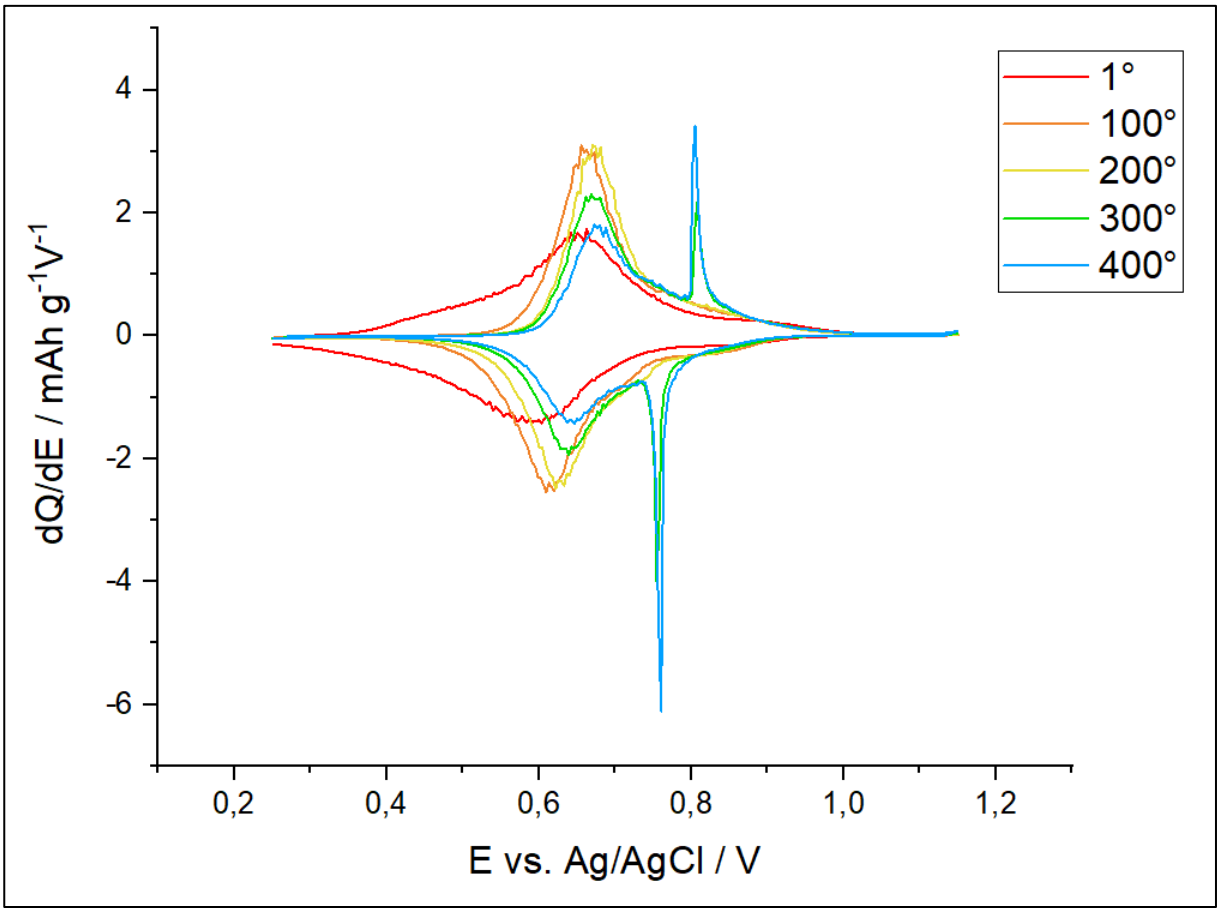

Figure 5.14. Differential charge plot of CuHCF 100:100 for 1st, 100th, 200th, 300th and 400th cycle.

Figure 5.14 shows the differential charge of the CuHCF 100:100 at the 1st, 100th, 200th, 300th and 400th cycle. The potential is measured vs. Ag/AgCl in 3 M KCl. These data are also taken from the second batch of the first synthesis. For both oxidation and reduction processes two peaks are visible. The second peaks appear at the 197th cycle and start to grow in a spike shape from the 215th cycle while the first peaks start to decrease. The average potential of the second peaks is 0.79 V.

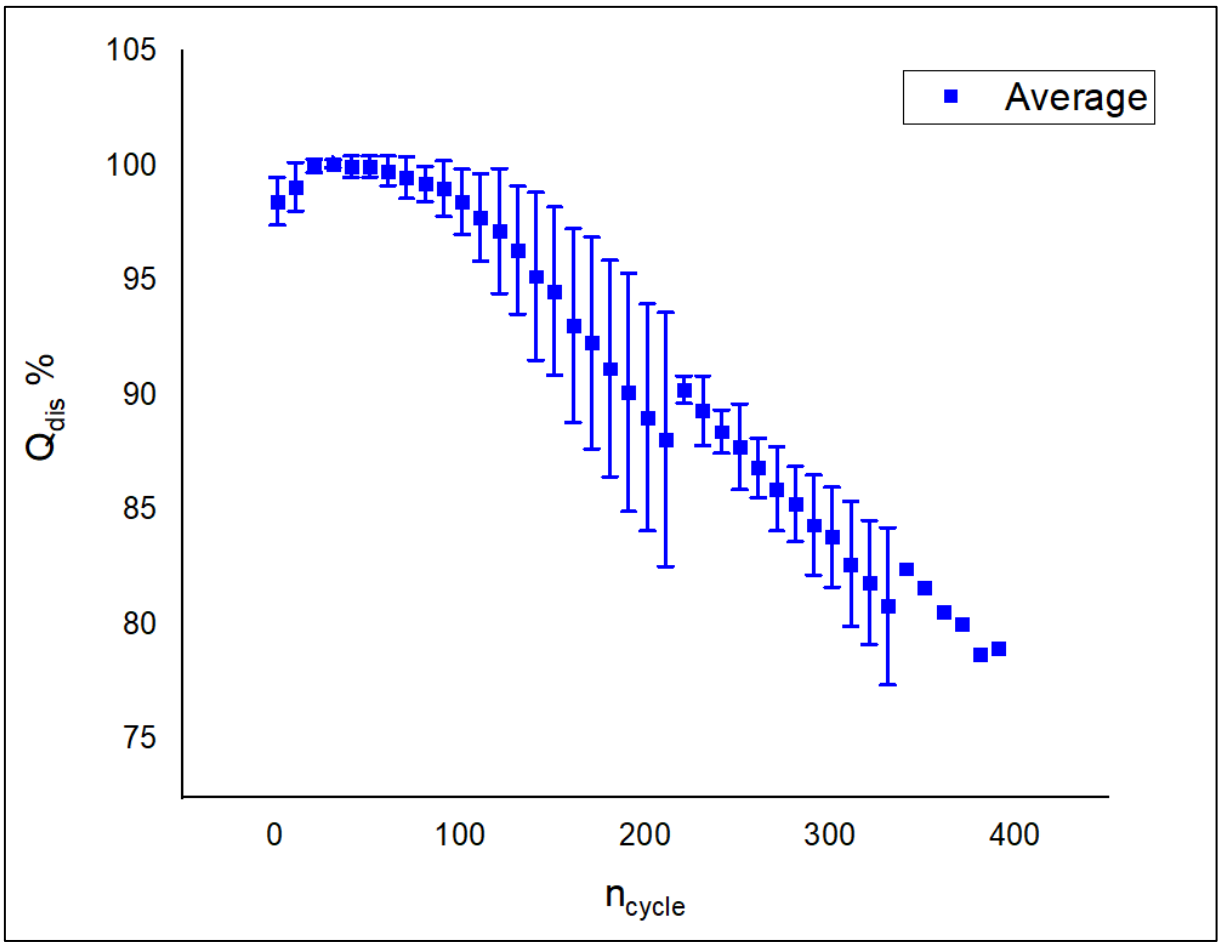

Figure 5.15: Average charge retention of the CuHCF 100:100 electrodes galvanostatically cycled at 1C vs. Ag/AgCl. The retention has been normalized by the charge at the 25th cycle.

Figure 5.15 shows the mean value of the CuHCF electrode charge retention related to the number of cycles. The values are generated after full reduction of the CuHCF electrode and plotted in percentage referring to the charge reached at the 25th cycle during the measurement. The average and standard deviation have been calculated by comparing three different samples resulting from two different batches of two different synthesis of CuHCF 100:100. The first measurement of the first batch achieved a retention of 80% at the 219th cycle. The first measurement of the second batch reached a retention of 80% after the 317th cycle. The second measurement

of the first batch achieved a retention of 80% after 371th cycle. The maximum standard deviation is 5.68.

5.5.2. CuHCF 100 :100 with 100mM KCl added in the solution

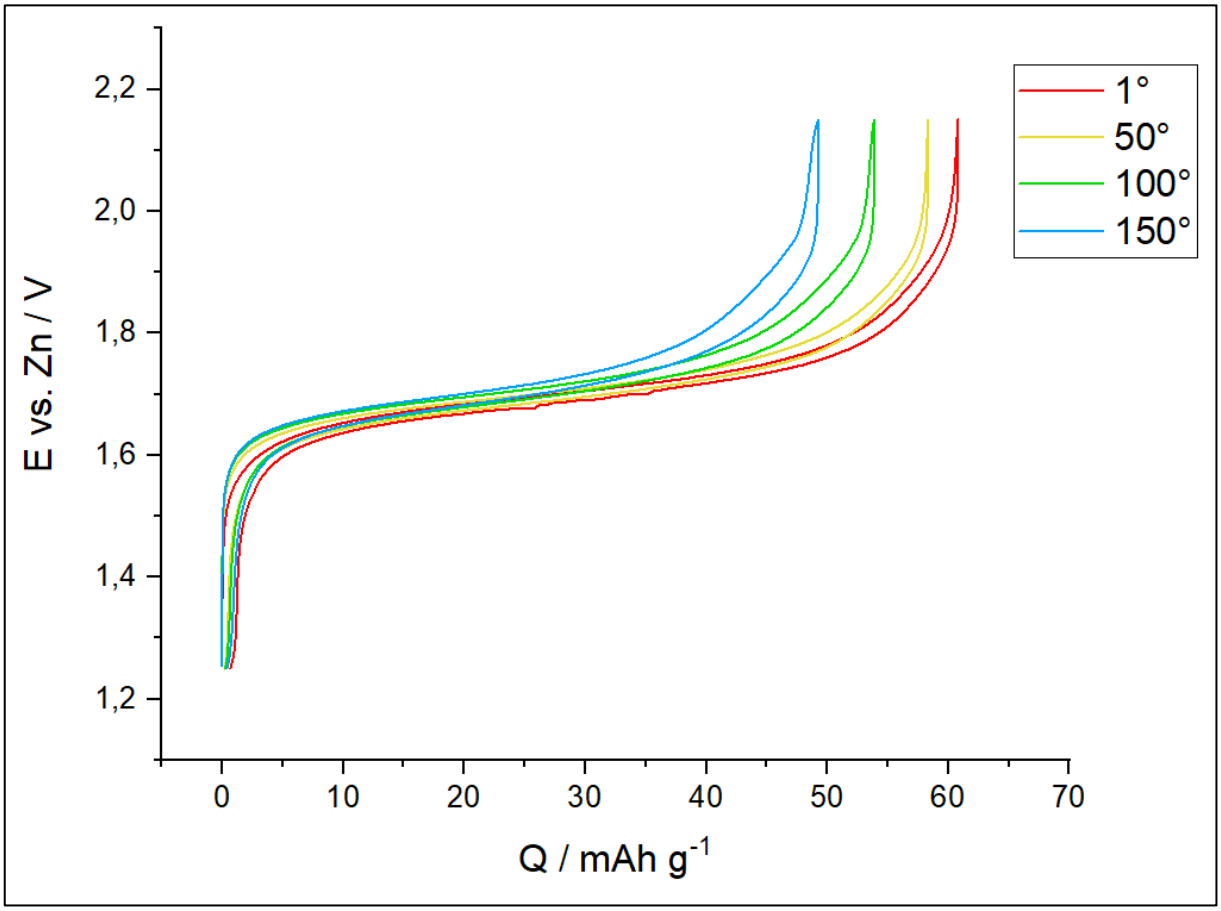

Figure 5.16. Galvanostatic cycle plot (1C rate) of CuHCF 100:100 with a solution of 100 mM $ZnSO_4$ and 100 mM KCl for 1st, 50th, 100th and 150th cycle.

In figure 5.16 the 1st, 50th, 100th and 150th galvanostatic cycle plots of CuHCF 100:100 synthesis are shown. The electrolyte solution is made of 100 mM $ZnSO_4$ plus 100 mM KCl. The potential is measured vs. Zn. These data are taken from the second batch of the secon CuHCF 100:100 synthesis. Starting with an initial specific charge capacity of 60.39 mAh g^{-1}, the specific charge of the working electrode decreases to 47.59 mAh g^{-1} after 160 cycles, which is equal to retention of 80%.

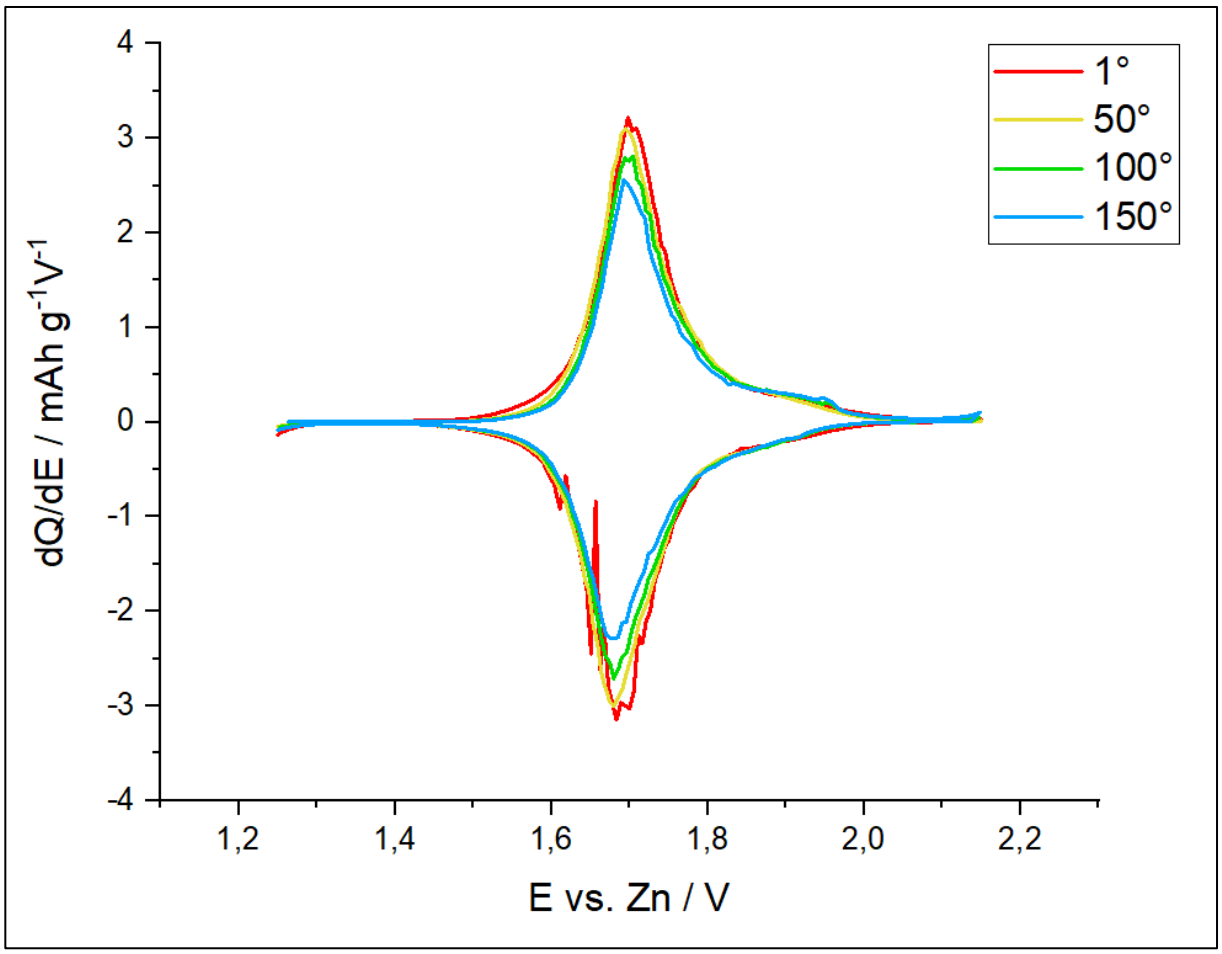

Figure 5.17: Differential charge plot of CuHCF 100:100 with a solution of 100 mM $ZnSO_4$ and 100 mM KCl for 1st, 50th, 100th and 150th cycle.

Figure 5.17 shows the differential charge of the CuHCF 100:100 at the 1st, 50th, 100th and 150th cycle. The potential is measured vs. Zn. These data are taken from the second batch of the second standard synthesis. In this case only the first-phase peaks are visible for both oxidation and reduction processes. The absence of the second phase-peak can also be seen from the galvanostatic cycles plot (Figure 5.16).

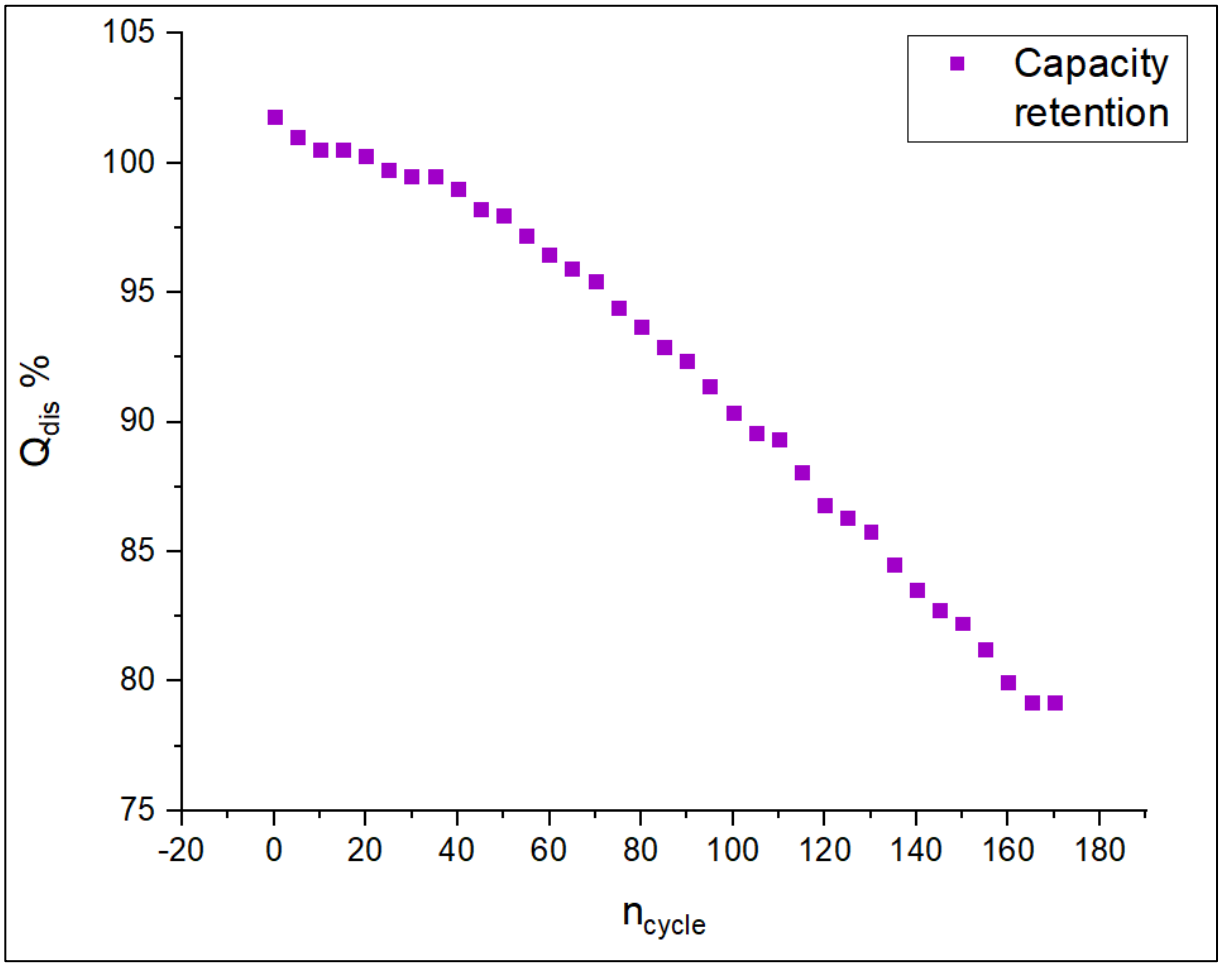

Figure 5.18: Charge retention of CuHCF 100:100 electrodes with a solution of 100 mM $ZnSO_4$ and 100 mM KCl, galvanostatically cycled at 1C vs. Zn. The retention has been normalized by the charge at the 25th cycle.

Figure 5.18 shows the decreasing of the capacity of the CuHCF electrode, with a solution of 100 mM $ZnSO_4$ and 100 mM KCl, related to the number of cycles. The values are generated after full reduction of the CuHCF electrode and plotted in percentage referring to the charge reached at the 25th cycle during the measurement.

5.5.3. CuHCF 100 :100 with 50mM KCl added in the solution

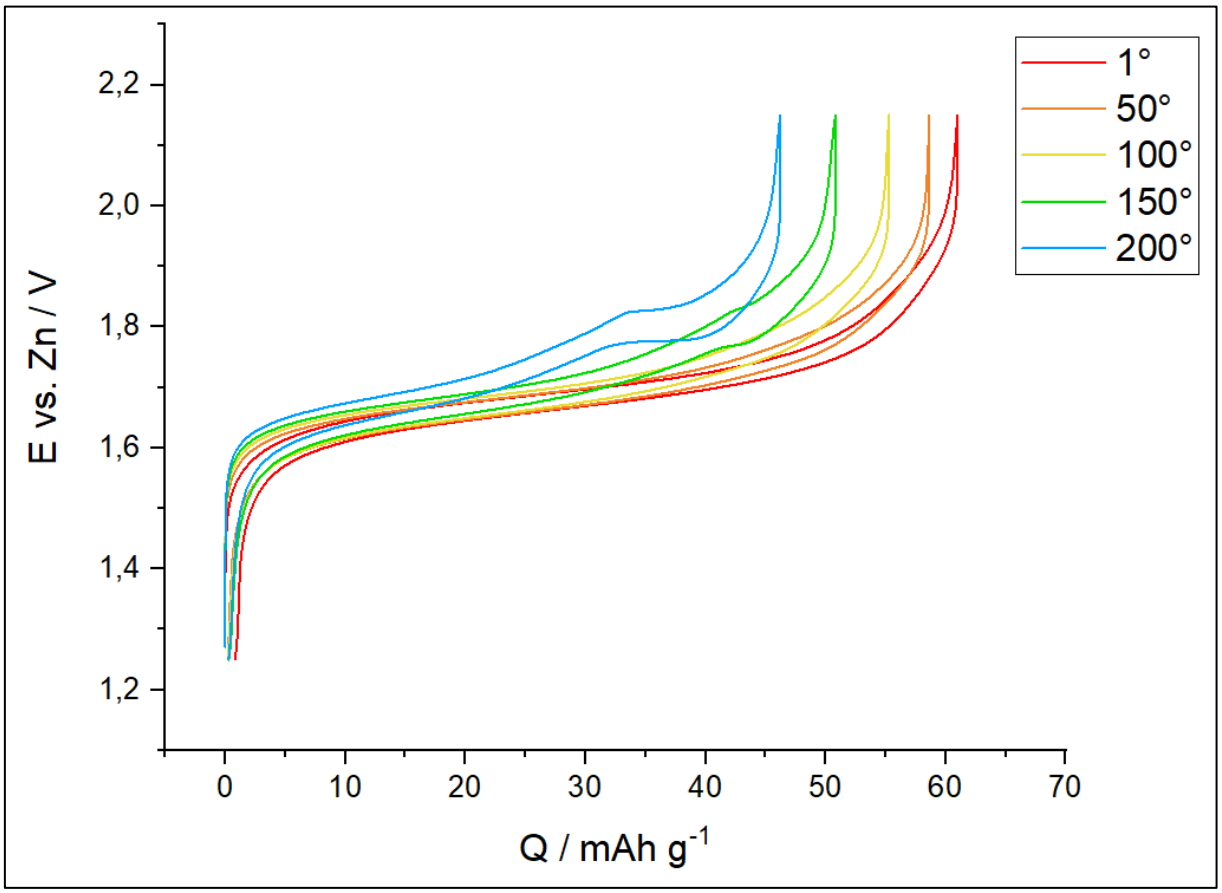

Figure 5.19: Galvanostatic cycle plot (1C rate) of CuHCF 100:100 with a solution of 100 mM $ZnSO_4$ and 50 mM KCl for 1st, 50th, 100th, 150th and 200th cycle.

In figure 5.19 the 1st, 50th, 100th, 150th and 200th galvanostatic cycle plots of CuHCF 100:100 with a solution of 100 mM $ZnSO_4$ and 50 mM KCl are shown. The potential is measured vs. Zn. These data are also taken from the first measurement of the third batch of the standard synthesis. Starting with an initial specific charge capacity of 60.19 mAh g^{-1}, the capacity retention of the working electrode decreases to 80% after 174 cycles, reaching a specific charge of 48.27 mAh g^{-1}.

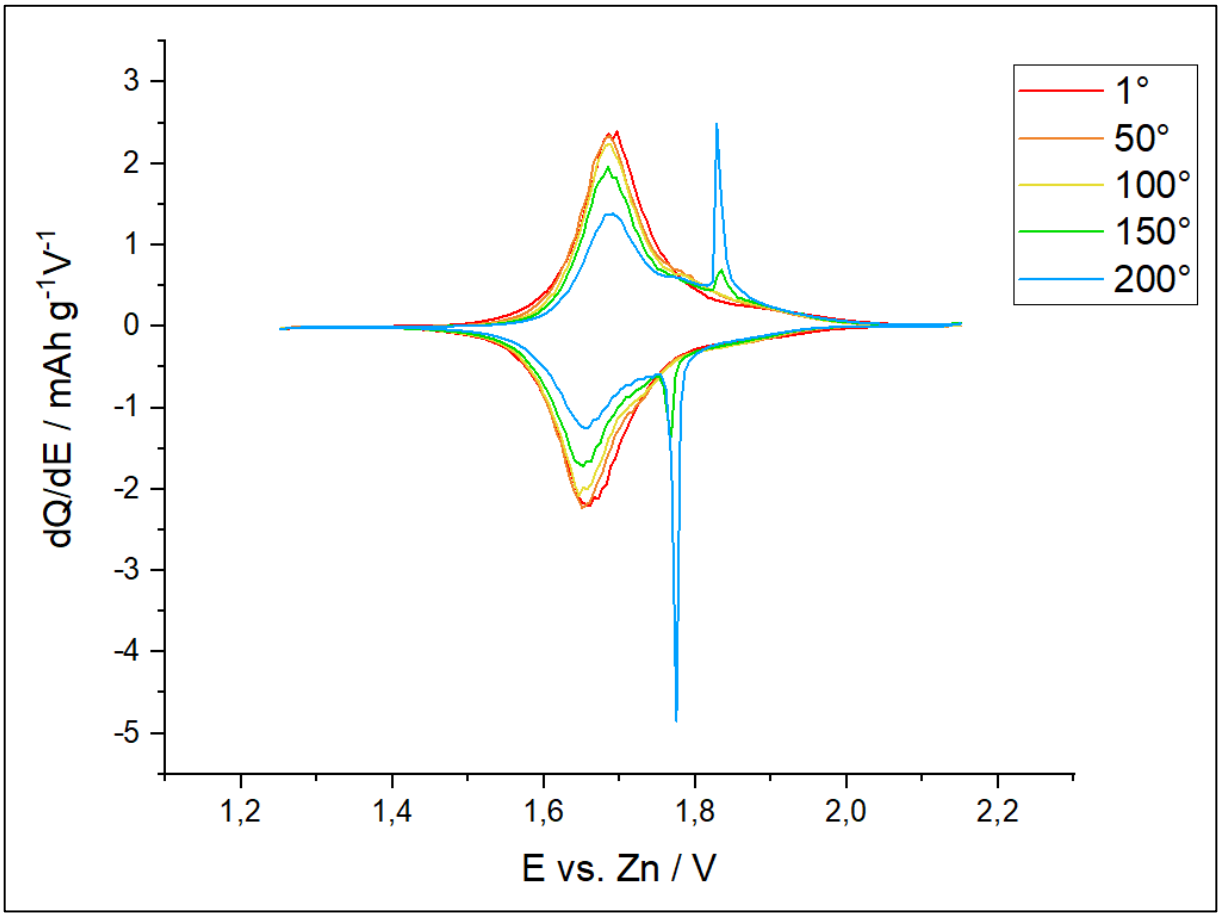

Figure 5.20: Differential charge plot of CuHCF 100:100 with a solution of 100 mM $ZnSO_4$ and 50 mM KCl for 1st, 50th, 100th, 150th and 200th cycle.

Figure 5.20 shows the differential charge of the CuHCF 100:100 at the 1st, 50th, 100th, 150th and 200th cycle with a solution of 100 mM $ZnSO_4$ and 50 mM KCl. The potential is measured vs. Zn. These data are also taken from the first measurement of the third batch of the standard synthesis. For both oxidation and reduction processes two peaks are visible. The second peaks appear at the 128th cycle and start to grow in a spike shape from the 139th cycle while the first peaks start to decrease. The average potential of the second peaks is 1.80 V.

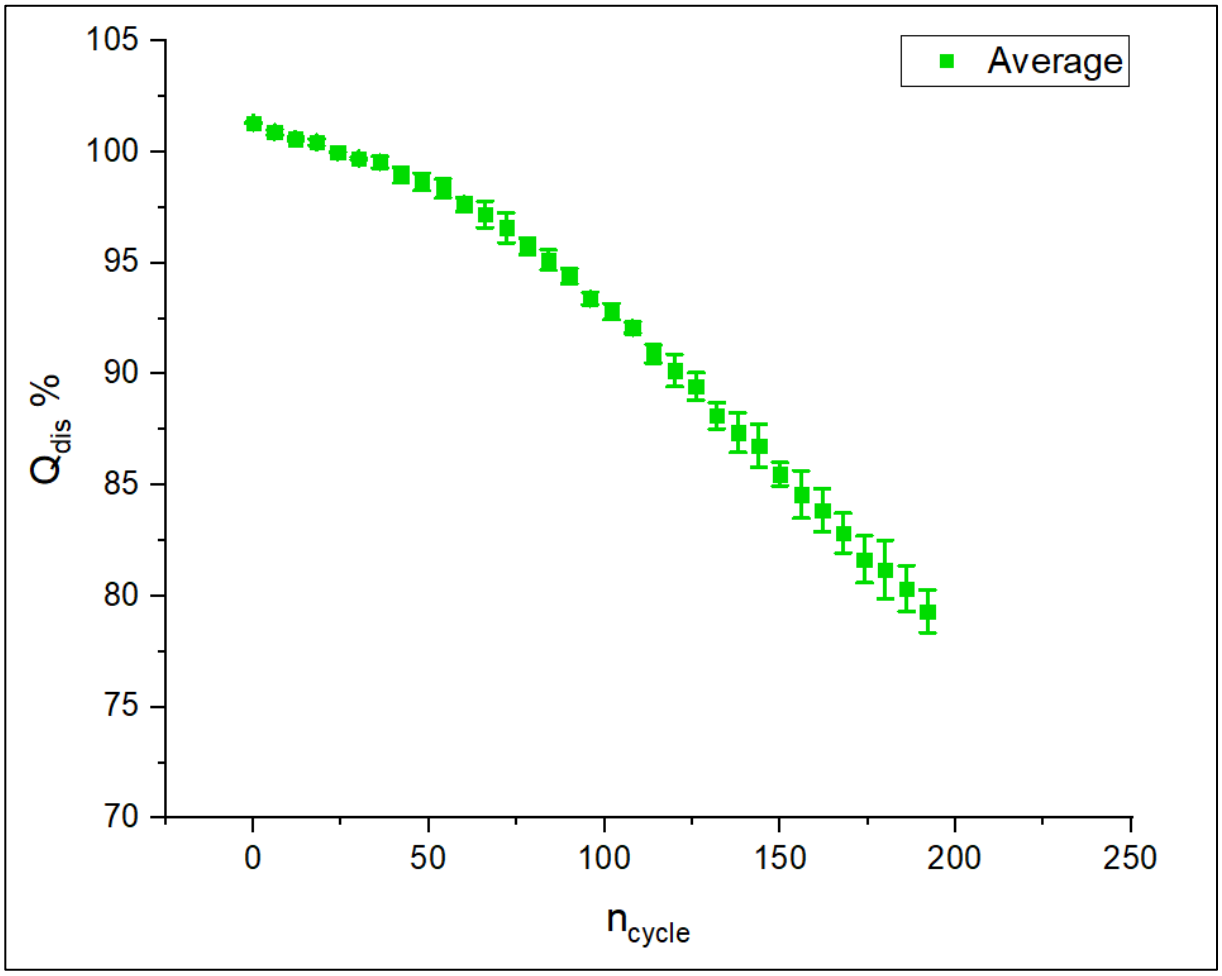

Figure 5.21: Average charge retention of the CuHCF 100:100 electrodes with a solution of 100 mM $ZnSO_4$ and 50 mM KCl galvanostatically cycled at 1C vs. Zn. The retention has been normalized by the charge at the 25th cycle.

Figure 5.21 shows the mean value of the CuHCF electrode charge retention related to the number of cycles. The values are generated after full reduction of the CuHCF electrode and plotted in percentage referring to the charge reached at the 25th cycle during the measurement. The average and standard deviation have been calculated by comparing two different samples resulting from the third batch of the second synthesis of CuHCF 100:100. The first measurement achieved a retention of 80% at the 193th cycle. The second measurement reached a retention of 80% after 183 cycles. The maximum standard deviation is 1.46.

5.5.4. CuHCF 100 :100 with 300mM KNO_3

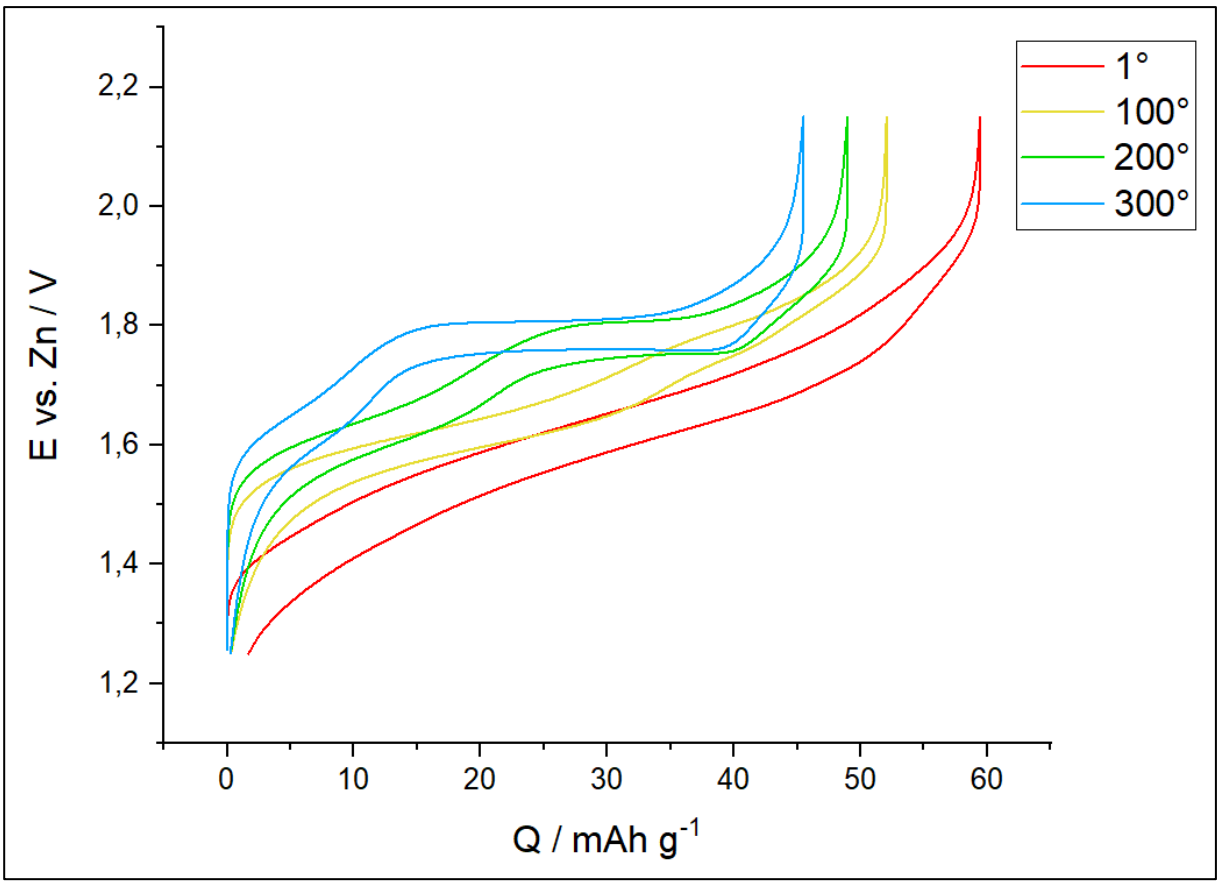

Figure 5.22: Galvanostatic cycle plot (1C rate) of CuHCF 100:100 with 300 mM KNO_3 (20') for 1st, 100th, 200th and 300th cycle.

In figure 5.22 the 1st, 100th, 200th and 300th galvanostatic cycle plots of CuHCF 100:100 with 300 mM KNO_3 synthesis are shown. The potential is measured vs. Zn. These data are taken from the first batch of the first synthesis of CuHCF 100:100 with 300 mM KNO_3 with a centrifuge time of 20 minutes. Starting with an initial specific charge capacity of 57.79 mAh g^{-1}, the specific charge of the working electrode decreases to 45.29 mAh g^{-1} after 302 cycles, which is equal to retention of 82.24%.

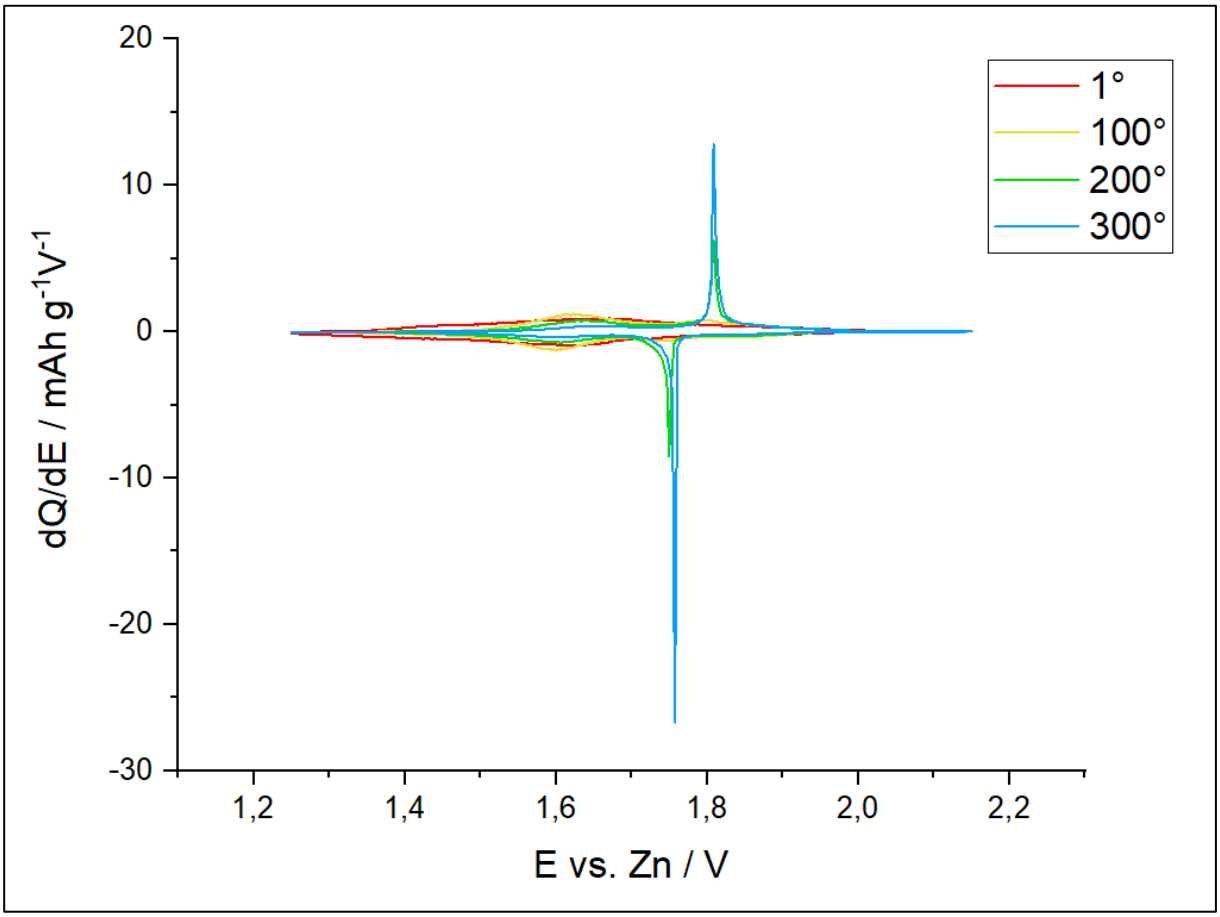

Figure 5.23: Differential charge plot of CuHCF 100:100 with 300 mM KNO_3 (20') for 1st, 100th, 200th and 300th cycle.

Figure 5.23 shows the differential charge of the CuHCF 100:100 with 300 mM KNO_3 synthesis at the 1st, 100th, 200th and 300th cycle. The potential is measured vs. Zn. These data are taken from the first batch of the first synthesis of CuHCF 100:100 with 300 mM KNO_3 with a centrifuge time of 20 minutes. Oxidation and reduction peaks are visible for all cycles. For both oxidation and reduction processes two peaks are visible. The second peaks appear at the 32th cycle and start to grow in a spike shape from the 133th cycle while the first peaks start to decrease. The average potential of the second peaks is 1.79 V.

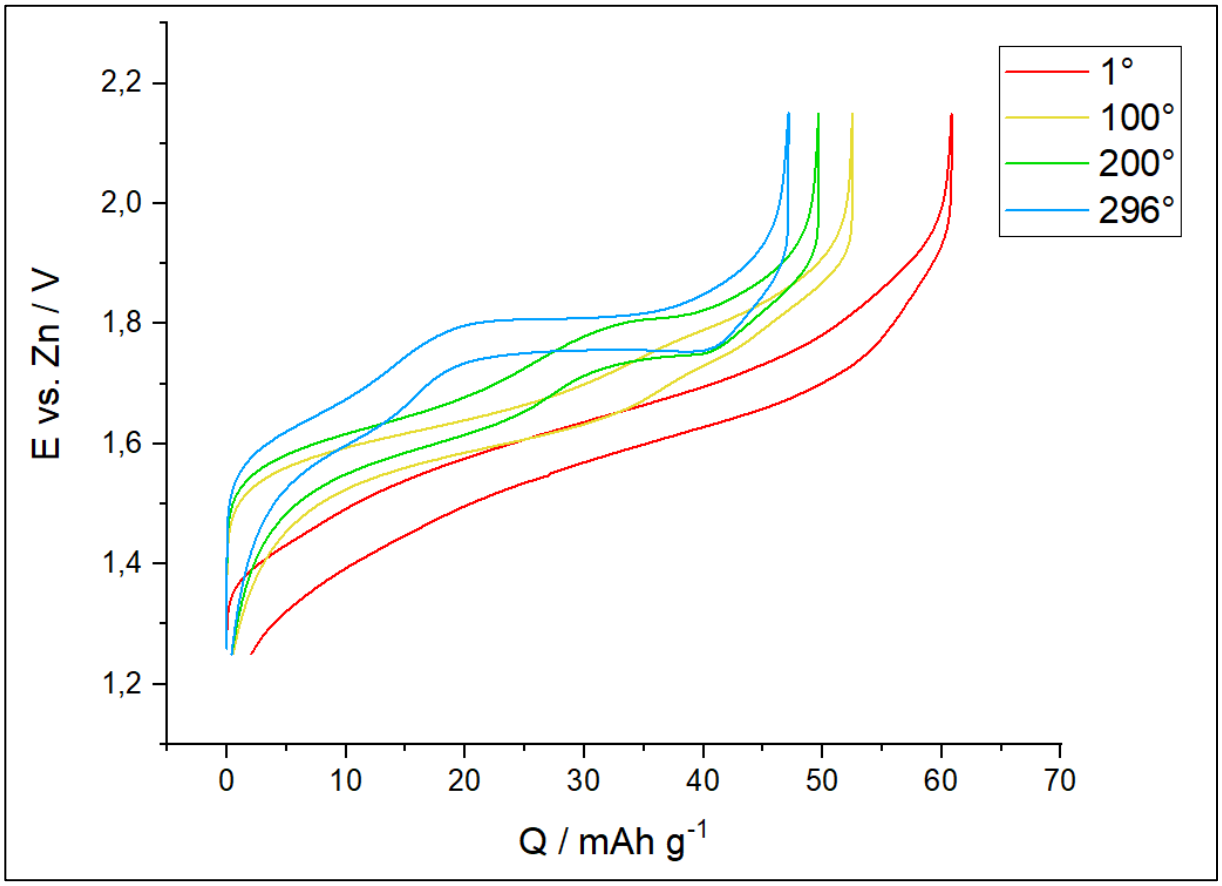

Figure 5.24: Galvanostatic cycle plot (1C rate) of CuHCF 100:100 with 300 mM KNO_3 (10') for 1st, 100th, 200th and 300th cycle.

In figure 5.24 the 1st, 100th, 200th and 300th galvanostatic cycle plots of CuHCF 100:100 with 300 mM KNO_3 synthesis are shown. The potential is measured vs. Zn. These data are taken from the first batch of the first synthesis of CuHCF 100:100 with 300 mM KNO_3 with a centrifuge time of 10 minutes. Starting with an initial specific charge capacity of 58.79 mAh g^{-1}, the specific charge of the working electrode decreases to 46.68 mAh g^{-1} after the 296th cycles, which is equal to retention of 83.86%.

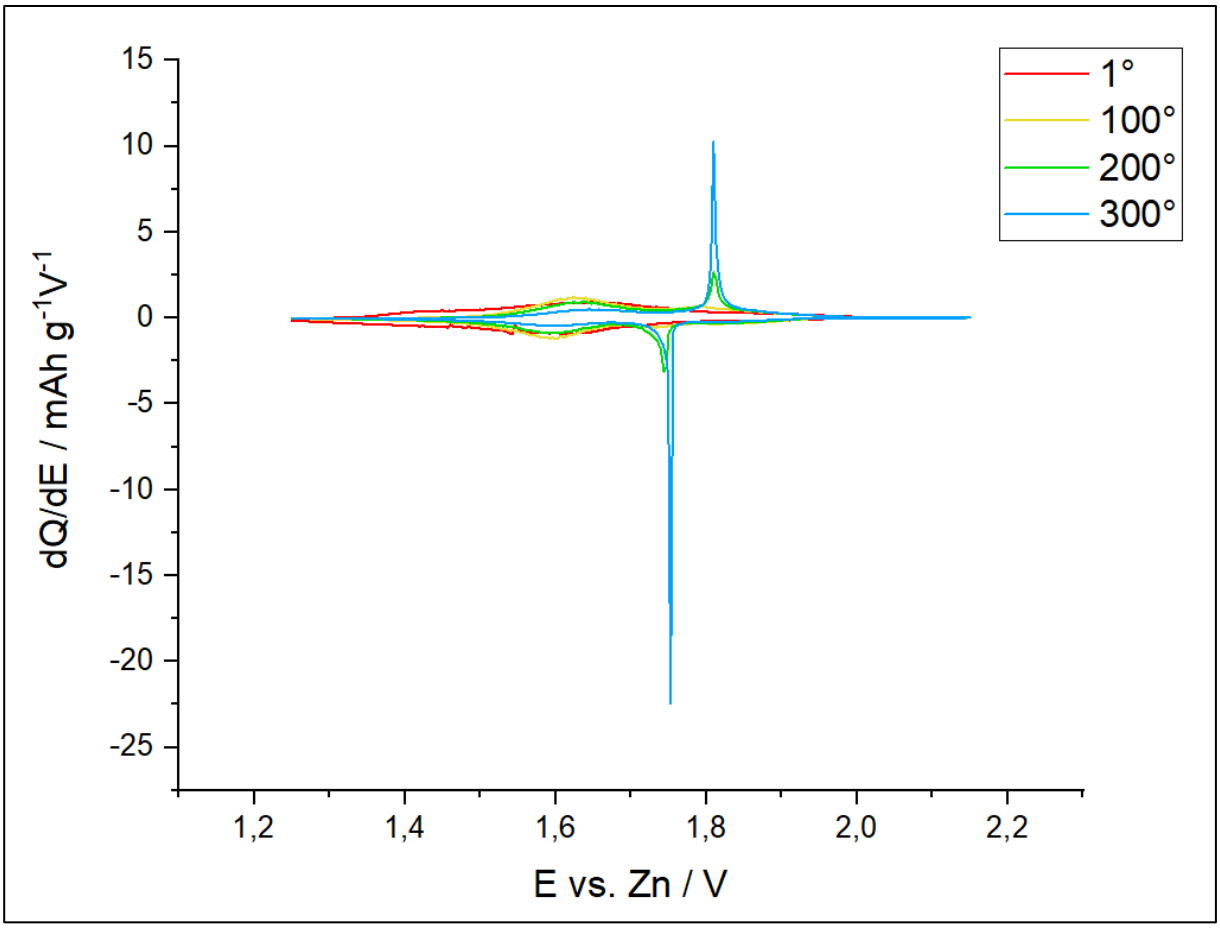

Figure 5.25: Differential charge plot of CuHCF 100:100 with 300 mM KNO_3 (10') for 1st, 100th, 200th and 300th cycle.

Figure 5.25 shows the differential charge of the CuHCF 100:100 with 300 mM KNO_3 synthesis at the 1st, 100th, 200th and 300th cycle. The potential is measured vs. Zn. These data are taken from the first batch of the first synthesis of CuHCF 100:100 with 300 mM KNO_3 with a centrifuge time of 10 minutes. Oxidation and reduction peaks are visible for all cycles. For both oxidation and reduction processes two peaks are visible. The second peaks appear at the 29th cycle and start to grow in a spike shape from the 158th cycle while the first peaks start to decrease. The average potential of the second peaks is 1.78 V.

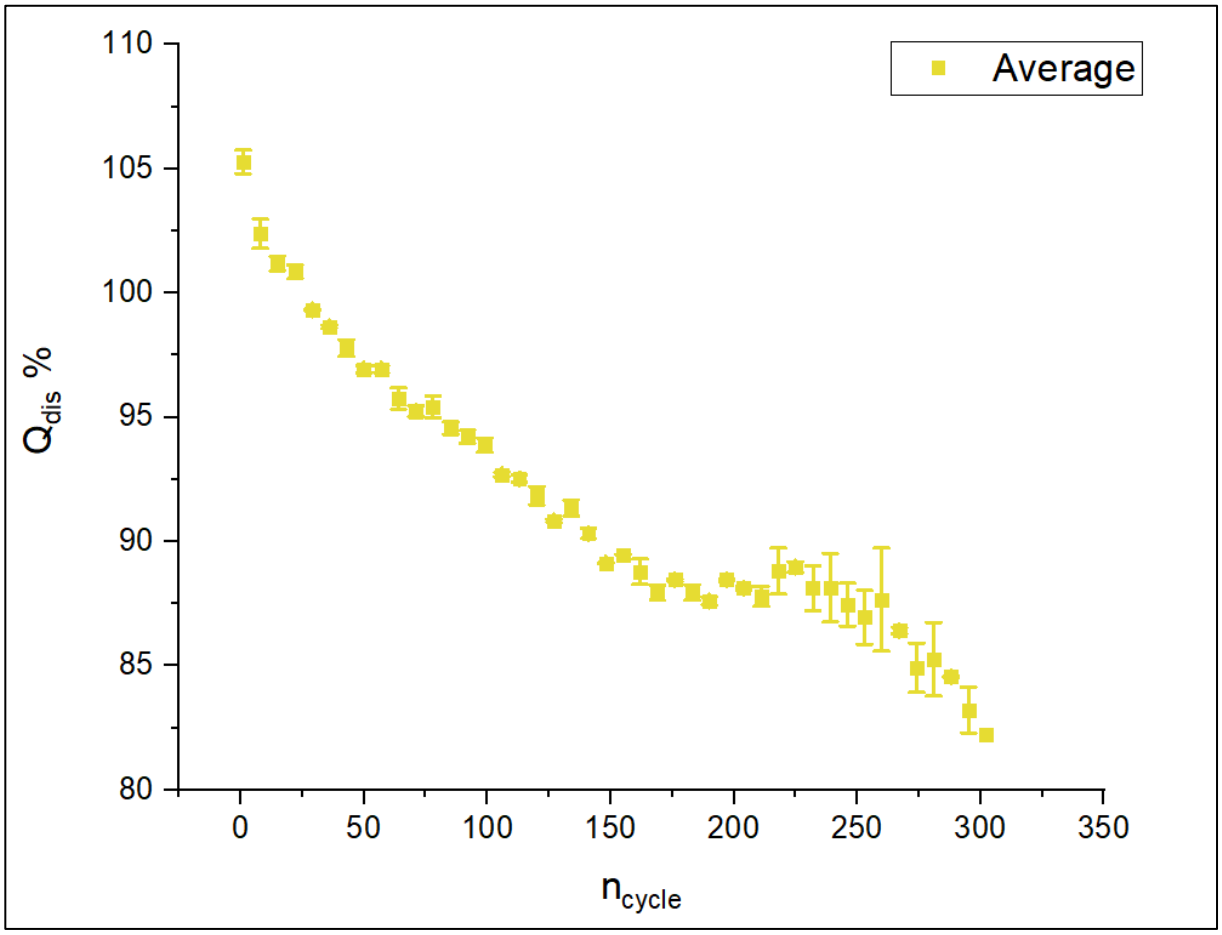

Figure 5.26: Average charge retention of the CuHCF 100:100 electrodes with 300 mM KNO_3 galvanostatically cycled at 1C vs. Zn. The retention has been normalized by the charge at the 25th cycle.

Figure 5.26 shows the mean value of the CuHCF electrode charge retention related to the number of cycles. The values are generated after full reduction of the CuHCF electrode and plotted in percentage referring to the charge reached at the 25th cycle during the measurement. The average and standard deviation have been calculated by comparing two different samples resulting from the first batch of the first synthesis of CuHCF 100:100 with 300 mM KNO_3. The first measurement (10 minutes centifruge) achieved a retention of 83.86% at the 296th cycle. The second measurement (20 minutes centifruge) reached a retention of 82.24% after 302 cycles. The maximum standard deviation is 2.33.

5.5.5. CuHCF 100 :100 with 600mM KNO_3

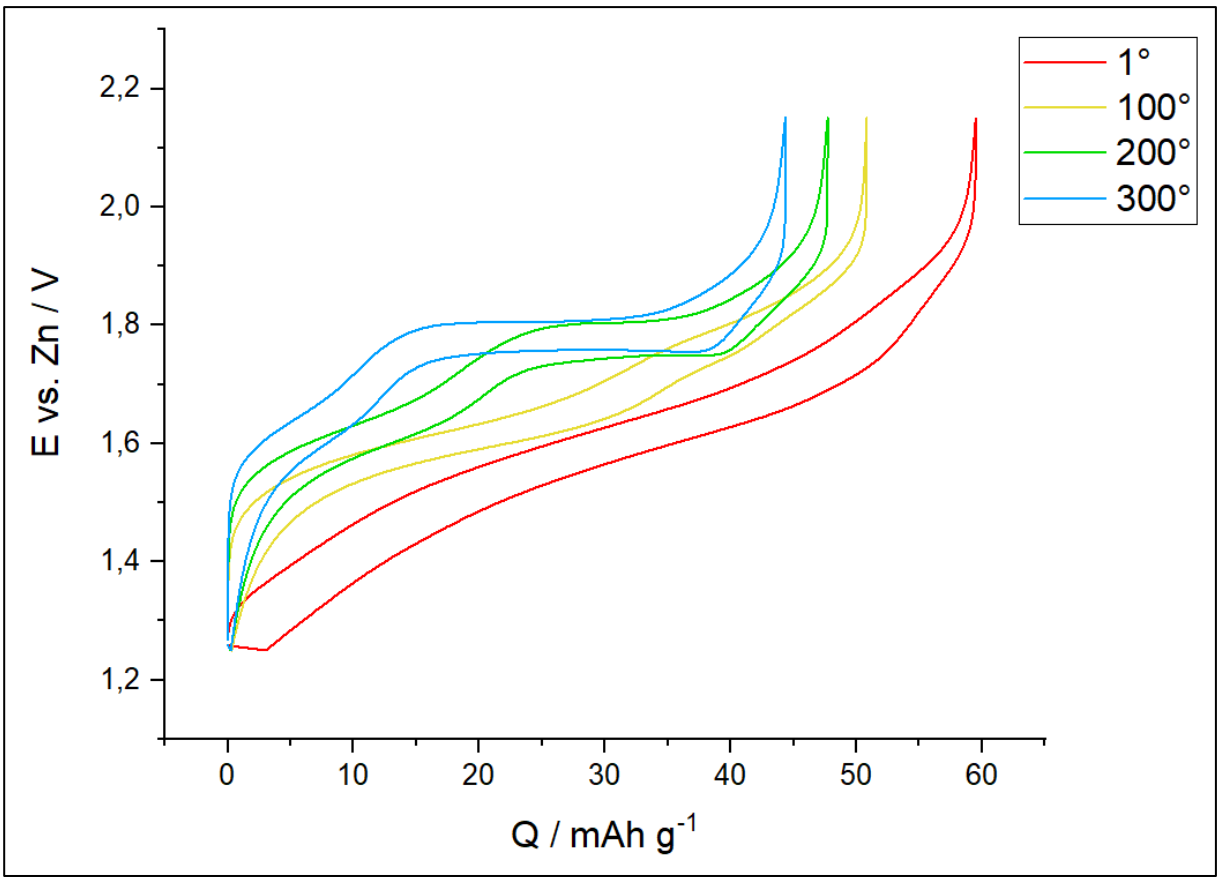

Figure 5.27: Galvanostatic cycle plot (1C rate) of CuHCF 100:100 with 600 mM KNO_3 for 1st, 100th, 200th and 300th cycle.

In figure 5.27 the 1st, 100th, 200th and 300th galvanostatic cycle plots of CuHCF 100:100 with 600 mM KNO_3 synthesis are shown. The potential is measured vs. Zn. These data are taken from the first batch of the first synthesis of CuHCF 100:100 with 600 mM KNO_3. Starting with an initial specific charge capacity of 57.83 mAh g^{-1}, the specific charge of the working electrode decreases to 42.92 mAh g^{-1} after 343 cycles, which is equal to retention of 80%.

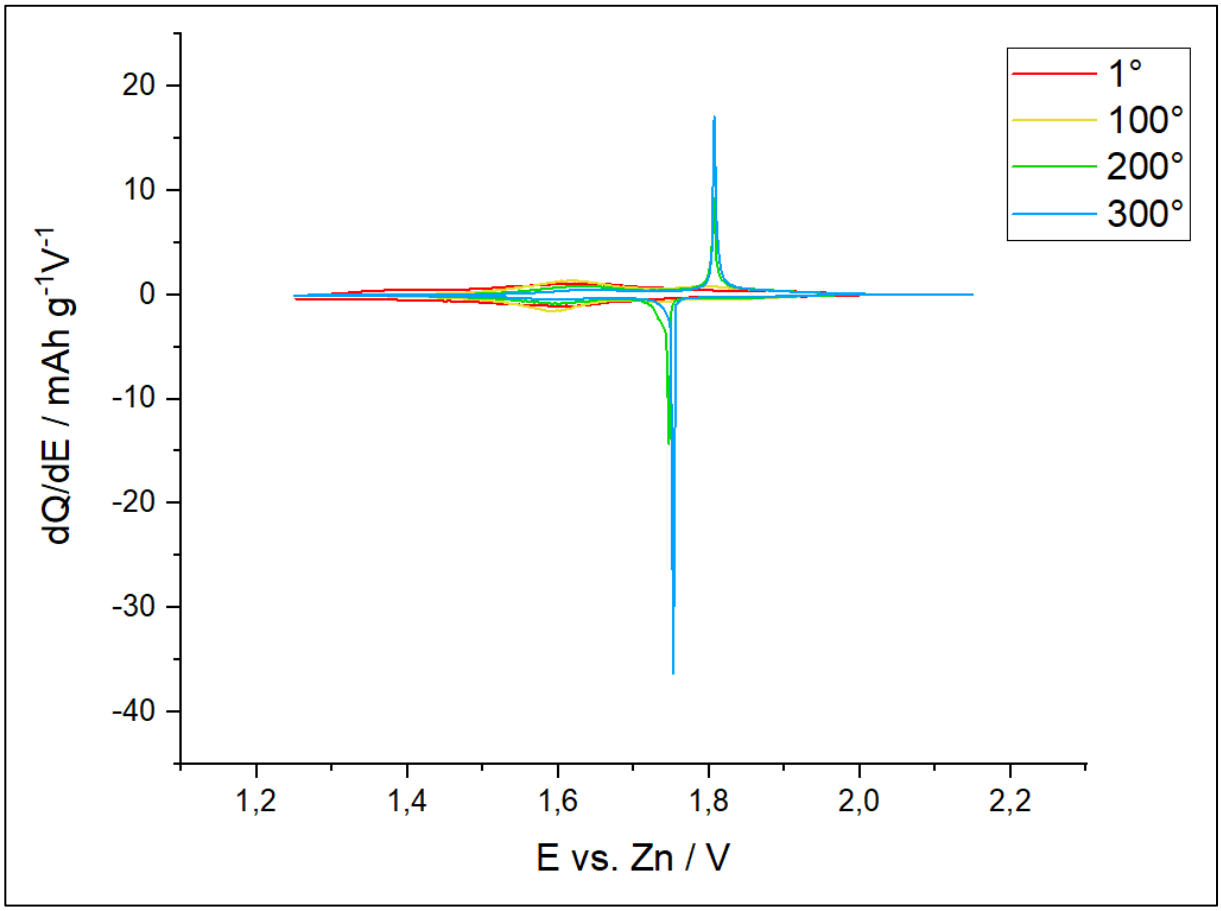

Figure 5.28: Differential charge plot of CuHCF 100:100 with 600 mM KNO_3 for 1st, 100th, 200th and 300th cycle.

Figure 5.28 shows the differential charge of the CuHCF 100:100 with 600 mM KNO_3 synthesis at the 1st, 100th, 200th and 300th cycle. The potential is measured vs. Zn. These data are taken from the first batch of the first synthesis of CuHCF 100:100 with 600 mM KNO_3. Oxidation and reduction peaks are visible for all cycles. For both oxidation and reduction processes two peaks are visible. The second peaks appear at the 24th cycle and start to grow in a spike shape from the 137th cycle while the first peaks start to decrease. The average potential of the second peaks is 1.79 V.

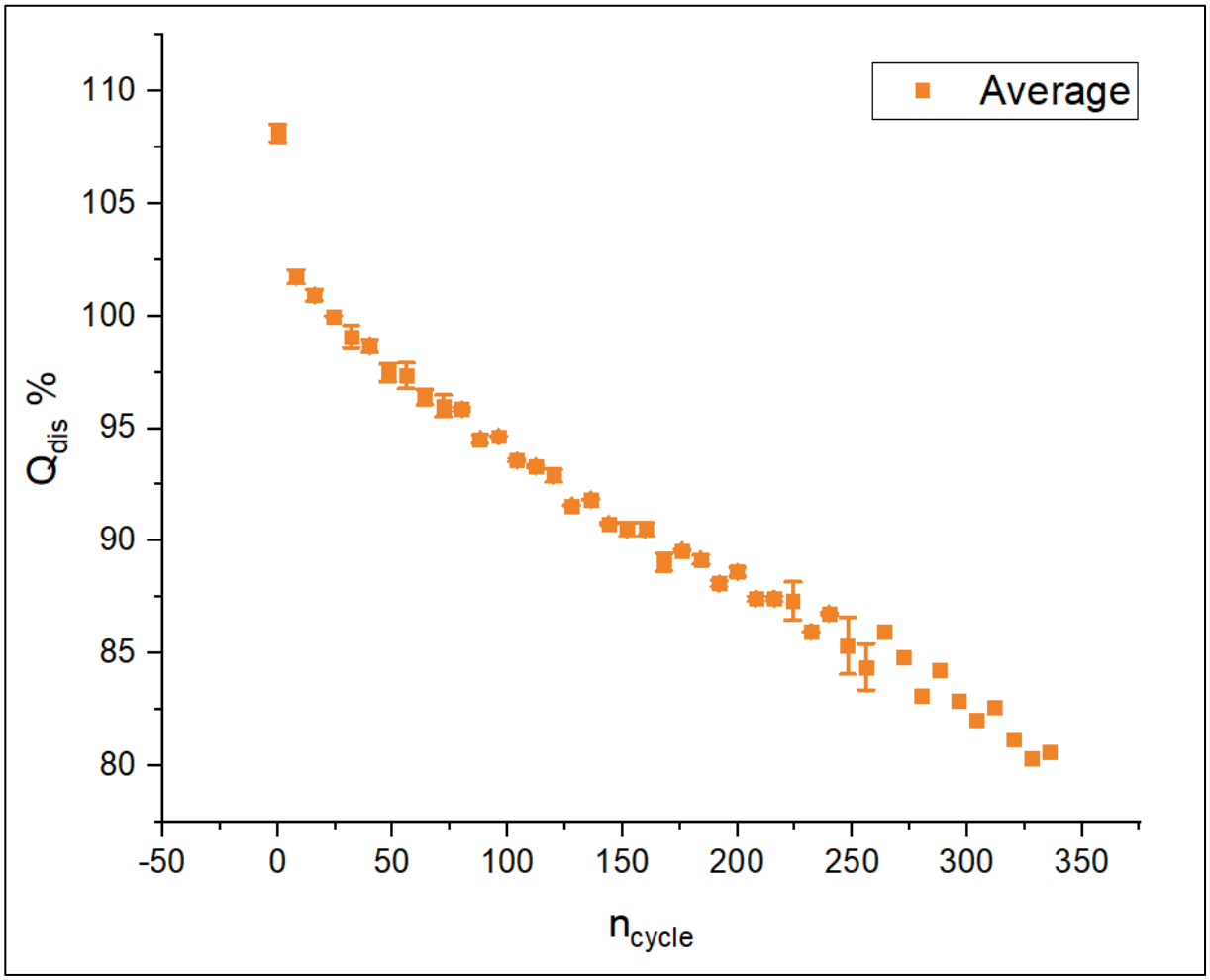

Figure 5.29: Average charge retention of the CuHCF 100:100 electrodes with 600 mM KNO_3 galvanostatically cycled at 1C vs. Zn. The retention has been normalized by the charge at the 25th cycle.

Figure 5.29 shows the mean value of the CuHCF electrode charge retention related to the number of cycles. The values are generated after full reduction of the CuHCF electrode and plotted in percentage referring to the charge reached at the 25th cycle during the measurement. The average and standard deviation have been calculated by comparing two different samples resulting from the first batch of the first synthesis of CuHCF 100:100 with 600 mM KNO_3. The first measurement achieved a retention of 83.15% at the 296th cycle. The second measurement reached a retention of 83.67% after 257 cycles. The maximum standard deviation is 1.34.

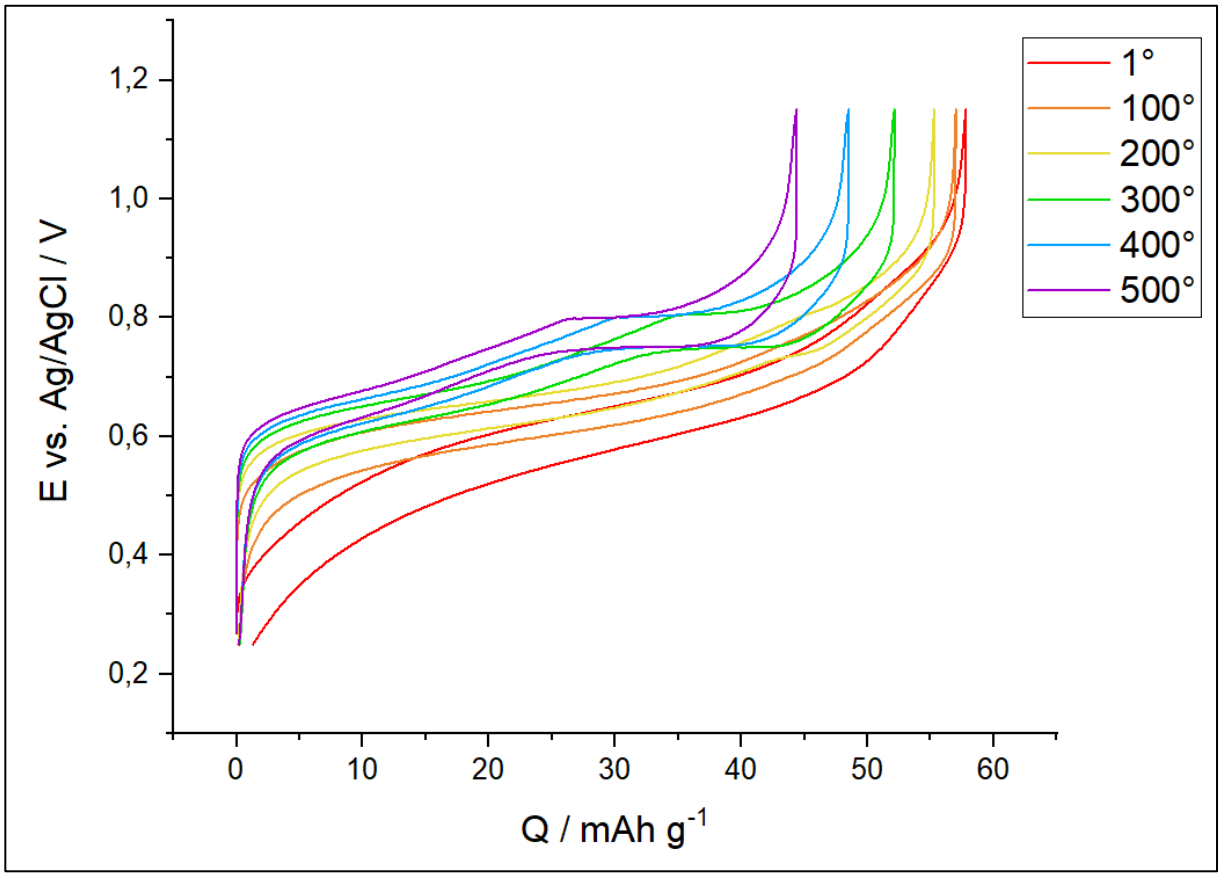

Figure 5.30: Galvanostatic cycle plot (1C rate) of CuHCF 100:100 with 600 mM KNO_3 for 1st, 100th, 200th, 300th and 400th cycle.

In Figure 5.30 the 1st, 100th, 200th, 300th and 400th galvanostatic cycle plots of CuHCF 100:100 with 600 mM KNO_3 synthesis are shown. The potential is measured vs. Ag/AgCl in 3 M KCl. These data are taken from the first batch of the first synthesis. Starting with an initial specific charge capacity of 56.48 mAh g^{-1} the capacity retention of the working electrode decreases to 80.13% after 474 cycles, reaching a specific charge of 45.26 mAh g^{-1}.

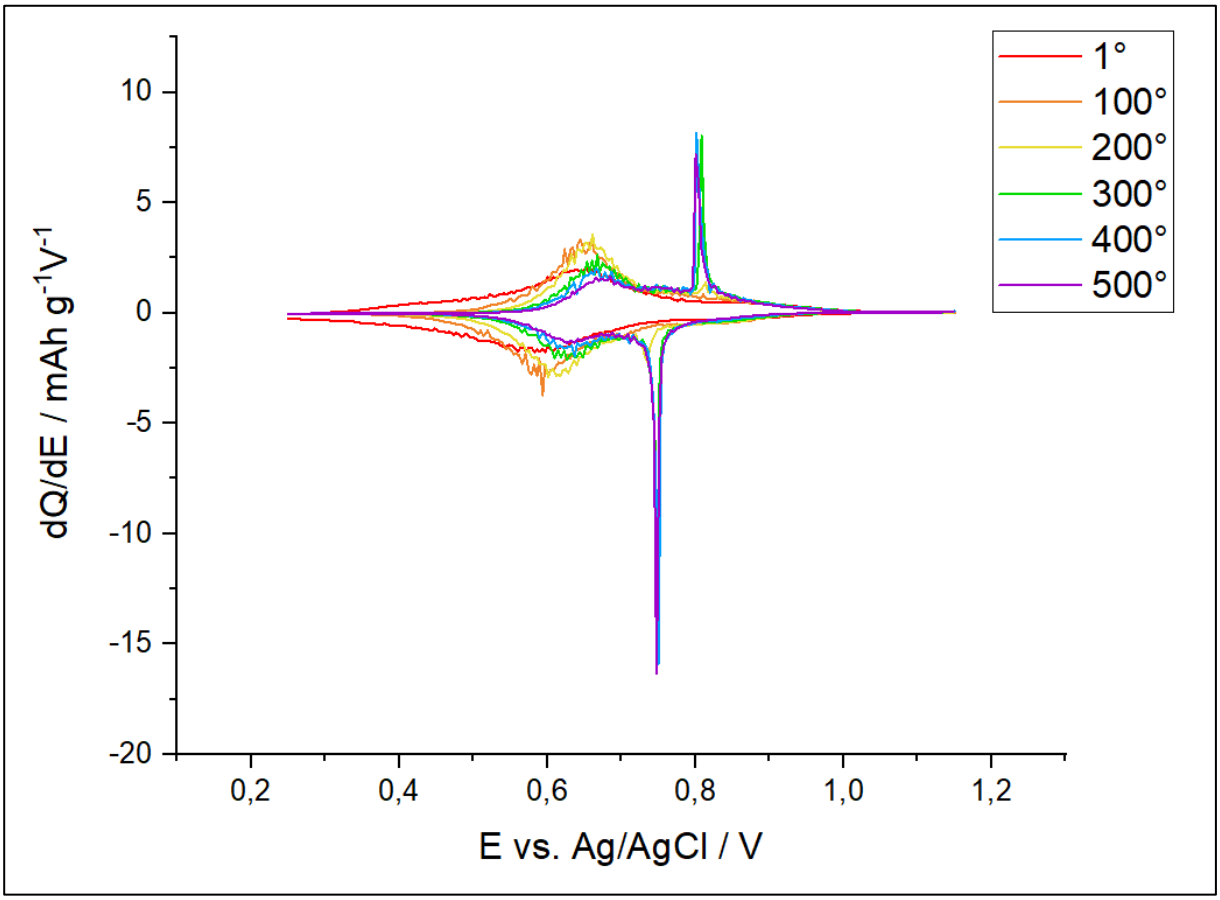

Figure 5.31. *Differential charge plot of CuHCF 100:100 with 600 mM KNO_3 for 1st, 100th, 200th, 300th and 400th cycle.*

Figure 5.31 shows the differential charge of the CuHCF 100:100 at the 1st, 100th, 200th, 300th and 400th cycle. The potential is measured vs. Ag/AgCl in 3 M KCl. These data are also taken from the first batch of the synthesis. For both oxidation and reduction processes two peaks are visible. The second peaks appear at the 159th cycle and start to grow in a spike shape from the 184th cycle while the first peaks start to decrease. The average potential of the second peaks is 0.78 V.

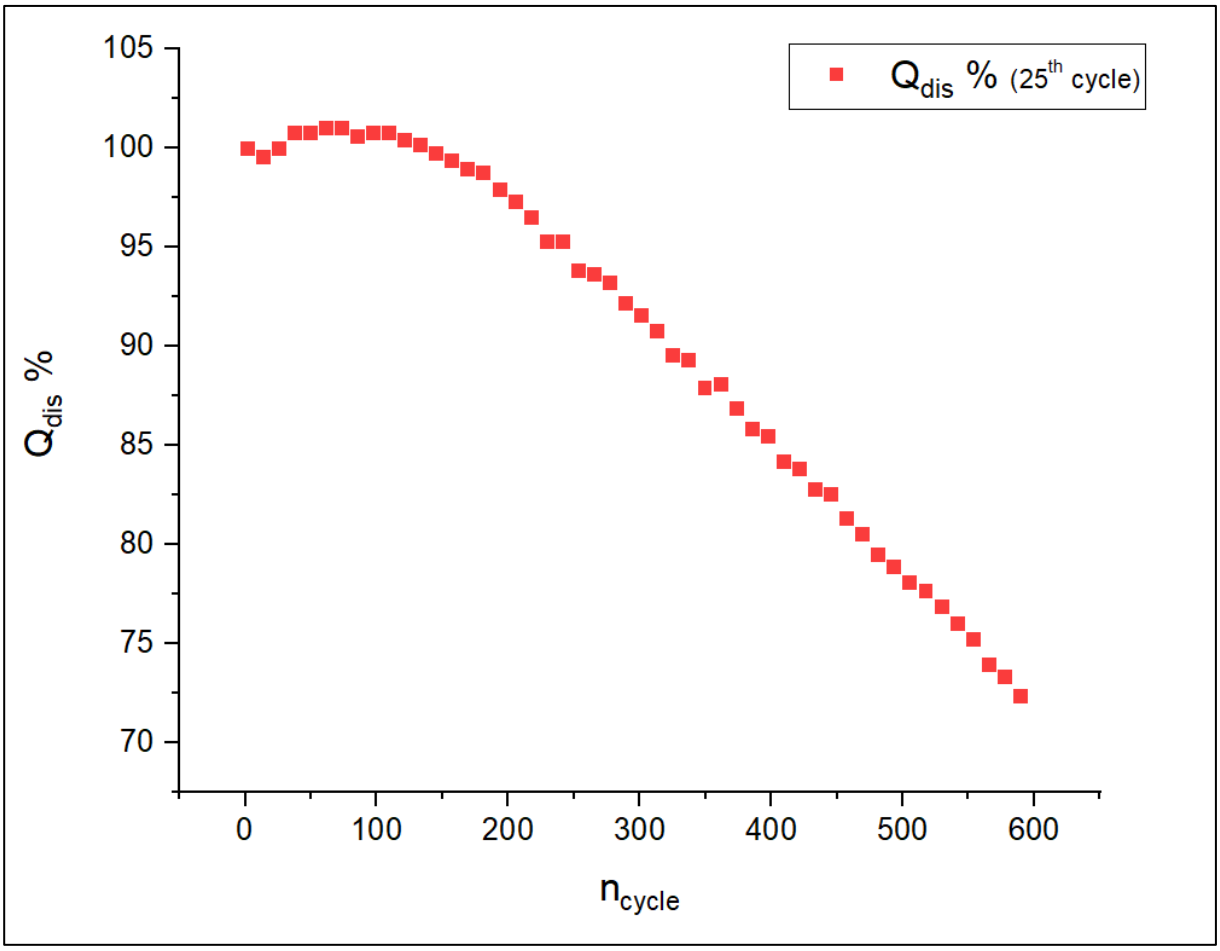

Figure 5.32: Charge retention of CuHCF 100:100 with 600 mM KNO_3 electrodes galvanostatically cycled at 1C vs. Zn. The retention has been normalised by the charge at the 25th cycle.

Figure 5.32 shows the decreasing of the capacity of the CuHCF 100:100 with 600 mM KNO_3 related to the number of cycles. The values are generated after full reduction of the CuHCF electrode and plotted in percentage referring to the charge reached at the 25th cycle during the measurement.

5.5.6. CuHCF 100 :100 (2 weeks immersed)

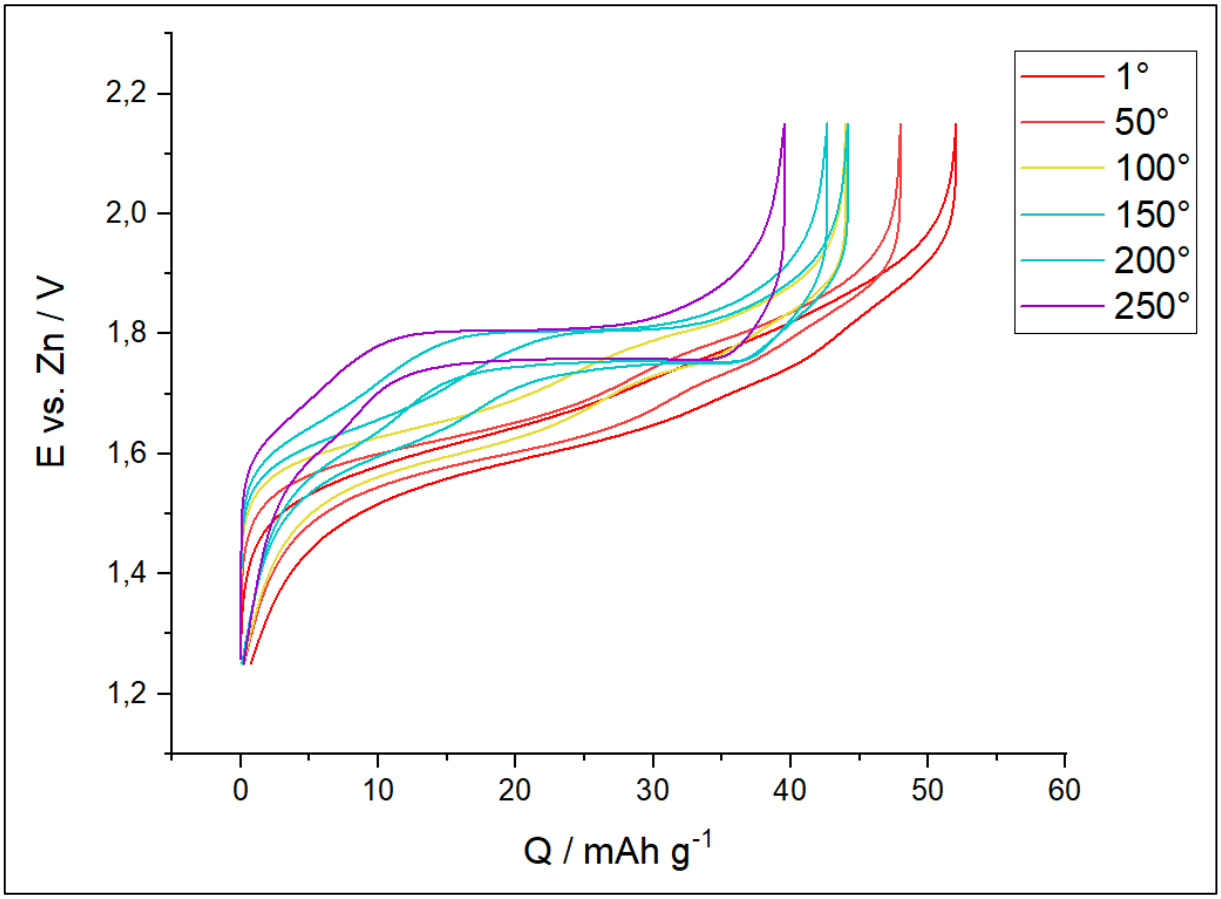

Figure 5.33: Galvanostatic cycle plot (1C rate) of CuHCF 100:100 (immersed for two weeks) for 1st, 50th, 100th, 150th, 200th and 250th cycle.

In Figure 5.33 the 1st, 50th, 100th, 150th, 200th and 250th galvanostatic cycle plots of CuHCF 100:100 synthesis are shown. After being cycled for 3 cycles to let the zinc ions intercalate inside the material, the electrodes were immersed for two weeks in a solution of 100 mM $ZnSO_4$. The potential is measured vs. Zn. These data are taken from the 2nd measurement of the second batch from the second synthesis of CuHCF 100:100. Starting with an initial specific charge capacity of 51.27 mAh g^{-1}, the specific charge of the working electrode decreases to 39.80 mAh g^{-1} after 237 cycles, which is equal to retention of 80%. Before being immersed, the initial specific charge was 54.13 mAh g^{-1} for the first electrode. For the second electrode, the initial specific capacity was 53.08 mAh g^{-1} while the initial capacity after being immersed is 50.35 mAh g^{-1}.

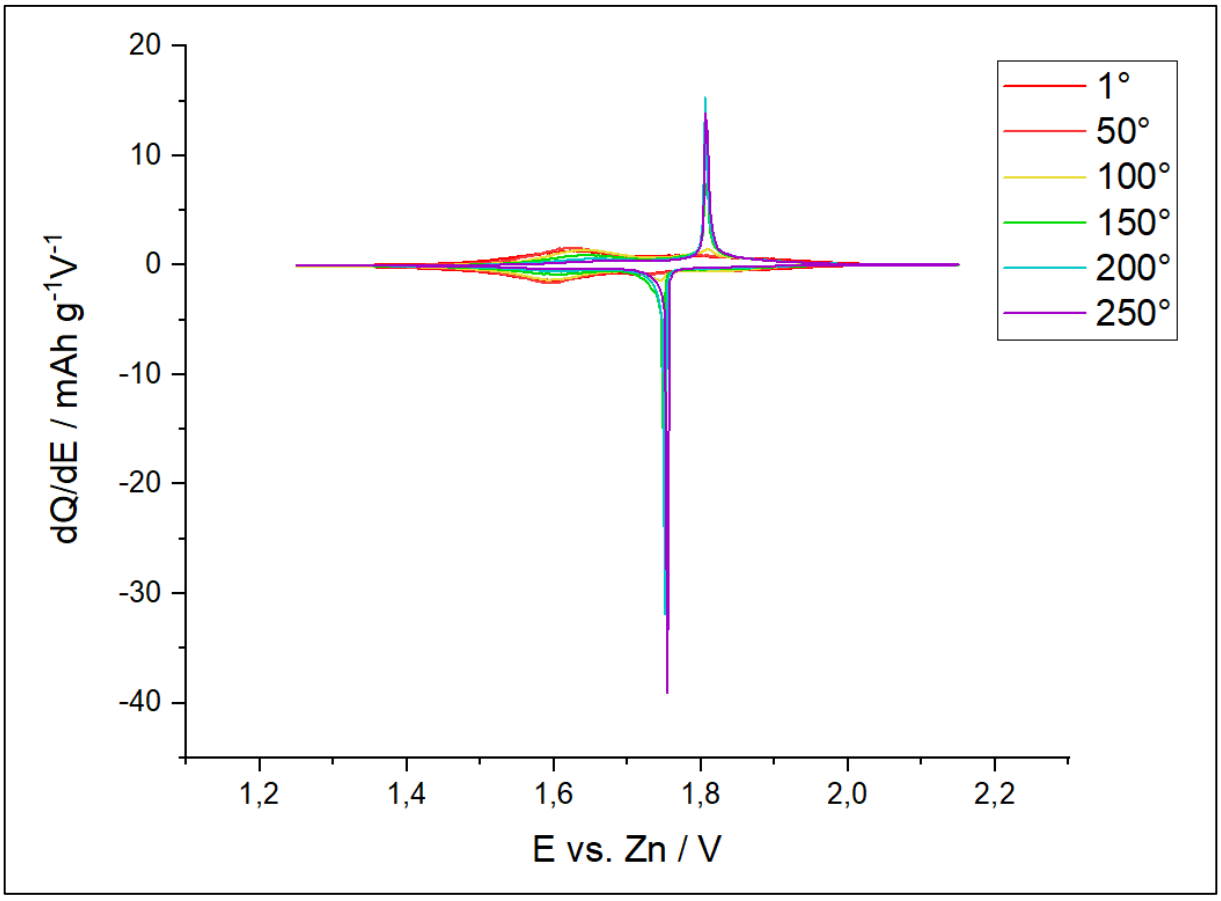

Figure 5.34: Differential charge plot of CuHCF 100:100 (immersed for two weeks) for 1st, 50th, 100th, 150th, 200th and 250th cycle.

Figure 5.34 shows the differential charge of the CuHCF 100:100 at the 1st, 50th, 100th, 150th, 200th and 250th cycle. The potential is measured vs. Zn. These data are taken from the 2nd measurement of the second batch from the second synthesis of CuHCF 100:100. Oxidation and reduction peaks are visible for all cycles. For both oxidation and reduction processes two peaks are visible. The second peaks appear weakly at the 6th cycle and start to grow in a spike shape from the 86th cycle while the first peaks start to decrease. The average potential of the second peaks is 1.79 V.

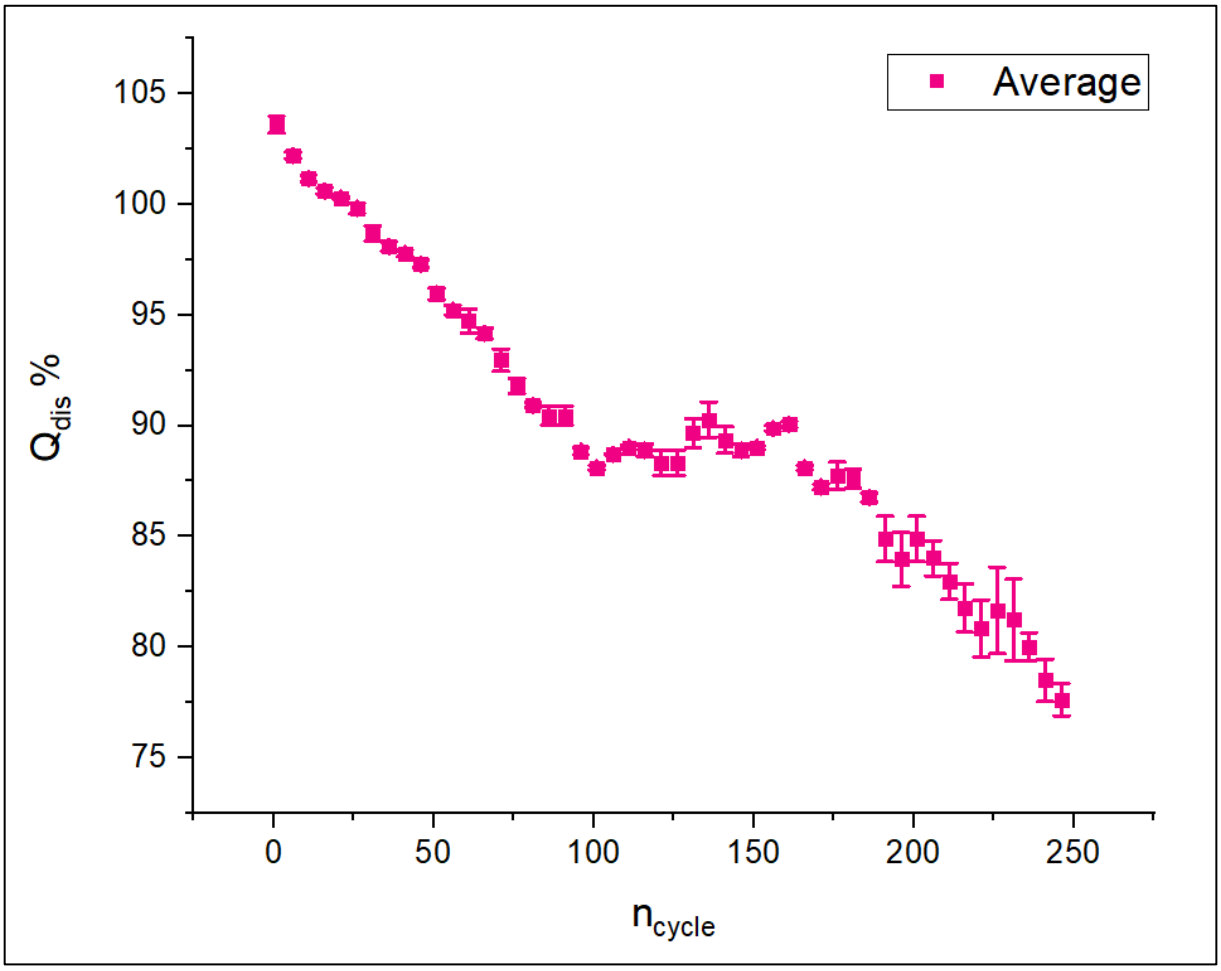

Figure 5.35: Average charge retention of the CuHCF 100:100 electrodes immersed for two weeks galvanostatically cycled at 1C vs. Zn. The retention has been normalized by the charge at the 25th cycle.

Figure 5.35 shows the mean value of the CuHCF electrode charge retention related to the number of cycles. The values are generated after full reduction of the CuHCF electrode and plotted in percentage referring to the charge reached at the 25th cycle during the measurement. The average and standard deviation have been calculated by comparing two different samples resulting from the 1st and 2nd measurement of the second batch from the second synthesis of CuHCF 100:100. The first measurement achieved a retention of 80.28% at the 230th cycle with a specific charge of 39.04 mAh g^{-1}. The second measurement reached a retention of 80.21% after 237 cycles with a specific charge of 29.80. The maximum standard deviation is 2.08.

5.6. Overview

In this section a comparative overview of the results is presented.

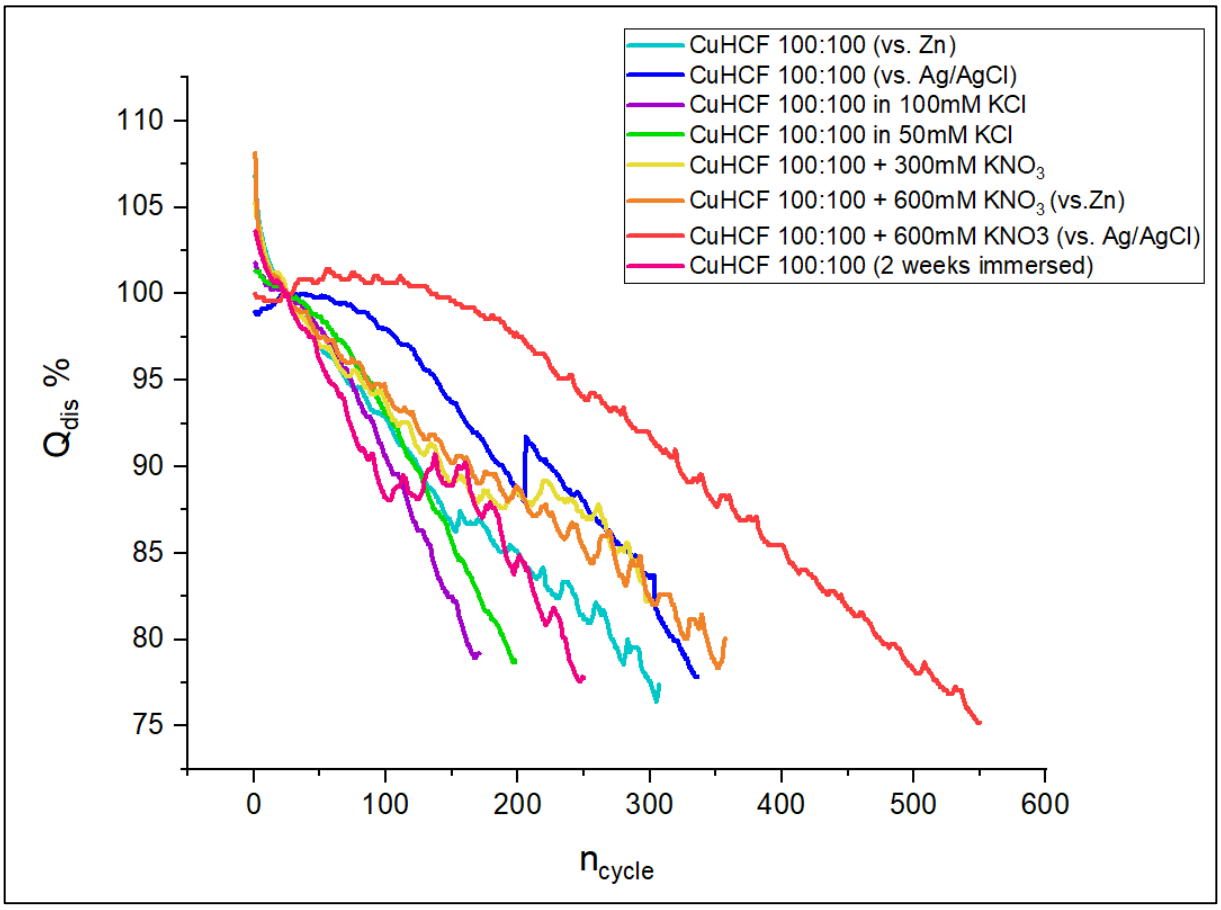

Figure 5.36: Charge retention plot of all measurements.

For all the measures carried out with zinc as reference electrode, the specific capacity starts to drop from the beginning. Conversely, the electrodes cycled against Ag/AgCl show a slightly increase of the specific capacity (Figure 5.36) as also shown by the values at the 25th cycle (see table 5.3).

The capacity retention trend of the electrodes immersed for two weeks (see Figure 5.35) shows a similar plateau to the 300 mM KNO_3 electrodes (see Figure 5.26) at c.a. 87% of the specific charge.

Among all the measurements, the electrodes of 600 mM KNO_3 synthesis show the highest life-cycle. In addition, the electrodes of this synthesis cycled with zinc as reference electrode lasted almost as long as the standard copper hexacyanoferrate

cycled against the silver/silver chloride RE. Thus, a concentration of 600 mM of KNO_3 or higher could play an important role in slowing the aging of the electrodes.

Table 5.3: Initial specific capacity, specific capacity at 25th cycle and the total cycles number at a capacity retention of 84% of all the measurements.

	Q_{dis} in. [mAh/g]	**Q_{dis} (25°)** [mAh/g]	**N° cycle at 84%**
CuHCF 100:100 (E vs Zn)	55.69	51.98	211
CuHCF 100:100 (E vs Ag/AgCl)	58.65	60.26	328
CuHCF 100:100 100 mM KCl solution	60.39	59.34	138
CuHCF 100 :100 50 mM KCl solution	60.19	59.42	166
CuHCF 100:100 + 300 mM KNO3 (10‘)	58.79	55.66	274
CuHCF 100:100 + 300 mM KNO3 (20‘)	57.79	55.07	290
CuHCF 100:100 + 600 mM KNO3 (E vs Zn)	57.83	53.61	294
CuHCF 100:100 + 600 mM KNO3 (E vs Ag/AgCl)	56.48	56.60	419
CuHCF 100 :100 2 weeks immersed	51.27	49.62	209

For all the measurements, Table 5.3 compares the initial specific capacity, specific capacity at 25th cycle and the total cycles number at a charge retention of 84%. As shown in Table 5.3, the specific capacity is not constant but varies between 60.40 mAh g^{-1} and 51.27 mAh g^{-1}. The higher values are shown for the electrodes cycled with potassium chloride in the solution while the lower ones are shown for the electrodes immersed for two weeks in a 100 mM $ZnSO_4$ solution. The specific capacity outcomes of the experiments with potassium nitrate in the synthesis have derived similar results to the standard synthesis. However, since also electrodes of the same batch have shown different values of specific capacity, a correlation to explain this trend cannot be done.

Among the all measurements, the electrodes that lasted longer are the ones cycled with Ag/AgCl as reference electrode. The lower life cycle values were obtained with the standard electrodes with the solutions of 100 mM KCl and 50 mM KCl in addition

to the 100 mM $ZnSO_4$. Thus, the right potassium chloride concentration and/or a gradual release of the KCl solution might play important role in the aging of the electrodes.

Table 5.4: Cycle of the 2° plateau, cycle of the spike-shape plateau and average potential of the 2° plateau for all the measurements.

	2° plateau (cycle)	**Spike-shape** (cycle)	**2° plateau** E [V]
CuHCF 100:100 (E vs Zn)	28	159	1.79
CuHCF 100:100 (E vs Ag/AgCl)	197	215	0.79
CuHCF 100:100 100 mM KCl solution	-	-	-
CuHCF 100 :100 50 mM KCl solution	128	139	1.80
CuHCF 100:100 + 300 mM KNO3 (10‘)	29	158	1.78
CuHCF 100:100 + 300 mM KNO3 (20‘)	32	133	1.79
CuHCF 100:100 + 600 mM KNO3 (E vs Zn)	24	137	1.79
CuHCF 100:100 + 600 mM KNO3 (E vs Ag/AgCl)	159	184	0.78
CuHCF 100 :100 2 weeks immersed	6	86	1.79

In Table 5.4 are shown the cycle number at which the phase transition starts to occur, the number of the cycle at which the second phase peak starts to grow in a spike-shape and the average potential of the second plateau. These data were taken from the differential charge plot of the measurements. For the electrodes cycled against zinc, the second phase appears earlier compared to the measurements with silver/silver chloride as reference electrode. Interestingly, the second peaks of the electrodes with zinc as RE start to turn into a spike-shape much later then the electrodes with Ag/AgCl as RE from the moment their appearance. This suggests that the delay of the second phase formation might be responsible for the longer life cycle of the electrodes. Thus, potassium and chloride ions may have a key role in postponing the electrodes’ aging.

The experiment with a solution of 100 mM of KCl didn't show any second phase peak. This could suggest that a high concentration of the potassium and chloride ions may play an important role in the delaying of the phase transformation. However, this measure showed the lowest life cycle. Thus, a too high KCl concentration might damage the crystal structure of the material. The same trend of silver/silver chloride measures (e.g. delayed second phase formation) can be seeing also for the experiments with a 50 mM KCl solution. However, also in this case the life cycle is lower. Therefore, 50 mM of KCl might still be too high.

The average potential of the second phase formation is 1.79 V for the measurements with zinc as reference electrode and 0.79 V for the ones with silver/silver chloride. Therefore, the phase transformation occurs at the same potential given a reference electrode.

6. CONCLUSIONS

Among the members of the Prussian Blue analogues' family, CuHCF is particularly promising as positive electrode material for aqueous ZIBs because of its low costs, non-toxicity, excellent power capability, and relatively simple synthesis route, which could enable the production of larger amounts of material at an industrial scale[10]. In the first part of this work, a basic study of the electrochemical behavior of the active material was carried out by voltametric and scanning electrochemical microscopy measurements.

The voltammograms obtained were typical of an electrolytic solution containing Zn^{2+} ions (Figure 5.2). Two pairs of peaks were clearly distinguished, both the peaks attributed to the redox system $[Fe(CN_6]^{3-}$ / $[Fe(CN)_6]^{2-}$, and the peaks assigned to the (de-)intercalation of Zn^{2+} in the CuHCF crystal structure.

The cyclic voltammograms recorded in stationary conditions were used to establish the mass actually present on the electrode surface. The higher mass value was obtained with the lowest scan rate, while the lower mass value was obtained with the higher scan rate, as shown in Table 5.2, with an average value of 0.18 mg (see section 5.2).

The SECM measurements on CuHCF films were conducted using [FcTMA] $[PF_6]$ as a redox mediator (see section 5.3). The approach curves obtained on the active part of the electrode clearly show a positive feedback (Figure 5.4), proving that the substrate is conductive. The approach curves were obtained on the insulating part show, as expected, a negative feedback (Figure 5.6). In order to establish the degree of homogeneity of the CuHCF film, from the point of view of the active centers, linear scans and 3D were performed to cover areas larger than those that could be evaluated by means of an approach curve. For each curve performed in a given direction, the corresponding one in the opposite direction was recorded, so as to verify that the observed signals were not artifacts due to uncontrolled phenomena (see section 5.4). The series of voltammograms were superimposable and the scan rates showed an irregular surface of different degree in some point of the material

(Figure 5.8). Finally, 3D surface maps were recorded. As shown in Figure 5.9, active and least active areas present in the CuHCF film can be distinguished.

In the second part of the thesis, a deeper study was performed by changing some variables during the synthesis and carrying out different experiments in order to achieve a better understanding of what might cause the aging of the system. Here, different experiments have been conducted to achieve a better understanding of the role of potassium ions within the synthesis of copper hexacyanoferrate and the potassium chloride as electrolyte. For this purpose, three main synthesis have been conducted: CuHCF 100:100 (standard), standard with 300 mM KNO_3, standard with 600 mM KNO_3. Two types of experiments have been carried out on the electrolyte: co-presence of potassium chloride and zinc sulfate and the zinc ion role in the absence of the electrochemical performance. The role of the electrolyte has been investigated with the electrodes of the standard material. In addition, the role of centrifuge time was also investigated on the standard with 300 mM KNO_3 electrodes. These experiments were conducted to understand if a longer centrifugation time would lead to a better washing of the material and therefore to an increase in the electrode performance (see section 4.2). The outcomes in section 5.6.4 show that the performances of the electrodes are very close in terms of initial specific capacity and life cycle. This is further confirmed by the average charge retention (see Figure 5.26) which shows a very similar trend of both types of electrodes. Hence, the centrifuge time does not influence the performance of the electrodes.

The measures conducted with silver/silver chloride as reference electrode have shown a longer life cycle compared to the measures with zinc as RE (see table 5.3). These outcomes drove the choice of using potassium chloride as electrolyte with the zinc sulfate (see section 4.4). The working electrodes immersed in the solution of KCl added have been utilized with a zinc foil as a reference electrode. Two potassium chloride concentrations have been investigated: 100 mM KCl and 50 mM KCl. The first concentration has resulted in a high initial specific capacity (see table 5.3). In addition, no second phase peaks were visible in the differential capacity plot (see Figure 5.17). As mentioned before, the phase formation may involve a partial substitution of Cu^{2+} with Zn^{2+} in the B sites of the CuHCF crystal, with the

consequent formation of a distorted CuZnHCF phase[14,15]. The delayed second phase formation observed with the measurements with Ag/AgCl as reference electrode may suggest that the right potassium and chloride ions concentration might have a major role in the delaying of the electrodes' aging. However, despite the absence of the second phase, the performance of the 100 mM KCl solution experiment has led to the lowest life cycle value among the other measurements. Thus, a too high KCl concentration might lead to a faster aging of the material. The outcomes of the potassium chloride concentration of 50 mM show a second phase formation (see Figure 5.21) and a delay similar to the measures obtained with electrodes of the standard material cycled against Ag/AgCl (see table 5.4). However, also in this case a low life cycle value has been obtained. Therefore, a concentration of 50 mM of KCl might still be too high and lead to a faster aging of the material.

As mentioned before, it has been hypothesized that the phase transformation process might also occur in the absence of the electrochemical one for direct reaction between the material and the electrolyte (see section 4.6). For this purpose, the electrodes have been immersed in the electrolyte (100 mM $ZnSO_4$) for two weeks after three cycle. For both the electrodes of the CuHCF 100:100 previously cycled the specific capacity dropped by 3-4 mAh g^{-1} after being immersed (see section 5.6.6). Interestingly, the life cycle is similar to the standard electrodes cycled against zinc (see table 5.3). Thus, a previous immersion of the electrodes in the electrolyte may be responsible for the capacity decreasing but does not influence the electrochemical performance.

7. REFERENCES

[1] – H. Mayer, *Air pollution in cities*, Atmospheric Environment 33 (1999) 4029-4037, https://doi.org/10.1016/S1352-2310(99)00144-2.

[2] - H. Ritchie, Our World in Data, 2017, https://ourworldindata.org/how-long-before-we-run-out-of-fossil-fuels.

[3]- Z. Yang, J. Zhang, M. C. W. Kintner-Meyer, *Electrochemical Energy Storage for Green Grid,* Chem. Rev. 2011, 111, 3577 –3613, https://doi.org/10.1021/cr100290v

[4]- J. Morales, R. Trocoli, J. Santos-Pena, *A $LiFePO_4$-Based Cell with Li_x(Mg) as Lithium Storage Negative Electrode,* Electrochemical and Solid-State Letters, 12 (7) A145-A149 (2009), https://doi.org/10.1149/1.3129126

[5] - W. Tang, Y. Zhu, Y. Hou, *Aqueous rechargeable lithium batteries as an energy storage system of superfast charging,* Energy Environ. Sci. 2013, 6, 2093– 2104, https://doi.org/10.1039/C3EE24249H

[6] - J. M. Tarascon, *Is Lithium the new gold?*, Nat. Chem., 2010, 2, 510

[7] - C. D. Wessells, R. A. Huggins, Y. Cui, *Copper hexacyanoferrate battery electrodes with long cycle life and high power*, Nat. Commun. 2011, 2, 550, 10.1038/ncomms1563.

[8] - Bellis, Mary. *"Biography of Alessandro Volta, Inventor of the Battery."* ThoughtCo, Aug. 27, 2020, thoughtco.com/alessandro-volta-1992584.

[9] [68]– G. Kasiri, J. Glennberg, A. B. Hashemi, R. Kun, F. La Mantia, *Mixed copper-zinc hexacyanoferrates as cathode materials for aqueous zinc-ion batteries,* Energy Storage Materials 19 (2019) 360–369, https://doi.org/10.1016/j.ensm.2019.03.006

[10] - G. Zampardi, M. Warnecke, *Effect of the reactants concentration on the synthesis and cycle life of copper hexacyanoferrate for aqueous Zn-ion batteries*, Electrochemistry Communications 126 (2021) 107030, https://doi.org/10.1016/j.elecom.2021.107030

[11] - R. Guduru, J. Icaza, *A brief review on multivalent intercalation batteries with aqueous electrolytes*, Nanomaterials 6 (2016) 41, https://doi.org/10.3390/ nano6030041.

[12] - C.D. Wessells, R.A. Huggins, Y. Cui, *Copper hexacyanoferrate battery electrodes with long cycle life and high power*, Nat. Commun. 2 (2011) 550, https://doi.org/10.1038/ncomms1563.

[13] G. Zampardi, F. La Mantia, *Prussian blue analogues as aqueous Zn-ion batteries electrodes: Current challenges and future perspectives*, Curr. Opin. Electrochem. 21 (2020) 84–92, https://doi.org/10.1016/j.coelec.2020.01.014

[14]- R. Trocoli, G. Kasiri, F. La Mantia, *Phase transformation of copper hexacyanoferrate (KCuFe(CN)(6)) during zinc insertion: Effect of co-ion intercalation*, J. Power Sources 400 (2018) 167–171, https://doi.org/10.1016/j.jpowsour.2018.08.015.

[15] - G. Kasiri, J. Glenneberg, R. Kun, G. Zampardi, F. La Mantia, *Microstructural Changes of Prussian Blue Derivatives during Cycling in Zinc-Containing Electrolytes*, ChemElectroChem 7 (2020) 3301–3310, https://doi.org/10.1002/celc.202000886

[16] - R. Yazami, P. Touzain, A reversible graphite-lithium negative electrode for electrochemical generators, J. Power Sources 1983, 9, 365 – 371, https://doi.org/10.1016/0378-7753(83)87040-2.

[17] - Luo, J. Y.; Xia, Y. Y. *Aqueous Lithium-Ion Battery $LiTi_2(PO_4)_3/LiMn_2O_4$ with High Power and Energy Densities as well as Superior Cycling Stability*. Adv. Funct. Mater. 2007, 17, 3877−3884, https://doi.org/10.1002/adfm.200700638.

[18] - Li, W.; Dahn, J. R.; Wainwright, D. S. *Rechargeable Lithium Batteries with Aqueous Electrolytes*. Science 1994, 264, 1115−1118, 10.1126/science.264.5162.1115

[19] - Hwang, J.-Y.; Myung, S.-T.; Sun, Y.-K. *Sodium-Ion Batteries: Present and Future*. Chem. Soc. Rev. 2017, 46, 3529−3614, 10.1039/C6CS00776G.

[20] - Kim, H.; Hong, J.; Park, K. Y.; Kim, H.; Kim, S. W.; Kang, K. *Aqueous Rechargeable Li and Na Ion Batteries*. Chem. Rev. 2014, 114, 11788−11827. https://doi.org/10.1021/cr500232y.

[21] - Stanley M Whittingham (2 December 2012). *INTERCALATION CHEMISTRY*. Elsevier. ISBN 978-0-323-14040-9.

[22] - Kwon, Jethro Mullen and K. J. (2 September 2016). "Samsung is recalling the Galaxy Note 7 worldwide over battery problem". *CNNMoney*.

[23]https://www.upsbatterycenter.com/blog/intercalation-work-batteries/#prettyPhoto

[24] - Yoshino, A. *The Birth of the Lithium-Ion Battery*. Angew. Chem., Int. Ed. 2012, 51, 5798−5800. https://doi.org/10.1002/anie.201105006

[25] - Winter, M.; Brodd, R. J. *What Are Batteries, Fuel Cells, and Supercapacitors?* Chem. Rev. 2004, 104, 4245−4270. https://doi.org/10.1021/cr020730k

[26] - Yamamoto, T.; Shoji, T. Rechargeable Zn|$ZnSO_4$|MnO_2-type Cells. Inorg. Chim. Acta 1986, 117, L27−L28.

[27] -G. Kasiri, R. Trócoli, A. B. Hashemi, F. La Mantia. 2016. *An electrochemical investigation of the aging of copper hexacyanoferrate during the operation in zinc-ion batteries.* Electrochimica Acta 222, 74–83. https://doi.org/10.1016/j.electacta.2016.10.155

[28] – G. Fang, J. Zhou, A. Pan, S. Liang. 2018. *Recent Advances in Aqueous Zinc-Ion Batteries.* ACS Energy Lett. 3, 10, 2480–2501. https://doi.org/10.1021/acsenergylett.8b01426

[29] - A. Kraft, et al., *On the discovery and history of Prussian blue*, Bull. Hist. Chem., 2008, 33, 61–67.

[30] - C. Gervais, et al., *Why does Prussian blue fade? Understanding the role(s) of the substrate*, J. Anal. At. Spectrom., 2013, 28, 1600. https://doi.org/10.1039/C3JA50025J

[32] – K. Hurlbutt, S. Wheeler, I. Capone, M. Pasta: *Prussian blue analogs as battery materials*. Joule 2018, 2, 1950–1960. https://doi.org/10.1016/j.joule.2018.07.017

[33] – K. Itaya, I. Uchida, V. D. Neff: *Electrochemistry of polynuclear transition metal cyanides: prussian blue and its analogues.* Accounts Chem Res 1986, 19, 162–168

[34] - G. Zampardi, M. Warnecke*, Effect of the reactants concentration on the synthesis and cycle life of copper hexacyanoferrate for aqueous Zn-ion batteries*, Electrochemistry Communications 126 (2021) 107030. https://doi.org/10.1016/j.elecom.2021.107030

[35] – G. Kasiri, *Synthesis and Characterization of Copper Hex-acyanoferrate and its Analogues as Cathode Material for Aqueous Zinc-Ion Batteries*.

[36] – C. D. Wessells, R. A. Huggins, Y. Cui. *Copper hexacy-anoferrate battery electrodes with long cycle life and high power.* Nature Communications 2011, 2, 1, 550. https://doi.org/10.1038/ncomms1563.

[37] - A. J. Bard, L. R. Faulkner, *Electrochemical Methods: Fundamentals and Applications*, Wiley, (2000).

[38]-C.G. Zoski, *Handbook of Electrochemistry*, Elsevier (2007)

[39] -A. Arya, A. L. Sharma, *Polymer electrolytes for lithium-ion batteries: a critical study*, Ionics 23 (2017) 497–540. 10.1007/s11581-016-1908-6

[40] - R.M. Winghtman, D.O. Wipf, A. Bard (Ed.), *Electroanalytical Chemistry*, M. Dekker

[41] - J. O. Bockris, A. K. N. Reddy, Modern Electrochemistry, vol. 1, Plenum, New York. 1970.

[42] - A. J. Bard, M. V. Mirkin, *Scanning Electrochemical Microscopy*, M. Dekker, New York, 2001

[43] - D. Shoup, A. Szabo, *Influence of insulation geometry on the current at microdisk electrodes,* J. Electroanal. Chem. 160 (1984) 27-31. https://doi.org/10.1016/S0022-0728(84)80112-6

[44] - K. Aoki, K. Akimoto, K. Tokuda, H. Matsuda, J. Osteryoung*: Linear sweep voltammetry at very small stationary disk electrodes*, J. Electroanal Chem. 171 (1984) 219. https://doi.org/10.1016/0022-0728(84)80115-1

[45] - M.I. Montenegro, M.A. Queiros, J.L. Dashbach, *Microelectrodes Theory and Applications* (NATO ASI series) Kluver (1992).

[46] - S.Nugues, G.Denuault, *Scanning electrochemical microscopy: Amperometric probing of diffusional ion fluexes through porous membranes and human dentine* J.Electroanal.Chem., 408 (1996) 125. https://doi.org/10.1016/0022-0728(96)04523-8

[47] - P.R.Unwin, J.Bard, *Ultramicroelectrode Voltammetry in a Drop of Solution: A New Approach to the Measurement of Adsorption Isotherms at the Solid-Liquid Interface,* Anal.Chem., 64 (1992) 113

[48] - A.L.Barker, M.Gonzalves, J.V.Macpherson, C.J.Slevin, P.R.Unwin, *Anal.Chim. Acta*, 385 (1999) 223

[49] - M.Tsionsky, Z.G.Cardon, A.J.Bard, R.B.Jackson, *Photosynthetic Electron Transport in Single Guard Cells as Measured by Scanning Electrochemical Microscopy,* PlantPhysiol. 113 (1997) 895. 10.1104/pp.113.3.895

[50] - I. Ciani, S. Daniele, *Voltammetric Determination of the Geometrical Parameters of Inlaid Microdisks with Shields of Thickness Comparable to the Electrode Radius*, Anal. Chem., 76 (2004) 6575. https://doi.org/10.1021/ac049041u

[51] - Y.Fang, J.Leddy, *Cyclic Voltammetric Responses for Inlaid Microdisks with Shields of Thickness Comparable to the Electrode Radius: A Simulation of Reversible Electrode Kinetics,* Anal.chem. 67 (1995) 1259-1270.

[52] - K. Aoki, J. Osteryoung, Diffusion-controlled current at the stationary finite disk electrode, J.Electroanal.Chem., 122 (1981) 19. https://doi.org/10.1016/S0022-0728(81)80137-4

[53] - S. Liu, G. L. Pan, G. R. Li, X. P. Gao, J. Mater. *Copper hexacyanoferrate nanoparticles as cathode material for aqueous Al-ion batteries*, Chem. A 3 (2015) 959-962. https://doi.org/10.1039/C4TA04644G

[54] - J.Bard, F.F.Fan, M.V.Mirkin, *Scanning Electrochemical Microscopy in Electro-analytical Chemistry*, A.J.Bard Ed., M.Dekker, New York, vol. 18, p.243

[55]- R. Trócoli, F. La Mantia. *An aqueous zinc-ion battery based on copper hexacyanoferrate*. ChemSusChem (2015) 8, 3, 481–485. https://doi.org/10.1002/cssc.201403143.

[56] -J. Newman, K. E. Thomas-Alyea. 2012. *Electrochemical Systems* (3., Edition). John Wiley & Sons, New York, NY.

[57] – D. R. Lide. 2004. *CRC handbook of chemistry and physics*. *A ready refererence book of chemical and physical data* (Eighty-fifth edition). CRC, Boca Raton, Fla., London.

[58] - R. Guduru, J. Icaza, *A brief review on multivalent intercalation batteries with aqueous electrolytes,* Nanomaterials 6 (2016) 41, https://doi.org/10.3390/nano6030041

[59] - C.D. Wessells, R.A. Huggins, Y. Cui, *Copper hexacyanoferrate battery electrodes with long cycle life and high power*, Nat. Commun. 2 (2011) 550, https://doi.org/10.1038/ncomms1563.

[60] - V. Renman, D. O. Ojwangb, M. Valvo. C. P. Gómez, T. Gustafsson, G. Svensson, *Structural-electrochemical relations in the aqueous copper hexacyanoferrate-zinc system examined by synchrotron X-ray diffraction,* Journal of Power Sources 369 (2017) 146-153. https://doi.org/10.1016/j.jpowsour.2017.09.079

[61] - A. Lovric M, F. Scholz, *A model for the propagation of a redox reaction through microcrystals*, J. Solid. State Electrochem. 1 (1997) 108-113